Alma Mater Studiorum · Università di Bologna

Scuola di Scienze
Corso di Laurea Magistrale in Fisica

Measurement of K(892)^{*0} resonance production in p-Pb collisions with the ALICE experiment at the LHC

Relatore:
Prof. Luisa Cifarelli

Correlatore:
Dott. Silvia Arcelli

Presentata da:
Lucia Leardini

Sessione II
Anno Accademico 2012/2013

Abstract

È qui presentato lo studio della produzione della risonanza K^{*0} in collisioni p-Pb con l'esperimento ALICE presso LHC. L'elaborato si compone di una introduzione sulla natura del fenomeno studiato: la formazione del Quark Gluon Plasma (QGP), uno stato della materia fortemente interagente ad alte temperatura e densità d'energia. Vengono descritte le segnature studiate ai fini di identificare il suddetto fenomeno, riportando come esempio concreto i risultati sperimentali. Successivamente l'acceleratore di particelle, LHC, e l'esperimento, ALICE, vengono brevemente introdotti. Più in dettaglio vengono descritti i rivelatori di ALICE effettivamente usati per l'analisi, a cui sono dedicate sezioni approfondite. Viene infine introdotta l'analisi e le sue motivazioni. Il metodo utilizzato e lo studio degli errori da associare alla misura sono illustrati in ogni loro passo e supportati dai risultati ottenuti. La discussione finale dei risultati include il confronto con i risultati precedentemente ottenuti da ALICE in collisioni pp e Pb-Pb e da altri esperimenti.

Contents

Introduction

The knowledge of how the universe came to be is one of the main research subjects of all times.
Stars and galaxies formation are largely studied today but what happened in those first moments after the enormous explosion called Big Bang is still obscure. ALICE (*A Large Ion Collider Experiment*), one of the biggest of the LHC (*Large Hadron Collider*) experiments, was built exactly for this purpose: to recreate, through heavy-ion collisions, the initial conditions after the Big Bang and the state of the matter at that time, made of unbound gluons, quarks and antiquarks, and called *Quark Gluon Plasma* (QGP). The interest in this field of research is not limited to astrophysics and cosmology but involves also physics as a mean to the deepening of our knowledge of QCD. Ultra-relativistic heavy-ion collisions are the probes used to explore this: they can recreate the primordial thermalized matter by colliding nuclei with high atomic number (Z) at high energies.
The complex system of detectors and electronics that constitute ALICE gather as much information as possible on the particles produced during the evolution of this strongly interacting medium as the temperature lowers and the energy density decreases while time is passing from the first ion collisions and gluons and quarks are bound together.
The first studies on QGP took place at CERN in the 80s and 90s, using the *Super Proton Syncrotron* (SPS). The research has been brought on by the *Relativistic Heavy Ion Collider* (RHIC) of the Brookhaven National Laboratories. There, gold and copper ions are used as projectiles at collision energies of the order of tenth and hundreds of GeV. LHC is now bringing the collision energy higher and higher, unveiling something more as it goes

on. Moreover, proton-proton and proton-lead collision are also part of the ALICE research program, in order to establish a reference for the study of heavy-ion collisions and disentangle initial state phenomenology. In fact, with proton-proton and proton-lead collision the QGP does not form, due to the insufficient energy density and the nature of the projectiles. As a consequence, it is possible to study how the system behaves with or without QGP formation and the differences or similarities between this two possible scenarios. Moreover, proton-lead collisions are an unique opportunity to study the behavior of nuclear forces without ambiguities: the asymmetry of the collision make it possible to discriminate initial from final-state medium effects.

Although the research on the primordial condition of the matter and its evolution after the Big Bang holds a great part of the ALICE Collaboration physics programme, this is not the only field that is being investigated. The purpose of the Collaboration has its base on a far greater field of interest: the expansion of our knowledge of the Quantum Chromo Dynamics (QCD) to farther limits and deeper understanding.

This thesis presents the analysis carried out on the data gathered from proton-lead collisions at the collision energy of $\sqrt{s_{\mathrm{NN}}} = 5.02$ TeV and focuses in particular on the production of the K^{*0} resonance. This study complements the results already obtained from proton and lead collision and is aimed to help their interpretation.

The first chapter will give an introduction of the QCD interactions that make Quark Gluon Plasma formation possible and an overview of the quantities involved with the phase transition from deconfined to confined matter (*hadronization*). A description of the typical signatures of QGP will be given. ALICE and the detectors that constitute it will be described in the second chapter. The *Time Projection Chamber* (TPC) and *Time-Of-Flight* (TOF) detectors will be treated in more detail since they are heavily used for the Particle Identification (PID) in the analysis presented here. The instruments used for the analysis, such as the AliRoot framework and the GRID system, will be described and the analysis method and development will be explained. The third and fourth chapter are dedicated to the analysis. In chapter three,

the analysis procedures will be illustrated and a detailed explanation of their steps will be given. In chapter four, the different systematic uncertainties that affect the measurements are introduced and the method followed for estimating the corresponding error on the K^{*0} yield will be described.
The fifth and final chapter will treat of the results obtained and of their physics interpretation.

Chapter 1

Physics of *Quark Gluon Plasma*

Quark Gluon Plasma is a strongly interacting state of the matter that forms after a heavy-ion collision. The temperature and energy density of this medium are extremely high and elementary particle such as quark, antiquark and gluons are not bound in hadrons but move freely in it. The physics of the strong interactions taking place during the evolution of the QGP are under study in this work. Every stage of the system evolution is analyzed: from heavy-ions collisions, passing through the expansion phases to the final hadronization and cooling of the matter.
In this chapter, an overview of some theoretical concepts that will be used later [1, 2, 4, 5, 6] will be given. An introduction to the physics of the Quark Gluon Plasma and to the physical signature that are used for the experimental study of this phenomenon [4] will follow.

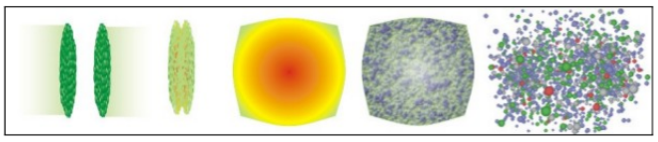

Figure 1.1: Pictographic representation of a ultra-relativistic heavy-ion collision. Left to right: the two nuclei approach, collide, form a QGP, the QGP expands and hadronizes, finally hadrons rescatter and freeze out.

1.0.1 QCD overview

Quantum Chromo Dynamics (QCD) was firstly introduced to justify the existence of the Δ^{++} baryon, discovered in 1951. At that time (ignoring what we know today about the colour charge) the Δ^{++} baryon appeared to be a fermion with symmetric flavour and spin wave function, $|\Delta^{++}\rangle = |u_\uparrow u_\uparrow u_\uparrow\rangle$, that should make it impossible for this particle to exist since a fermion must have a overall asymmetric wave function. The solution to this puzzle came years later with the introduction of the colour charge, a quantum number associated with SU(3) group, the gauge group on which the QCD is based. The Δ^{++} wave function can be made antisymmetric with this new degree of freedom

$$|\Delta^{++}\rangle = |\epsilon^{ijk} \quad u_{i\uparrow} u_{j\uparrow} u_{k\uparrow}\rangle \quad . \tag{1.1}$$

This was only the initial step to the formulation of the theory of strong forces that rules quarks and gluons interaction.

Quantum Chromodynamics is based on the SU(3) group, the special unitary group in 3 complex dimensions. The two fundamental representation are $\mathbf{3}$ and $\bar{\mathbf{3}}$. Colour charges (*red*, *green*, *blue*), QCD analogous of the positive electric charge, belong to the first one while anti-colour charges, (anti-*red*, anti-*green*, anti-*blue*), analogous of the negative electric charge, belong to the latter. SU(3) is an exact symmetry, meaning the colour charges are absolutely conserved. The strong force vector boson, the gluon, is part of an octet[1]: the gluon carries colour charge and can participate to interaction vertexes with two or three other gluons. The QCD is a non-abelian theory. The interactions of quarks and gluons with each other or with other particles can be pictured using Feynman diagrams like in the QED case, substituting the electromagnetic coupling constant with the strong coupling constant, $\alpha_s(Q^2)$. It must be noted that the coupling constant is dependent on the energy (Q^2) at which the interaction takes place; this affects the computation of the interaction cross section too, since Feynman diagrams are also used to

[1] From the two fundamental representation: $\mathbf{3} \bigotimes \bar{\mathbf{3}} = \mathbf{8} \bigoplus \mathbf{1}$, that gives a coloured octet and a "colourless" singlet combination that does not interact with quarks.

estimate the cross section. The strong interaction coupling constant is

$$\alpha_s(Q^2) = \frac{1}{\frac{33-2N_f}{12\pi}\ln(Q^2/\Lambda_{QCD})}, \tag{1.2}$$

where N_f is the number of flavours considered, Q^2 the quadratic transferred quadrimomentum and Λ_{QCD} ~200 MeV specifies the energy scale at which $\alpha_s(\Lambda_{QCD}) \sim 1$ and the perturbative coupling would nominally become infinite (called the Landau pole). Eq. 1.2 is valid only in the purely perturbative regime and it is not reliable at strong coupling. This equation should not be taken to imply that the physical behavior of full QCD should exhibit a divergence for $Q \to \Lambda$.

As shown in Fig.1.2 the QED and QCD coupling constants have differ-

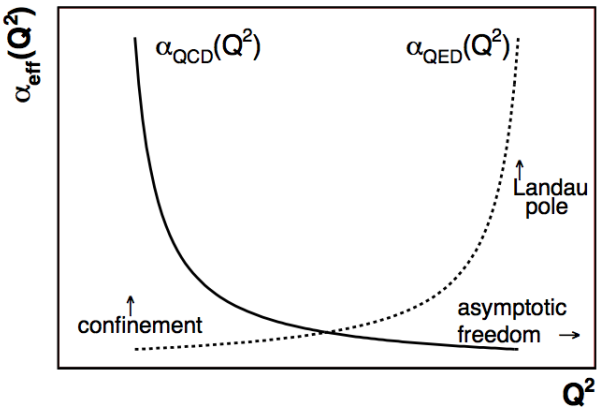

Figure 1.2: Running of the QED and QCD coupling constant [3].

ent behaviours due to the different nature of the forces that they represent and both depend on the energy scale considered, that is, they are "running" coupling constant. At high energies the value of α_s decreases entering the *asymptotic freedom* region. As a consequence, due to the effectively decreasing coupling, a perturbative approach to the theory can be used to predict its behaviour at even higher energies.

At lower energies, the coupling rapidly increases at scales below 1 GeV. This divergency is called *confinement* or *infrared slavery*. Here, the perturbative

method fails to describe the physical behavior of the strongly interacting particles and a numerical approach is used as substitute for prediction: the *Lattice*-QCD.
Even though with some limitations – multi-scale and/or time-evolution problems – *Lattice*-QCD (ℓQCD) has been an indispensable tool to study phenomena such as the Chiral Condensate and the QCD phase transition. To verify its validity, ℓQCD was used to study the strong coupling in comparison with the perturbative method calculations, proving itself an adequate approach to non-perturbative QCD.
In this work, *Lattice*-QCD in relation to the phase transition will only be briefly described in some of the theoretical aspects (see 1.0.2).

1.0.2 Lattice QCD observables

Lattice-QCD (ℓQCD) is a method for calculating equilibrium properties of strongly interacting systems directly from the QCD Lagrangian by numerical evaluation of the corresponding path integrals [4].
The Lagrangian defining Quantum Chromodynamics is

$$\mathcal{L} = -\frac{1}{4}F^{a}_{\ \mu\nu}F^{\mu\nu}_{a} - \sum_{f}\bar{\psi}^{f}_{\ \alpha}(i\gamma^{\mu}\partial_{\mu} + m_{f} - g\gamma^{\mu}A_{\mu})^{\alpha\beta}\psi^{f}_{\ \beta}, \tag{1.3}$$

where $\psi^{f}_{\ \alpha}$ are the quark field of colour α (α = 1,2,3) and flavour f, γ^{μ} are Dirac matrixes, g is the coupling constant. A_{μ} is the vector potential of the strong interaction, while the gauge invariant gluon field strength tensor is given by

$$F^{a}_{\ \mu\nu} = (\partial_{\mu}A^{a}_{\ \nu} - \partial_{\nu}A^{a}_{\ \mu} - gf^{a}_{\ bc}A^{b}_{\ \mu}A^{c}_{\ \nu}), \tag{1.4}$$

where $A^{a}_{\ \mu}$ denotes the gluon field of colour a (a = 1,2,...,8) and $f^{a}_{\ bc}$ are the SU(3) structure constants. The bare quark masses are indicated as m_{f}. The thermodynamic is obtained from the partition function $Z(T,V)$, which is expressed as a functional path integral and involves directly the Lagrangian

density defining the theory,

$$Z(T,V) = \int dA\, d\psi\, d\bar{\psi}\, \exp\left(- \int_V d^3x \int_0^{1/T} d\tau \mathcal{L}(A,\psi,\bar{\psi}) \right), \qquad (1.5)$$

where $\mathcal{L}(A,\psi,\bar{\psi})$ is the Lagrangian defined in Eq.1.3 and the integrals in the exponent are over the volume V and over the inverse of the temperature T of the system. In the thermodynamic limit ($T \to \infty$, $V \to \infty$) the exponent becomes infinite. TAssuming a finite temperature[2] for the ℓQCD treatment, two observables are of particular interest: the scalar quark density $\bar{\psi}(x)\psi(x)$ of the system and the *Polyakov loop* operator defined as

$$L = \frac{1}{3} \mathrm{tr}(\mathcal{P}\, e^{ig\int_0^\beta A_4(\mathbf{x},\tau)d\tau}), \qquad (1.6)$$

where $A_4 = A_4^a \frac{\lambda_a}{2}$ is a 3×3 matrix and $\mathcal{P}$ stands for path ordering.

Due to translational invariance of the QGP medium both have x-independent thermal expectation values which, however, show a strong temperature dependence, as it can be seen in Fig.1.3.

A vanishing thermal expectation value $\langle L \rangle$ of the Polyakov loop operator (left in Fig.1.3) indicates infinite energy for a free quark, that is quark confinement. This happens at small temperatures. As the temperature increases, $\langle L \rangle$ increases rapidly to a non-zero value at high temperatures, with a relatively sharp peak of its derivative at a critical coupling β_{cr}: the quark confinement is broken at the corresponding critical temperature T_{cr}.

The Polyakov loop can be then used as a discriminator between the confined and deconfined phase of the QCD matter.

This behaviour is reversed for the scalar quark density (right in Fig.1.3). At low temperatures, $\bar{\psi}(x)\psi(x)$ has a non-vanishing expectation value ("chiral condensate") which evaporates below a critical temperature. For massless quarks the QCD Lagrangian is chirally symmetric, meaning it is invariant

[2]Figure1.3 is obtained fixing the quark mass at a specific temperature-dependent value $m_q = 0.8T$ in the lattice calculation. This value here is unrealistically large for simplicity since calculations with realistic and temperature-independent masses are very costly computationally. Repeating the calculations for several unrealistically large masses and it is possible to extrapolate to zero mass.

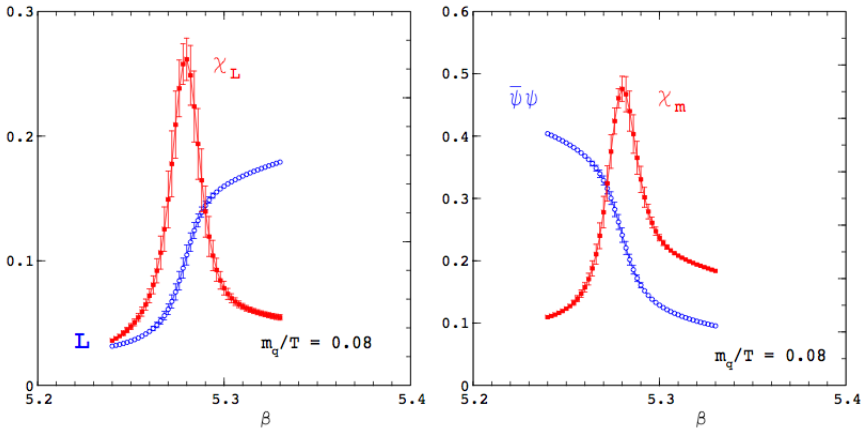

Figure 1.3: Left: Polyakov loop expectation value $\langle L \rangle$ and its temperature derivative (Polyakov loop susceptibility χ_L) as a function of the lattice coupling $\beta = 6/g^2$ which is monotonically related to the temperature T (larger β correspond to larger T). Right: The chiral condensate $\langle \bar{\psi}\psi \rangle$ and the negative of its temperature derivative (chiral susceptibility χ_m) as a function of temperature [4].

under separate SU(2) rotations of right- and left-handed quarks. Since the up and down quark masses in $\mathcal{L}_{QCD}$ are very small, neglecting them is a good approximation. The non-vanishing chiral condensate at $T = 0$ breaks this chiral symmetry and generates a dynamic mass of order 300 MeV for the quarks (the corresponding "constituent" masses in vacuum are ∼300 MeV for the up and down quarks and ∼450 MeV for the strange quark whose bare mass in $\mathcal{L}_{QCD}$ is ∼150 MeV). The dynamically generated mass tends to zero for $T \geq T_{cr}$: the approximate chiral symmetry of QCD is restored.
Deconfinement and chiral symmetry restoration are both important to understand the final products of heavy-ion collisions, and vice versa. Deconfinement frees a large number of gluons which can produce additional quark-antiquark pairs and introduce flavour not present before the collision (strange, charm and beauty quarks). The vanishing dynamical quark masses above T_{cr} make the quarks lighter and lowers the quark-antiquark pair production threshold. This is particularly important for the production of resonances and bound states whose constituent quark mass is much higher than the critical temperature.

1.0.3 QCD phase diagram

Figure 1.4 shows the phase diagram of the strongly interacting matter as a function of the temperature, on the y-axis, and of the baryochemical potential[3], on the x-axis. At T = 0 and $\mu_B \simeq m_N \simeq$1 GeV sits the ordinary nuclear

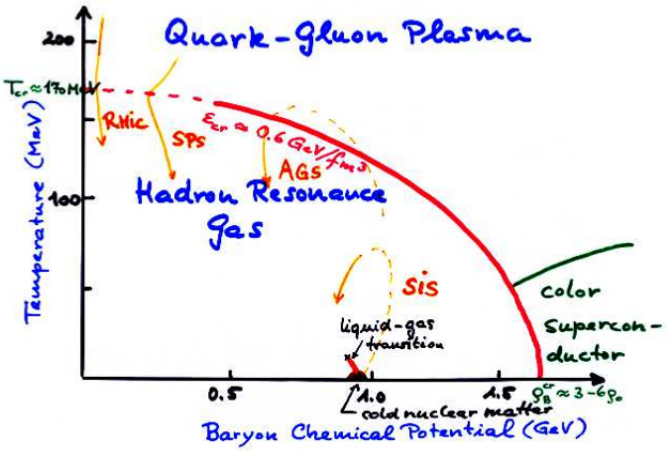

Figure 1.4: QCD phase diagram.

matter, called cold nuclear matter. ℓQCD calculations predict that the temperature at which the deconfinement transition from a hadron resonance gas to a Quark Gluon Plasma takes place is at $T_{cr} \approx$170 MeV for $\mu_B = 0$. It is not a sharp phase transition but a rapid crossover. For $T > T_{cr}$, due to the dissociation of the massive hadrons in massless or quite massless quarks and gluons, the energy density of the system increases rapidly. Phenomenological models (examples are given in [7]) have suggested the discriminating value between QGP and hadron gas to be at roughly constant critical energy density $\epsilon_{cr} = 1$ GeV/fm^3. At low temperatures and asymptotically large baryon densities quarks are also deconfined, not in a quark-gluon plasma state but

[3]The chemical potential μ, and the baryochemical one (μ_B) in an analogous way, quantifies the change of the internal energy U of a system due to the addition of a particle (or a baryon): $\mu = \frac{\partial U}{\partial N}$. μ_B can also be obtained as the ratio between baryons and antibaryons aboundances.

in a colour superconductor. The superconducting state is separated from the QGP by a first order transition at a critical temperature estimated to be of order 30-50 MeV.

1.1 Heavy-ion collisions and Quark Gluon Plasma signatures

Ultra-relativistic heavy-ion collisions allow to study hadronic matter under extreme conditions including the phase transition to QGP and its subsequent evolution from hot dense strongly interacting matter (or *fireball*) to its fragmentation in hadrons.
In nucleus-nucleus collisions not all of the particles created in the primary collisions between the incoming nucleons can immediately escape into the surrounding vacuum. Instead, they scatter off each other in a limited area, creating the dense and strongly interacting matter which, when it thermalizes quickly enough and at sufficiently large energy density, is a Quark Gluon Plasma. This does not happen in elementary particle (proton) collisions: the particles resulting from the collision escape right away from the interaction area in the form of a hadron gas.
The medium produced after the heavy-ion collision undergoes three main stages: termalization, expansion and decoupling, as schematically draw in Fig.1.5.

In the early stages of the collision, before QGP formation, heavy quarks and jets are formed. These are called *hard* probes: they are particles with large mass and high traverse momentum ($p_T \gg 1$ GeV/c). In central collisions between nuclei, the reaction zone has a diameter of about 12 fm so that the hard probe which is created near the border of the reaction zone moves inwards through it, taking 12 fm/c before exiting on the opposite side. In this time interval, the *soft* matter, the bulk of the particle produced during the collision, termalizes, expands and cools. The hard particle probes all this phases while traveling: it scatters in the forming medium and loses energy. This energy is proportional to the medium density, the particle cross section

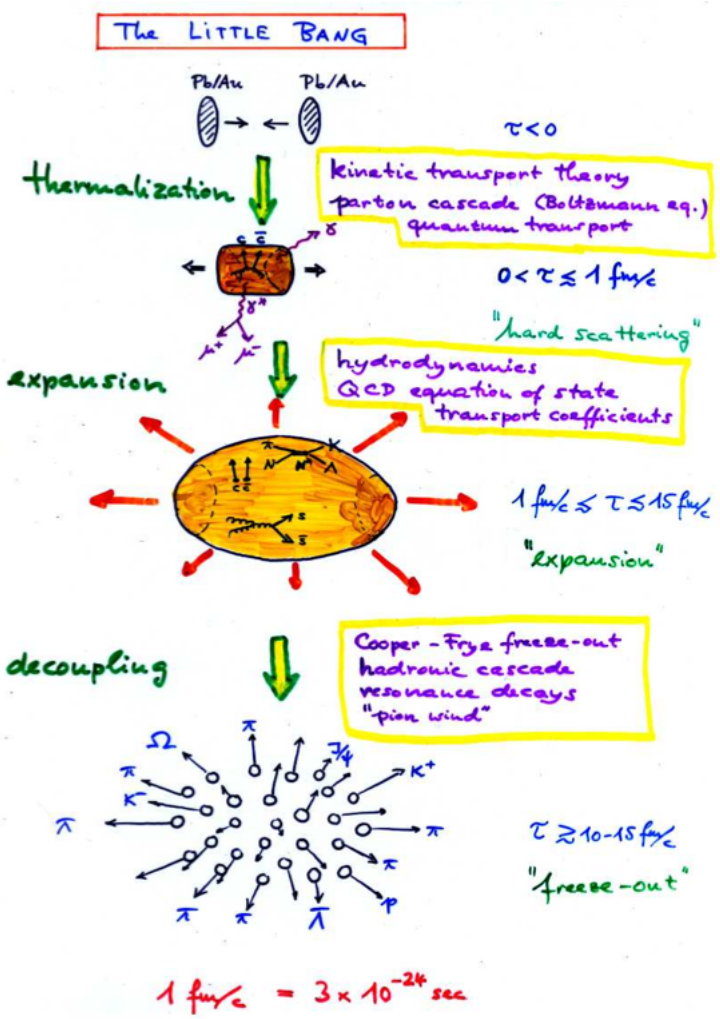

Figure 1.5: Stages of an heavy-ion collision [4].

and the path length and can be measured [8].

At this stage, direct photons are also a probe. They form in a medium constituted by a large amount of charged quarks and antiquarks from the early stages of the collisions. Direct photons can be real or virtual, in which case they are detected as final-state dileptons (e^+e^- o $\mu^+\mu^-$). Since their cross section is small ($\sigma \propto \alpha_{EM}^2$), direct photons can travel through the medium undisturbed, carrying uncontaminated information on the particles that originated them. On the other hand, the enormous electromagnetic background

makes direct photons and dileptons difficult to reconstruct.
The produced partons re-scatter both elastically and inelastically. Both types of collisions lead to equipartitioning of the deposited energy, but only the inelastic collisions change the relative abundances of gluons, light and strange quarks. From the phenomenology of pp collisions it is known that the produced hadron abundances are distributed statistically, but that strange hadrons are systematically suppressed, because strange quarks are not present in the initial state and their large constituent mass of ≈450 MeV makes them hard to be created from the vacuum [9, 10]. In a heavy-ion collision, if the reaction zone thermalizes at energy density $> \epsilon_{cr}$ such that gluons are deconfined and chiral symmetry is restored, strange quarks are much lighter ($m_s <$ 150 MeV) and can be relatively easily created by secondary collisions among the many gluons. The observed strangeness suppression in pp collisions is expected thus to be reduced or absent in relativistic heavy-ion collisions.
This has been historically referred to as the "strangeness enhancement" [11] and considered a distinctive signature of the QGP. After low energy heavy-ion experiments, ALICE has also observed an enhancement in the strange hadrons component. An example of the the results obtained by SPS, RHIC and ALICE on strangeness enhancement is shown in Fig. 1.6.

As a consequence of the thermal pressure of the thermalized system acting against the surrounding vacuum, a collective (hydrodynamic) expansion of the collision fireball takes place. The fireball cools and its energy density decreases. When $\epsilon_{cr} = 1$ GeV/fm^3, the partons convert to hadrons. In this phase transition the entropy density drops steeply over a small temperature interval but, since the total entropy can not decrease, this implies that the volume of the fireball must increase by a large factor while the temperature remains approximately constant. The growth of the fireball volume takes time, so the fireball ends up spending significant time near T_{cr}.
While inelastic processes can change the chemical abundances of the hadrons, elastic collisions change their momentum distribution. Since the corresponding inelastic cross sections are only a small fraction of the total cross section, inelastic processes stop long before the elastic ones. When the mean distance between hadrons is bigger than the range of the strong interactions, inelastic

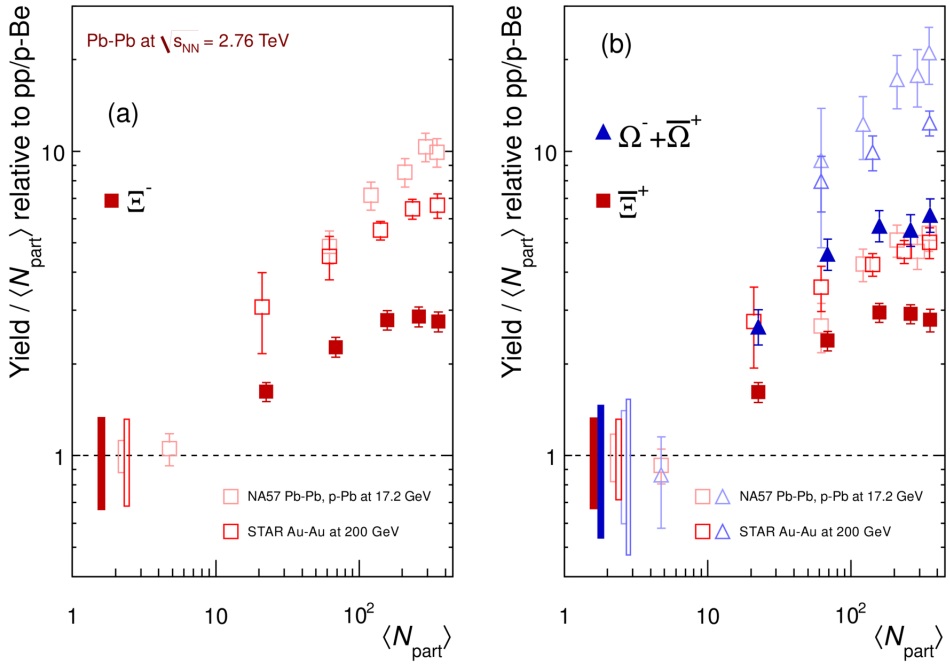

Figure 1.6: Strange hadrons enhancements in the rapidity range $|y| < 0.5$ as a function of the mean number of participants $\langle N_{part} \rangle$, measured at LHC (ALICE, full symbols), RHIC and SPS (open symbols). The LHC data use interpolated pp values. Boxes on the dashed line at unity indicate statistical and systematic uncertainties on the pp or p-Be reference. Error bars on the data points represent the corresponding uncertainties for all the heavy-ion measurements and those for p-Pb at the SPS [13].

reactions stop and the chemical compositions are fixed. This stage is called *chemical freeze-out*. The hadrons keep scattering elastically for a while, continuing to build up pressure for the expansion flow, until the matter becomes so dilute that also elastic interactions stop and the hadrons decouple (*kinetic freeze-out*). At kinetic freeze-out all hadrons, including the then present unstable resonances, have an approximately exponential transverse momentum spectrum reflecting the temperature of the fireball at that point.

Depending on the collision phase at which they formed, Quark Gluon Plasma signatures are classified into *hard probes* or *soft probes*:

- hard probes: signal produced in the early stages of the collision, due

to high momentum parton interaction. In this category are grouped heavy quarks and their bound states (charmonium, bottomonium), *jet quenching*, direct photons, dileptons;

- soft probes: signal produced in the later stages of the collision, they carry indirect information on the phase transition and on QGP. These information are accessible through spectra studies, with strangeness enhancement, anysotropic flow, particle correlations, etc.

1.1.1 Hard probes

Direct photons and dileptons

Direct photons and dileptons are electromagnetic probes; since they interact electromagnetically ($\alpha_{EM} \ll 1$), they should not be affected by the strongly interacting medium. Direct protons have a mean-free path larger than the size of the fireball and this means they do not interact but leave the fireball region undisturbed. They carry information on the early thermal state of the medium in which they were created and they are further divided in prompt photons, fragmentation photons and thermal photons. Prompt photons are produced in hard scattering processes of gluons and quarks: $q + g \rightarrow q + \gamma$ (quark-gluon Compton), $q+\bar{q} \rightarrow g+\gamma$ and bremsstrahlung. Quark-antiquark annihilation in two direct photons is only possible if the latter are virtual; the virtual photons will then decay into lepton pairs, which are another QGP electromagnetic signature. Prompt photons have high transverse momentum that allows for a perturbative treatment of the problem, can give us constraints for non-perturbative quantities such as parton density functions (PDFs) and can be a reference not only for other hard probes (e.g. jets) but also for a comparison between the different systems (pp, A-A, p-A) used to study nuclear forces. Fragmentation photons are produced in the fragmentation of hard scattered quarks or gluons ($q + q \rightarrow q + q + \gamma$). Thermal photons come from thermal production and have low/medium transverse momentum. The photon emission spectrum (momentum distribution) can provide information about the temperature of the system or about its chem-

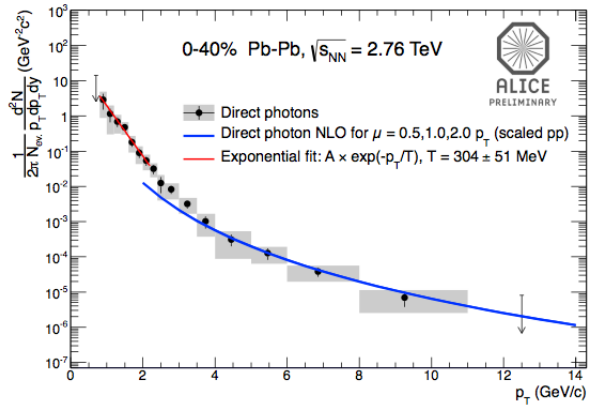

Figure 1.7: Direct photon invariant yield in 0-40% Pb-Pb collisions at $\sqrt{s_{\rm NN}}$ = 2.76 TeV with NLO pQCD prediction and exponential fit [16].

ical composition. Fig. 1.7 shows the direct photon spectrum in the 0-40% most central Pb-Pb collisions at $\sqrt{s_{\rm NN}}$ = 2.76 TeV as measured by ALICE. For transverse momenta above 4 GeV/c, the signal is described by binary scaled NLO (pQCD) calculations for pp [15]. At low p_T the spectrum shows an excess above the pQCD prediction which can be described by an exponential function. Assuming a thermal origin of low p_T direct photons, the inverse of the temperature T in the exponential slope parameter can be interpreted as an effective temperature of the source integrated over the whole system evolution. A high value of this temperature ($\sim$ 300 MeV) compared to the critical temperature for deconfinement (150-170 MeV [17, 18]) implies an early production time of direct photons during the system evolution [16]. Dileptons production is also composed by a thermal component, an hard scattering component and a "background" component due to mesons decay. In respect to direct photons, dileptons carry an additional information: the invariant mass of the pair, strictly related to the dynamics of excitation of the matter.

Quarkonia

Heavy flavours are, among the hard probes, a very important signature for QGP. Heavy quarks (charm and beauty) are produced during the early stages ($t \simeq 1/2m_q$) [19] of the collisions and, conversely to light quarks, which can be thermally produced, heavy quarks maintain their identity through the hot stage of the collision and they experience the whole evolution of the system. Their production takes place in time intervals of the order of $1/m_q$ but their life-time is long, so that heavy quarks can live through the termalization and hadronization phase. Of particular interest is the study of the in-medium energy loss due to elastic processes (collisional energy loss) and inelastic processes that can provide important insight on the properties of the medium.
Quark and antiquark pairs can form bound states called quarkonia (charmonium and bottomium) whose binding energy is proportional to the mean energy of the medium. The suppression of quarkonium states in heavy-ion collisions is accepted as a signature of a formation of a Quark Gluon Plasma. The phenomenon mainly involved in the suppression is the color screening mechanism [20]. The screening radius is estimated from *Lattice*-QCD results to be around 0.3-0.5 fm [6]. When the medium in which the heavy quarks form has high density, the range of the potential between two charges (c and $\bar{c}$ or b and $\bar{b}$) in this medium is reduced to what is called the screening radius. If the quarkonia state of the two quark has radius larger than the screening radius, the bound state does not form. The presence of an higher number of quarks of other flavours (u, d and s) favours the production of open flavour (e.g. the D mesons).
Other phenomena that participate in the quarkonia suppression are the dissociation in cold nuclear matter [21] and/or in the hot confined medium [22]. Also initial state effects, such as nuclear shadowing and initial state parton energy loss are expected to play a role [23].
A suppression compared to pp collisions was observed in p-A collisions [24], which was understood as a destruction of the pre-resonant $c\bar{c}$ state by the nucleons of the colliding nuclei. The measurements in Pb-Pb at the SPS ($\sqrt{s_{\mathrm{NN}}}$ = 17.3 GeV) [25] and in Au-Au at RHIC [26] showed an anomalous

suppression, attributed to the presence of hot and dense QCD matter. The phenomenon is theoretically interpreted as a sequential suppression [27, 28] of various charmonium states as a function of energy density or temperature of the QGP. A clear difference to the RHIC results was seen in the first LHC measurement of the overall (inclusive in p_T) production, performed in ALICE [29].

In Fig.1.8 an example of suppression for the J/ψ is reported. The suppression is represented by the nuclear modification factor R_{AA}, defined as the ratio of the yield in Pb-Pb collisions to the pp yield scaled by the number of binary collisions

$$R_{AA} = \frac{d^2N/dp_T d\eta}{\langle T_{AA}\rangle d^2\sigma_{pp}^{inel}/dp_T d\eta}, \tag{1.7}$$

where T_{AA} is the nuclear overlap function computed from the Glauber model [30] and σ_{pp}^{inel} the pp inelastic cross section.

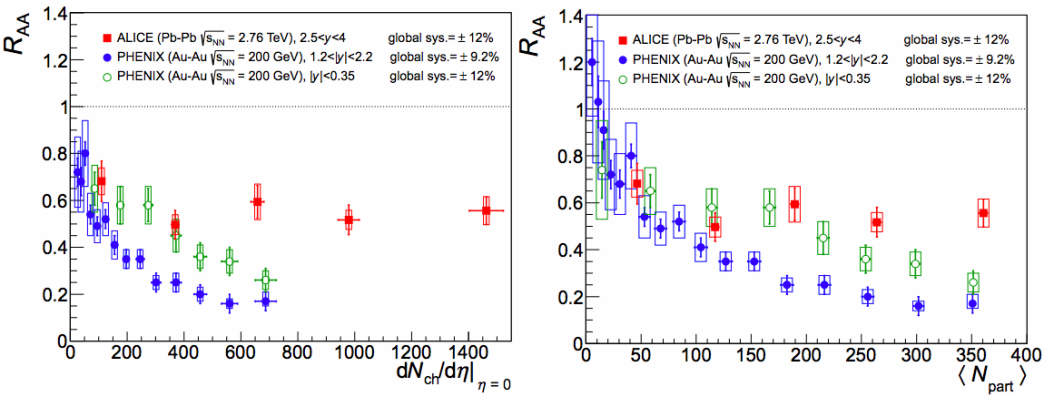

Figure 1.8: (Color online) Inclusive J/Ψ R_{AA} as a function of the mid-rapidity charged-particle density (left) and the number of participating nucleons (right) measured in Pb-Pb collisions at $\sqrt{s_{\rm NN}} = 2.76$ TeV, measured by ALICE, compared to PHENIX results in Au-Au collisions at $\sqrt{s_{\rm NN}} = 200$ GeV at mid-rapidity and forward rapidity. [29] and reference therein.

Jet quenching

Another interesting phenomenon observed in heavy-ion collisions is the quenching of partons and jets at high transverse momentum. When a high-p_T parton or a jet (defined as a set of particles emitted in a small region in the momentum space, generated from the fragmentation of an hard parton) travels through a medium of dense and hot matter, such as the QGP, it loses energy in radiative processes and in elastic collisions with the surrounding partons. The result is the production of a smaller number of particles with high transverse momentum. Looking at their azimuthal distribution of a dijet (a pair

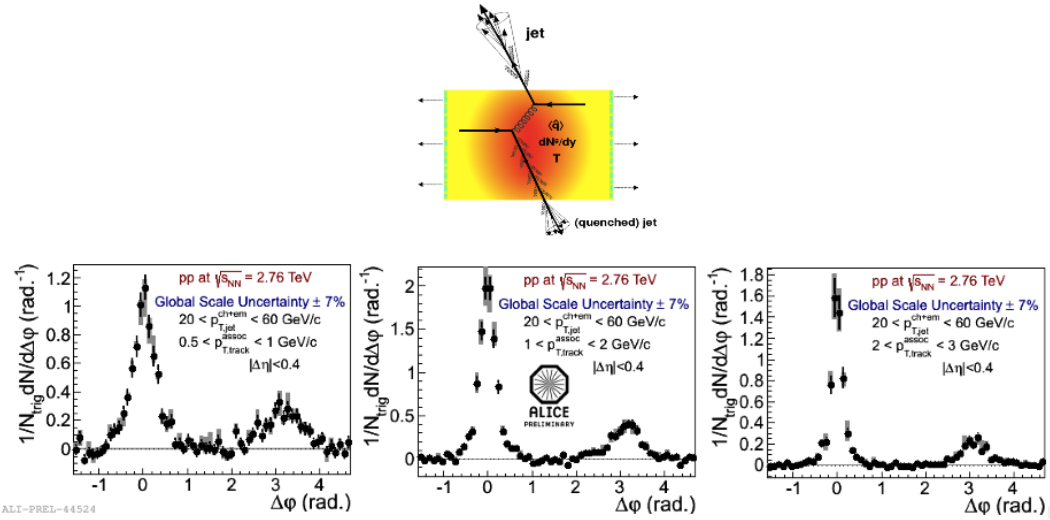

Figure 1.9: Left: Jet quenching in a head-on nucleus-nucleus collision. Two quarks suffer a hard scattering: one goes out directly to the vacuum, radiates a few gluons and hadronizes, the other goes through the dense plasma created, suffers energy loss due to medium-induced gluonstrahlung and finally fragments outside into a (quenched) jet [31]. Right: $\Delta\phi$ distribution of 20-60 GeV/c jets reconstructed on particles with $p_T > 3$GeV/c correlated with 0.5-3GeV/c tracks in 3 associated momentum bins.

of jets produced back to back for energy-momentum conservation), Fig.1.9, it can be seen that one jet, produced near the fireball surface, has a yield greater than the yield of the jet moving inward through the fireball. This is due to the fact that the second jet has interacted in the medium, losing energy before leaving the fireball. The approximate position of production

of the jet can be reconstructed through jet correlation studies. The proportionality of the energy loss to the square of the path length of a particle can provide useful information on the kind of medium formed after the collision [8].

1.1.2 Soft probes

Strangeness enhancement

The definition of strangeness enhancement was given in section 1.1.
Both in heavy-ion collisions and in proton collisions the net strange content of the system before the collision is zero and extra strangeness cannot be produced by final state hadronic re-scattering; strangeness enhancement thus reflects the properties of the prehadronic state.
In the presence of QGP, the energy threshold for a strange quark production is lowered as a consequence of the partial restoration of the chiral symmetry [33]. $s\bar{s}$ pairs are more probable to be produced since there is a larger amount of gluons in the fireball (due to the nature of the projectile particles). Strangeness pair production is mainly due to gluon fusion processes ($gg \rightarrow s\bar{s}$). The overall effect is an enhancement in the strangeness of the system, i.e. in the number of strange hadrons. Moreover the greater the strangeness content in a hadron, the more pronounced is the enhancement effect, as it can be seen from the ALICE and lower energy experiments results reported in Fig. 1.10. On the other hand, in pp collision the strange quark production is strongly suppressed: a hadronic gas takes the place of QGP but since quark-gluon fusion is very unlikely to occur and the strange mass is too large (compared to the up and down quark masses) so that it is difficult for the system to overcome the production threshold. As a result, the total fraction of strange particles is about twice as high in heavy-ion collisions compared to elementary particle collisions. Strangeness production can also be enhanced in a pure hadronic scenario [6]. If, during the heavy-ion collision, the gas of produced hadrons has enough time to interact, the inelastic collisions will drive the system towards chemical equilibrium. In this

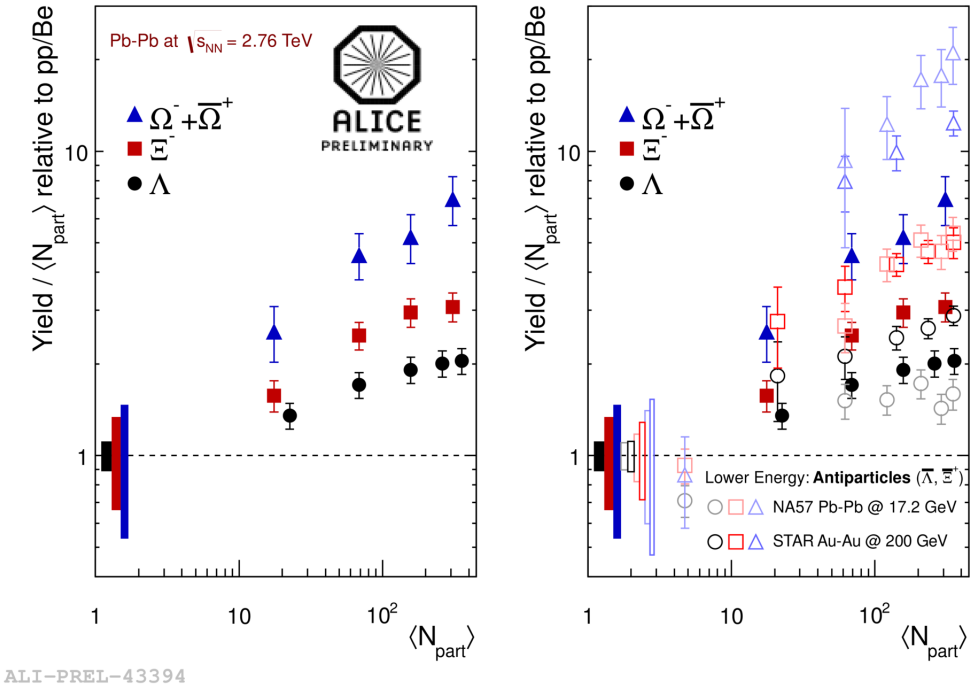

Figure 1.10: Strangeness enhancement for Λ, Ξ^- and Ω^- shown with $\langle N_{part} \rangle$ scaling and comparisons to lower energy measurements from NA57 and STAR [34].

scenario, at the early stages strangeness production is suppressed and during the hadronic re-interactions the strangeness content will increase with time. A typical inelastic process of this type is $\pi^0 + p \rightarrow K^+ + \Lambda$. Once we produce a strange particle, the probability to destroy it is very low, because it interacts mostly with pions and nucleons (until strangeness will reach its equilibrium value). For multi-strange hadrons such re-interactions will be much less effective because their production requires a longer reaction chain, that has low probability and therefore needs a long time. In addition, multi-strange particles can easily be destroyed in subsequent interactions with pions or nucleons. Therefore, the approach to chemical equilibrium for these hadrons will be very slow. The direct production of a pair is strongly suppressed because of the high threshold.

In any case, the exclusivity of the gluon fusion process and the low background on the particles of interest (strange hadrons) make of strangeness

enhancement an important signature of Quark Gluon Plasma formation.

Collective flow

The presence of collective flow is considered another signal of the formation of the Quark Gluon Plasma. A flow is the movement of correlated particles, dependent on the expansion of the system in which the particles are produced. If the system is a thermalized one (or approximately thermalized like the QGP), it has non-zero thermal pressure. The gradient with respect to the vacuum surrounding the system pushes it outwards, starting the collective flow. In this way, the presence of flow is an unambiguous signal of the presence of QGP: absence of collective flow would indicate absence of pressure and imply absence of a hot thermalized system.
The flow velocity $\mathbf{v}(x)$ can be separated into its components along the beam direction (longitudinal flow v_L) and in the plane perpendicular to the beam (transverse plane $v_\perp$), called transverse flow. The magnitude of $v_\perp$ may depend on the azimuthal angle around the beam direction, i.e. on the angle between $v_\perp$ and the impact parameter b of the collision. In this case we call the transverse flow anisotropic. Radial flow is its azimuthal average.

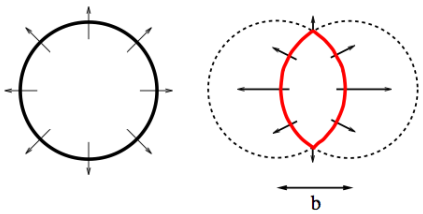

Figure 1.11: Schematic picture of radial and anisotropic (elliptic) flow [4].

Radial flow

If the impact parameter (b) is taken as a reference to define the interaction plane, a collision is central when $b = 0$ (for ALICE definition of centrality

see chapter 3). In heavy ion collisions this means that the nuclei collide head on, they are aligned and the only flow present is the radial one.

Anisotropic flow

If the collisions are non-central, the geometrical overlap region of two colliding nuclei is azimuthally anisotropic. As said above, the pressure gradient between the thermal system and the surrounding vacuum pushes the first one outwards. Since the gradient is larger in the direction where the size of the expanding medium is smaller, the geometrical anisotropies cause anisotropies in the particle emission: the initial spatial asymmetry is converted into an anisotropy in momentum space through re-scattering processes. This phenomenon is the onset of transverse anisotropic flow. Anisotropic flow [35] develops before the medium reaches the critical temperature and hadronizes, so that it is sensitive to the equation of state of the QGP phase.
The anisotropy is quantified in terms of the azimuthal Fourier coefficients of the transverse momentum spectrum [36, 37]:

$$E\frac{dN^3}{dp^3} = \frac{1}{2\pi}\frac{dN^2}{p_T dp_T dy}\left(1 + 2\sum_{N=1}^{\infty}\nu_n \cos[n(\phi - \Psi_n)]\right) \tag{1.8}$$

where n is the order of the harmonic, ϕ indicated the particle azimuthal angle and Ψ_n is the angle of the spatial plane which maximize the expectation value of ν_n in each event, the harmonic symmetry plane. The flow coefficient are dependent on the p_T and on the pseudorapidity η and are given by $\nu_n(p_T, \eta) = \langle\cos[n(\phi - \Psi_n)]\rangle$, where the average is over particles in a given p_T and over events in a given centrality class. The three coefficients of main interest at present are the elliptic flow ν_2, the triangular flow ν_3 and the quadrangular flow ν_4 (which is considered with respect to the second (ν_4/Ψ_2) and fourth (ν_4/Ψ_4) harmonic symmetry planes [37]. ν_2 is the representation of the initial symmetry while $\nu_{n>2}$ reflects the local fluctuations of the initial conditions.

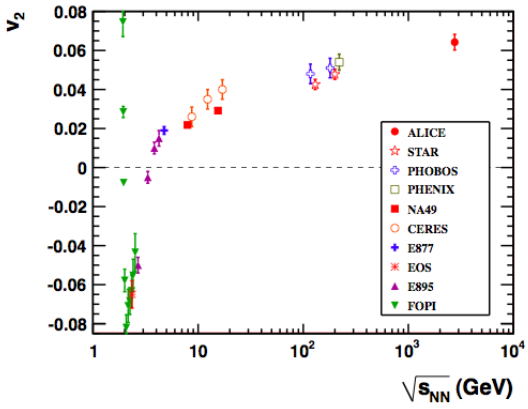

Figure 1.12: Azimuthal flow ν_2 of charged particles measured by the ALICE experiment in Pb-Pb collisions at $\sqrt{s_{\rm NN}} = 2.76$ TeV in comparison with the lower-energy experiment results [40].

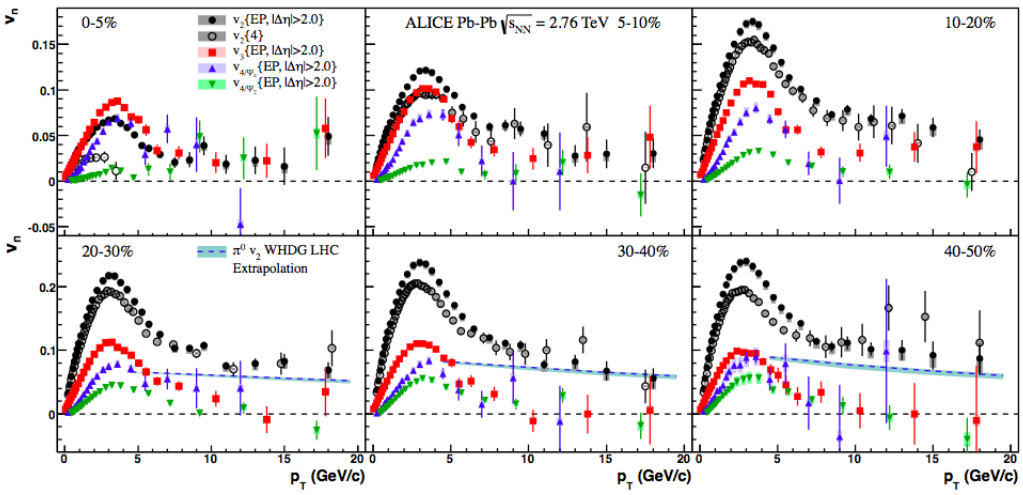

Figure 1.13: (color online) ν_2, ν_3 and ν_4 measured (by ALICE) for unidentified charged particles as a function of transverse momentum for various centrality classes. The dashed line represents the WHDG model calculations for neutral pions ν_2 [41] extrapolated to the LHC collision energy. For clarity, the markers for ν_3 and ν_2/Ψ_2 results are slightly shifted along the horizontal axis. Error bars (shaded boxes) represent the statistical (systematic) uncertainties.

Theoretical models, based on relativistic hydrodynamics [38, 39], successfully described the elliptic flow observed at RHIC and predict its increase at LHC energies from 10% to 30%. In Fig.1.12 elliptic flow integrated over p_T measured by the ALICE experiment and lower-energy experiments is shown. The observed trend of ν_2 versus $\sqrt{s_{\rm NN}}$ confirms model expectations that the value of ν_2 in Pb-Pb collisions at $\sqrt{s_{\rm NN}} = 2.76$ TeV increases by about 30% with respect to ν_2 in Au-Au collisions at $\sqrt{s_{\rm NN}} = 0.2$ TeV [40].
Significant triangular flow was also observed at the Relativistic Heavy Ion Collider and at the Large Hadron Collider, [37]. Fig.1.13 shows unidentified charged particle ν_2, ν_3, and ν_4 as a function of transverse momentum for different centrality classes measured by ALICE [41].

Spectra

The expansion of the hadrons emitted in heavy-ion collisions is characterized by the appearance of collective flow in the soft region of the spectrum, as described in 1.1.2. Radial flow is the component of the collective motion isotropic with respect to the reaction plane. It determines the expansion in the radial direction and can be estimated by measuring the primary hadron transverse momentum spectra, that also contains the information about the temperature of kinetic freeze-out (T_{kin}). The ALICE measurement of identified particle spectra in central (0-5%) Pb-Pb collisions at $\sqrt{s_{\rm NN}} = 2.76$ TeV is represented by the red symbols in Fig.1.14 [42]. The mid-rapidity ($|y| < 0.5$) p_T-integrated particle yields were extracted by fitting the π, K and p spectra individually with a blast wave function, in order to extrapolate to zero p_T. Spectra measured at the LHC are compared with RHIC results for Au-Au collisions at $\sqrt{s_{\rm NN}} = 200$ GeV (black empty markers). The spectral shape is significantly harder at the LHC with respect to RHIC [43], indicating that there is a significantly stronger radial flow.

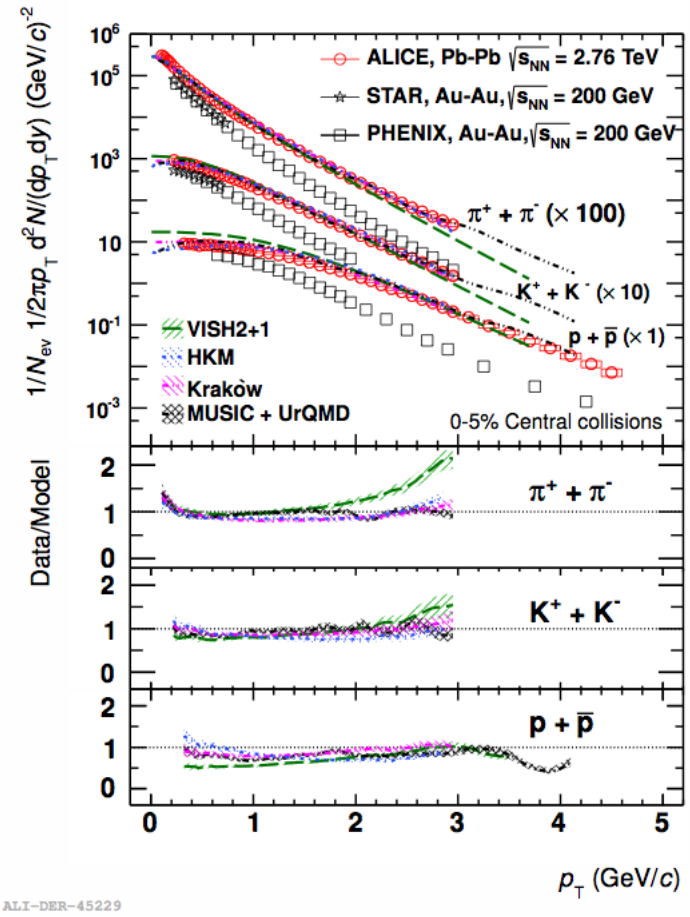

Figure 1.14: (color online) Transverse momentum distributions of the sum of positive and negative particles (box: systematic errors; statistical errors smaller than the symbol for most data points), fitted individually with a blast wave function, compared to RHIC data and hydrodynamic models [42].

Particle Ratios

The thermal description of hadron production was found to be successful over a broad range of energies (from $\sqrt{s_{\rm NN}} = 2$ GeV to $\sqrt{s_{\rm NN}} = 200$ GeV [44, 46]). The parameters which govern the thermal model are only three: the chemical freeze-out temperature T_{ch}, the baryochemical potential μ_B and the volume V. The identified particle yields measured by ALICE in Pb-Pb collisions at $\sqrt{s_{\rm NN}} = 2.76$ TeV have been used to compute particle ratios to be compared with the prediction of the thermal model [44, 45]. In order to

extract the parameters T_{ch}, μ_B and V, the thermal fit of integrated yields at mid-rapidity dN/dy in central (0-20%) Pb-Pb collisions, reported in Fig1.15 was performed. Here are also included results from strange and multi-strange particle analyses [47].

The temperature extracted from the fit $T_{ch} = 152 \pm 3$ MeV is lower with respect to the temperature one would expect considering T_{ch} constant above SPS energies (164 MeV). The prediction from the thermal model is reported with two different values of the freeze-out temperature: $T_{ch} = 164$ MeV (value obtained from fit to RHIC data) and $T_{ch} = 152$ MeV (from the fit described above). It was hypothezed that the interactions in the hadronic phase, in particular via the large cross section channel for antibaryon-baryon annihilation, could explain the significant deviation from the usual thermal ratios [43, 49]. As expected from particle production at LHC, there is a negligible

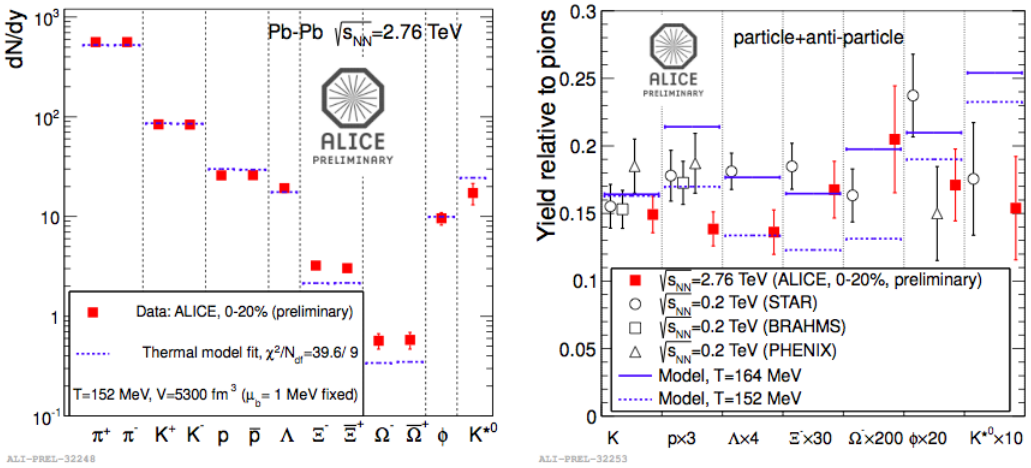

Figure 1.15: Left: integrated yields at mid-rapidity dN/dy in central (0-20%) Pb-Pb collisions at $\sqrt{s_{\rm NN}} = 2.76$ TeV with results from thermal fit. Right: integrated yields at mid-rapidity dN/dy in central (0-20%) Pb-Pb collisions relative to pions with RHIC comparison and thermal model predictions [43].

difference between the yield of particles and their antiparticles: antiparticle/particle integrated production ratios are observed to be consistent with unity for all particle species in all centralities. This suggests that the baryochemical potential μ_B is close to zero as expected at LHC energies.

1.2 Resonance production

Resonances are particles in an excited state that have the same quark content as their stable counterparts. Hadronic resonances decay strongly, thus they have a short lifetime, ranging from about 1 fm/c like the ρ meson (1.3 fm/c) to tenths of fm/c. The shortest lived states can be measured only via the reconstruction of their decay products in a detector. The decay products, or "daughters", may interact with the other particles of the expanding medium. This phenomenon, called re-scattering, results in the impossibility of reconstructing the resonance, because the invariant mass of the daughters does not match that of the parent particle. On the other hand, resonances may be regenerated as a consequence of pseudo-elastic collisions in the time lapse between the chemical (T_{ch}) and the kinetic freeze-out (T_{kin}). Re-scattering and regeneration (and the resonance yields) depend on the lifetime and temperature of the hadronic medium and on their individual cross section. The yield is decreased if the re-scattering dominates, vice versa the regeneration feeds the system with more particles. It has to be noted that since the resonance decay mainly into the same hadrons from which they were generated, the yield of stable hadrons itself is not modified.

Thermal models [53, 54, 55, 56, 57] can be used to predict particle ratios as functions of the chemical freeze-out temperature T_{ch} and the time between chemical and thermal freeze-out. An example of the time evolution of the chemical composition of an expanding fireball is shown in Fig.1.16 for Au-Au collisions at $\sqrt{s_{\mathrm{NN}}} = 200$ GeV as at RHIC [12]. UrQMD, a hadronic cascade model, was used. The time evolution is started here at the phase transition critical temperature T_c with chemical equilibrium particle abundances. Hyperons and resonances decay while the stable hadrons reach their final yields. The unstable particle abundances are not frozen at the chemical freeze-out, because of the re-scattering and regeneration processes. The hadron cross sections are in fact dominated by resonances, which means that processes like $n + N \rightarrow \Delta \rightarrow n + N$, $+ \rightarrow \rho \rightarrow +$, $+K \rightarrow K^{*0} \rightarrow +K$, and so on, happen frequently in the hadronic medium. These processes contribute to equilibrate the hadron momentum distribution with the decreasing temperature. Their

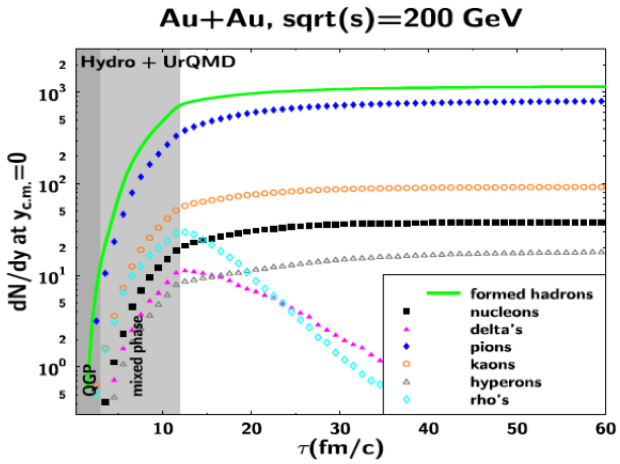

Figure 1.16: Evolution of the chemical composition of an expanding hadronic fireball produced in Au-Au collisions at $\sqrt{s_{\rm NN}} = 200$ GeV as a function of the medium proper time, from a UrQMD simulation. The expansion was started at the phase transition critical temperature T_c, with chemical equilibrium particle abundances [12].

abundances do not decrease with a exponential decay law, but more slowly thanks to resonance regeneration [4].

The study of resonances can provide information about the in-medium modifications of the intrinsic particle properties and on chiral symmetry restoration in the partonic and hadronic phases. If resonances are produced in the QGP, changes in their masses and/or widths may be observed [58, 59]. Hadronic states that are formed and decay within the lifetime of the partonic medium, experience in-medium interactions with the surrounding QGP, which may cause a resonance to dissociate, leading to a reduction in its lifetime, or an increase in its width. These resonance decay off-shell if chiral symmetry restoration reduces their mass. As previously discussed (see section 1.0.2), the chiral phase transition takes place nearly when the confined-deconfined matter transition occurs. This is suggested by the dependence from the critical temperature of the Polyakov loop and chiral condensate plotted in Fig.1.3. The presence of a partial chiral symmetry restoration effect can be investigated by studying intermediate momentum resonances, which are formed early and decay into particles that escape the partonic medium ad suffer of only little re-scattering and regeneration during the subsequent

hadronic medium expansion phase. Medium-induced effects may appear experimentally as reduced production rates, modification of the branching ratios, mass shifts and broadening of the widths in the QGP phase, that are expected to be detectable. The study of the $\phi(1020)$ and $K^{*0}(892)$[4] production is of particular interest. They both are mesonic resonances with close mass values (and close to the proton mass) but their lifetimes differ of about a factor 10, being $\tau_{\phi} = 46$ fm/c and $\tau_{K^{*0}} = 4.0$ fm/c. Also, their strangeness content differs by one unit. Among the two, the K^{*0} is expected to be more sensitive to the re-scattering effects in the hadronic medium, because of the much shorter lifetime. On the other hand, the ϕ escaping the medium with almost no re-scattering are good candidates to look for hints of partial restoration of the chiral symmetry at the formation time. In addition, the ϕ is a good candidate to probe strangeness production, being the lightest vector meson composed of sea quarks ($s\bar{s}$) only. In pp collisions, $s\bar{s}$ pair production was found to be significantly suppressed in comparison with $u\bar{u}$ and $d\bar{d}$ [61, 62]. In Pb-Pb the strangeness suppression effect is reduced, as described in section 1.1.2.

Below, some results on resonance production for d-Au collisions at RHIC, Fig.1.17, and pp and Pb-Pb collisions at LHC, Fig.1.18 and 1.19, are presented.

In Fig.1.17 (upper panel), $(K^{*0}+\overline{K^{*0}})/2$ and $(K^{*+}+K^{*-})/2$ invariant yields are reported as a function of p_T at $|y| < 0.5$. In the central panel and bottom panel of Fig.1.17 the K^{*0} mass and width respectively are reported; they refer to same same dataset as the one of the yields. In the upper panel, the solid line is the PDG K^{*0} mass (0.8961 GeV/c^2) [63]. The dashed line is the PDG $K^{*\pm}$ mass (0.8917 GeV/c^2) [63]. In the lower panel, the solid line is the K^{*0} and $K^{*\pm}$ widths (0.0507 GeV/c^2) [63]. The brackets indicate the systematic uncertainties [60]. In Fig.1.18, the transverse momentum spectra for K^{*0} and $\phi(1020)$ in pp collisions at $\sqrt{s_{\rm NN}} = 7$ TeV are reported, fitted with a Levy-Tsallis function (dashed line) [64]. In Fig. 1.19, the K^{*0} mass and width for

[4]For the sake of brevity, in the following ϕ will substitute $\phi(1020)$; K^{*0} will indicate both the $K^{*0}(892)$ and its antiparticle. When discrimination is necessary, the latter will be indicated as $\overline{K^{*0}}$.

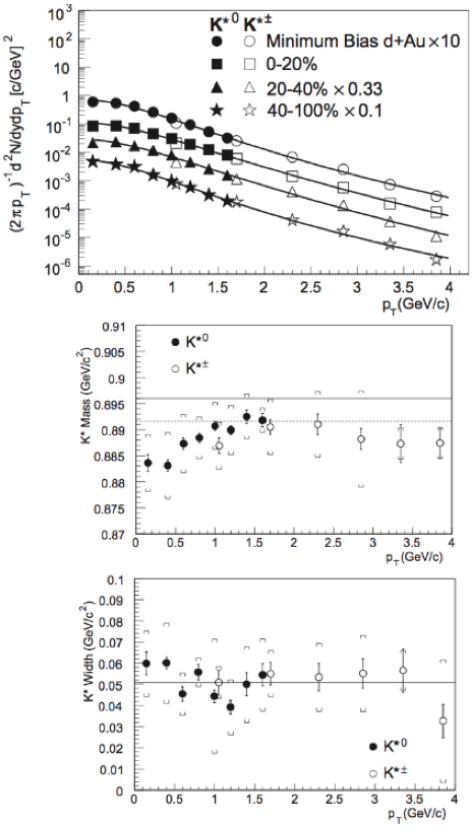

Figure 1.17: Top: The $(\mathrm{K}^{*0}+\overline{K^{*0}})/2$ together with the $(\mathrm{K}^{*+}+\mathrm{K}^{*-})/2$ invariant yields as a function of p_T at $|y| < 0.5$ for minimum bias d+Au collisions. Center and bottom: The K^{*0} mass and width as a function of p_T at $|y| < 0.5$ for minimum bias d+Au collisions.

centrality bins measured by ALICE in Pb-Pb collisions at $\sqrt{s_{\mathrm{NN}}} = 2.76$ TeV are reported.

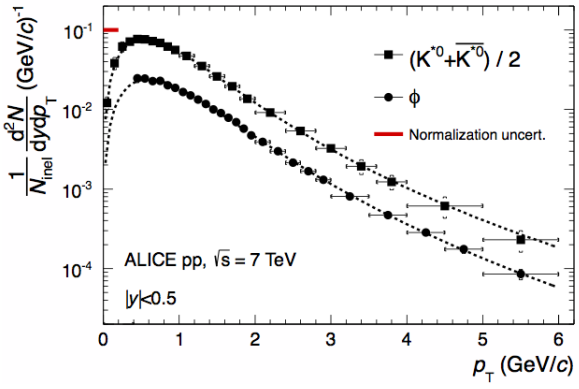

Figure 1.18: Transverse momentum spectra for K^{*0} and $\phi(1020)$ in pp collisions at $\sqrt{s_{\rm NN}}$ = 7 TeV. The statistical and systematic uncertainties are added in quadrature and the uncertainty due to normalization is shown separately. Each spectrum is fitted with a Levy-Tsallis function (dashed line) [64].

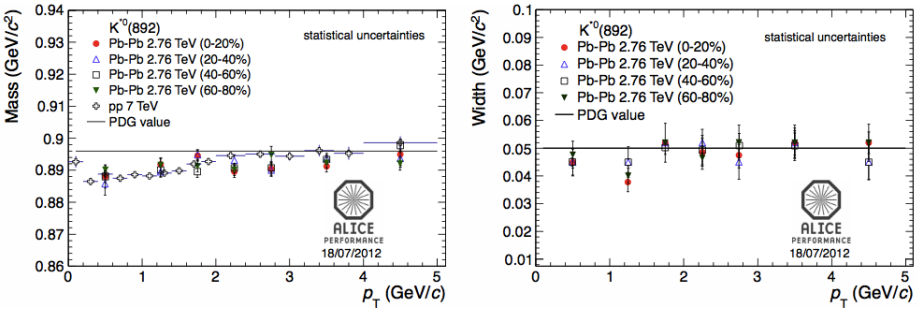

Figure 1.19: The K^{*0} mass and width in Pb-Pb collisions at $\sqrt{s_{\rm NN}}$ = 2.76 TeV measured by ALICE [59].

1.3 p-Pb collision in ALICE

In September 2012, the first (pilot) run with the proton-lead system took place at the LHC. Other collisions followed at the beginning of 2013 with both the possible configurations, p-Pb and Pb-p. In this section the first ALICE results from the p-Pb runs are presented in comparison to the results from pp and Pb-Pb runs.

1.3.1 Why p-A collisions

One of the most problematic uncertainties in heavy-ion collisions is the impossibility to separate initial from final-state medium effects. One of the main goals of the nucleon-nucleus run at the LHC is to exploit the different nature of the colliding beam to alter the relative importance of initial and final state medium effects, allowing for a better separation between them. The observables measured in p-Pb collisions are sensitive to final state rescattering and energy loss of partons traversing the nuclear medium. Thus, comparing these observables with those obtained from pp collisions, where no relevant cold nuclear matter effects or final state effects are present, and from Pb-Pb could give insights to resolve the aforementioned ambiguities. In addition, p-A collisions allow to test the Glauber model assumption that, when in a multiple hadronic scattering such as a collision between two nuclei (or a nucleon and a nucleus), the incident nucleon interacts with one target nucleon at a time. The other main goal of p-A collisions is to investigate the nuclear parton density function (nPDF). In the parton model, hard processes are described by convoluting the perturbatively calculated partonic cross sections with parton distribution functions (PDFs) for the description of the initial state and with fragmentation functions for the description of the hadronization process in the final state. The input parameters of the PDFs needed to evolve them to higher Q^2 are extracted from experimental data and several parametrizations have been developed. p-Pb collisions allow to reduce the uncertainties and attain more information on the differences between nuclear and proton PDFs, proving decisive to our understanding of

phenomenon such as, for example, the nuclear shadowing.

1.3.2 Particle production

Particle production in p-Pb collisions is expected to be sensitive to nuclear effects in the initial state. Different theoretical descriptions correspond to different models of particle production and, likewise, generate predictions of the charged-particle pseudorapidity density that may vary significantly. Thus, the measurements of particle production in p-Pb collisions constrain and potentially exclude certain models, and enhance the understanding of QCD at small x and of the initial state. Primary charged-particle pseudorapidity density in p-Pb at $\sqrt{s_{\mathrm{NN}}} = 5.02$ TeV (from Septermber 2012 pilot run) is shown in Fig.1.20 as measured by ALICE.

The $dN_{ch}/\mathrm{d}\eta_{lab}$ is measured in non single-diffractive (NSD) collisions for

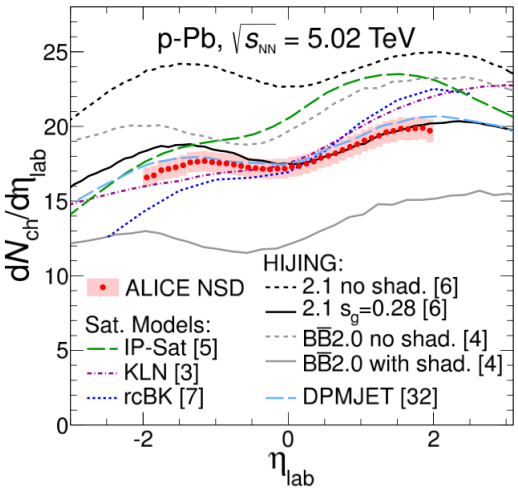

Figure 1.20: Pseudorapidity density of charged particles measured in NSD p-Pb collisions at $\sqrt{s_{\mathrm{NN}}} = 5.02$ TeV compared to theoretical predictions ([66] to [70]). The calculations [67, 68] have been shifted to the laboratory system [65].

$|\eta_{lab}| < 2$, where $\eta_{lab} = -\ln\tan(\theta/2)$ and θ is the polar angle between the charged particle direction and the beam axis z. A forward-backward asymmetry between the proton and lead hemispheres is clearly visible. The colored

lines are model calculations compared with the data: most of the models that include shadowing [69] or saturation [66, 70] predict the measured multiplicity values to within 20%. In particular, DPMJET [71] (normalized to NSD) and HIJING 2.1 [69], where the gluon shadowing parameter $s_g = 0.28$ was tuned to describe experimental data on rapidity distributions in d-Au collisions at $\sqrt{s_{\rm NN}} = 0.2$ TeV (RHIC) [72, 73], give values that are closest to the data. Both also describe the pseudorapidity shape relatively well, whereas the saturation models [66, 68, 70] exhibit a steeper η_{lab} dependence than the data [65].

In section 1.1.1 it was explained how partons losing energy in hot QCD matter cause a suppression in the production of charged hadrons at high-p_T. Experiments at RHIC have shown this suppression in Au-Au collisions [75, 76] in comparison to to the expectation from an independent superposition of nucleon-nucleon collisions (binary collision scaling). With p-Pb collisions, one can establish if the initial state of the colliding nuclei plays a role in the suppression of hadron production at high-p$_T$ that was also observed in Pb-Pb collisions at LHC. In Fig.1.21, the spectra of charged particles measured in NSD p-Pb collisions at $\sqrt{s_{\rm NN}} = 5.02$ TeV is compared with the interpolated pp reference spectrum [74].

In order to quantify nuclear effects in p-Pb collisions, the p_T-differential yield relative to the pp reference, an analogue of the nuclear modification factor, is studied. This is defined as

$$R_{pPb}(p_T) = \frac{d^2N_{ch}^{pPb}/d\eta dp_T}{\langle T_{pPb}\rangle d^2\sigma_{ch}^{pp}dp_T} \tag{1.9}$$

where N_{ch}^{pPb} is the charged particle yield in p-Pb collision, T_{pPb} is the overlap function for p-Pb collisions and σ_{ch}^{pp} is the charged particle cross section in pp collisions. The measurement of this quantity for $|\eta_{cms}| < 0.3$ is shown in Fig.1.22 [74]. R_{pPb} is here compared with the measurement of the nuclear modification factor of central (0-5% centrality) and peripheral (70-80% centrality) Pb-Pb collisions at $\sqrt{s_{\rm NN}} = 2.76$ TeV [79]. R_{pPb} is consistent with unity for $p_T \gtrsim 2$ GeV/c [74], demonstrating that the strong suppression observed in central Pb-Pb collisions [77, 78, 79] is not due to an initial-state

effect, but rather due the hot matter created in collisions of heavy ions.

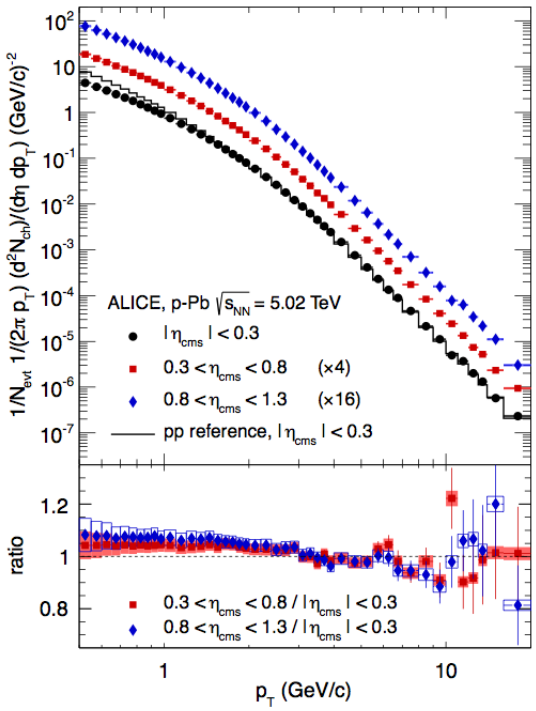

Figure 1.21: Transverse momentum distributions of charged particles in NSD p-Pb collisions for different pseudorapidity ranges (upper panel). The spectra are scaled by the factors indicated. The histogram represents the reference spectrum in pp collisions (see text). The lower panel shows the ratio of the spectra at forward pseudorapidities to that at $|\eta_{cms}| < 0.3$. The vertical bars (boxes) represent the statistical (systematic) errors [74].

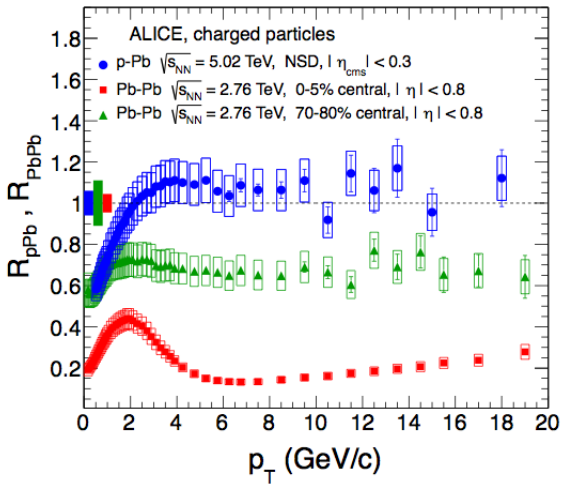

Figure 1.22: The nuclear modification factor of charged particles a function of transverse momentum in NSD p-Pb collisions at $\sqrt{s_{\rm NN}} = 5.02$ TeV. The data for $|\eta_{cms}| < 0.3$ are compared to measurements [79] in central (0-5% centrality) and peripheral (70-80%) Pb-Pb collisions at $\sqrt{s_{\rm NN}} = 2.76$ TeV. The statistical errors are represented by vertical bars, the systematic errors by (empty) boxes around data points. The relative systematic uncertainties on the normalization are shown as (filled) boxes around unity near $p_T = 0$ for p-Pb (left box), peripheral Pb-Pb (middle box) and central Pb-Pb (right box) [74].

Chapter 2

LHC and the ALICE experiment

The Large Hadron Collider (LHC) [80] is the world's largest and most powerful particle accelerator. It first started up on 10 September 2008 and it has been taking data for the last four years during pp runs at $\sqrt{s}$ = 900 GeV and 2.76, 7 and 8 TeV, during Pb-Pb runs at 2.76A TeV and during the p-Pb runs at 5.02A TeV.
On 14 February 2013 the Long Shutdown 1 (LS1) has begun and it will last for about two years. During this time, the detectors and the whole structure will undergo maintenance work in order to upgrade some of its components and prepare for LHC upgrade to design energies.
The LHC accelerator is briefly introduced in this chapter whose main purpose is to describe the ALICE detector. The ALICE detector layout will thus be treated in more detail. The central barrel detectors used in this analysis are described in sections 2.2.1 – 2.2.4. The last section of this chapter is dedicated to a short introduction of the ALICE offline framework, section 2.3.

2.1 The Large Hadron Colllider

The LHC [80] consists of a two-ring superconducting hadron accelerator and collider installed in the existing 26.7 km tunnel that was constructed for the CERN LEP machine. The two counter-rotating beams are curved and

kept on the desired path with a complex system of superconducting magnets. 1232 15m-long magnetic dipole bend the beams while 392 3m-long quadrupole focalize them. The magnets, cooled to a temperature below 2 K using superfluid helium and operating at fields above 8 T, are based on NbTi Rutherford cables, efficiently conducting electricity without resistance or loss of energy. The same accelerating machine is able to operate with both protons and heavy-ions beams. Protons are obtained by stripping electrons off an hydrogen atom. Lead ions are produced from a highly purified lead sample heated to a temperature of about 500°C. The lead vapor is ionized by an electron current and the lead ions are completely stripped of electrons too ($^{208}Pb^{82+}$). The particles (protons or nuclei) are accelerated through the sequence depicted in Fig.2.1: they are accelerated to 50 MeV in the LINAC2 (LINAC3 for Pb ions), and to 1.4 GeV in the booster. In the Proto-Synchrotron (PS) protons reach 25 GeV before being injected to the Super-Proto-Synchrotron (SPS), where they are accelerated up to 450 GeV. In the LHC ring protons/ions are finally accelerated to 3.5 TeV (or to 7 TeV at nominal energy).

The two beams are brought close to the speed of light before they are made to collide in the four interaction points of the main ring. In each interaction point, an extremely sophisticated experiment is placed in order to collect as much information as possible from the collision products. The four main experiments are ALICE [81], ATLAS [82], CMS [83] and LHCb [84].

The LHCb experiment is dedicated to precision measurements of CP violation and rare decays of B hadrons. ATLAS (A Toroidal LHC ApparatuS) and CMS (Compact Muon Solenoid) program comprehends the study of the Higgs physics and search for supersymmetric particles. ALICE (A Large Ion Collider Experiment) is a general-purpose, heavy-ion detector which focuses on QCD. It is designed to address the physics of strongly interacting matter and the Quark Gluon Plasma at extreme values of energy density and temperature reached in nucleus-nucleus collisions. Peculiar of this experiment are the capacity to cope with a very elevated multiplicity of events such as is the case with nuclei collisions, and the particle-identification capabilities that are of fundamental importance for the characterization of the produced

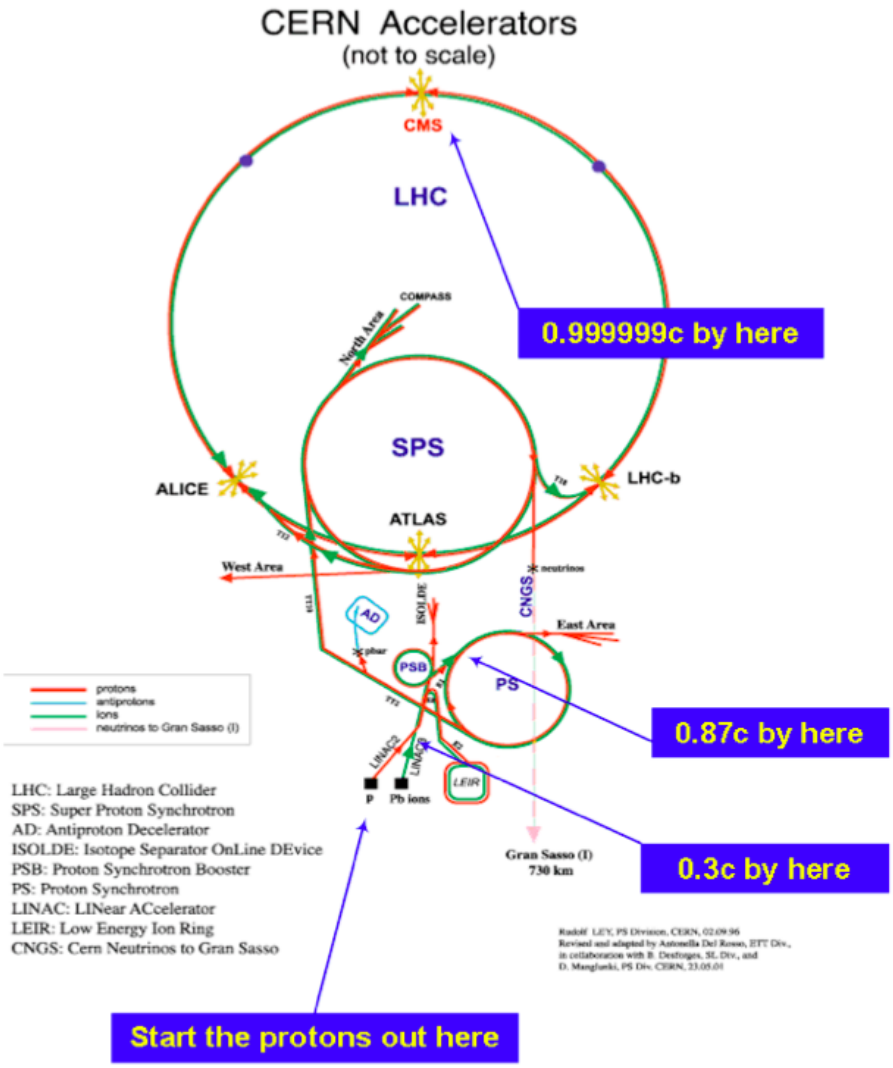

Figure 2.1: Scheme of the accelerating sequence of the *Large Hadron Collider*.

medium.

2.2 The ALICE experiment

ALICE is a general-purpose experiment, specialized in analyzing lead-ion collisions, whose detectors measure and identify mid-rapidity hadrons, leptons and photons produced in the interaction [81]. A unique design, with very

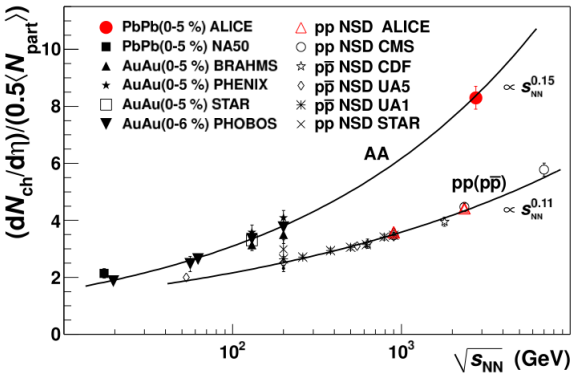

Figure 2.2: Charged-particle pseudorapidity density per participant pair for central nucleus-nucleus and nonsingle diffractive pp (p-$\bar{p}$) collisions, as a function of $\sqrt{s_{\rm NN}}$ [85].

different optimization than the one selected for the dedicated pp experiments at LHC, has been adopted for ALICE. In particular, ALICE is designed to track and identify particles from very low (∼100 MeV/c) up to fairly high (∼100 GeV/c) transverse momentum. ALICE, among other things, aims in fact to reconstruct short-lived particles such as hyperons, D and B mesons, and to perform these tasks in an environment with large charged-particle multiplicities, which has been measured to be up to $dN/dy \sim 1600$ charged particles per rapidity unit at mid-rapidity at $\sqrt{s_{\rm NN}} = 2.76$ TeV [85] (the design value for which the detector has been optimized is $dN/dy \sim 4000$ charged particles per rapidity unit at mid-rapidity), Fig.2.2.

The detection and identification of muons are performed with a dedicated spectrometer, including a large dipole magnet and covering a domain of large rapidities [1] (-4.0≤ $\eta \leq$ -2.4). Hadrons, electrons and photons are detected and identified in the central rapidity region (-0.9 $\leq \eta \leq$ 0.9) by a complex system of detectors operating in a moderate (0.5 T) magnetic field. From the

[1] In ALICE the coordinate axis system is a right-handed orthogonal Cartesian system with the point of origin at the beam interaction point. The axis are defined as follows: x-axis is perpendicular to the mean beam direction, aligned with the local horizontal and pointing to the accelerator centre; y-axis is perpendicular to the x-axis and to the mean beam direction, pointing upward; z-axis is parallel to the mean beam direction. Hence the positive z-axis is pointing in the direction opposite to the muon spectrometer.

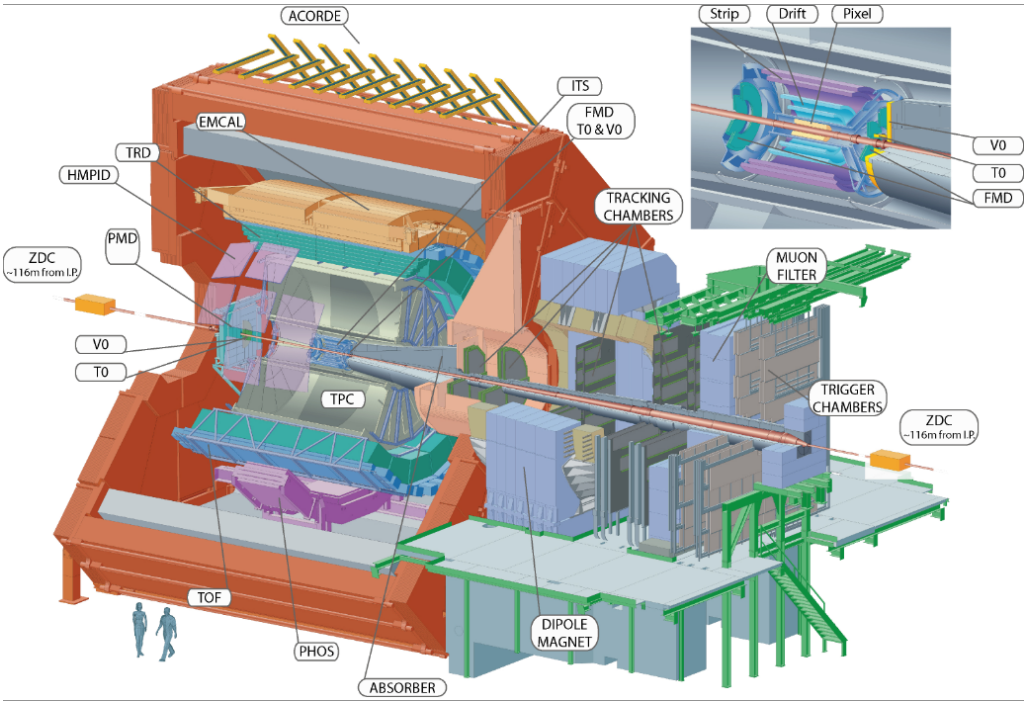

Figure 2.3: The ALICE detector.

inside out, the barrel contains an Inner Tracking System (ITS) of six planes of high-resolution silicon pixel (SPD), drift (SDD), and strip (SSD) detectors, a cylindrical Time-Projection Chamber (TPC), a Transition Radiation (TRD) and a Time-of-Flight system (TOF) that cover the full ϕ angle. Outside the TOF, a Ring Imaging Cherenkov (HMPID – High Momentum PID) and two electromagnetic calorimeters (PHOS and EMCal) cover a limited acceptance. The forward muon arm consists of a complex arrangement of absorbers, a large dipole magnet, and fourteen planes of tracking and trigger chambers. Several smaller detectors (ZDC, PMD, FMD, T0, V0) for global event characterization and trigger are located at small angles close to the beam pipe. An array of scintillators (ACORDE) on top of the L3 magnet is used to trigger on cosmic rays.

2.2.1 The Inner Tracking System (ITS)

The main tasks of the Inner Tracking System (ITS) are to localize the primary vertex with a resolution better than 100 μm, to reconstruct the secondary vertices from the decays of hyperons and D and B mesons, to track and identify particles with momentum below 200 MeV/c, to improve the momentum and angle resolution for particles reconstructed by the Time-Projection Chamber (TPC) and to reconstruct particles traversing dead regions of the TPC.

The ITS is located at radius between 4 and 43 cm, surrounding the LHC beryllium beam pipe that is 800 μm thick and has a radius of 2.9 cm. The detector layout has been designed taking into account the high multiplicity environment foreseen for central Pb-Pb collisions (a few thousands of particles per unit of rapidity were expected at the top energy), so that the occupancy is kept on the order of few percent. In order to accomplish this, Silicon Pixel Detector (SPD) have been chosen for the innermost two layers, and Silicon Drift Detectors (SDD) for the following two layers. The two outer layers are equipped with double-sided Silicon micro-Strip Detectors (SSD). The detector structure is represented in Fig.2.4 (left).

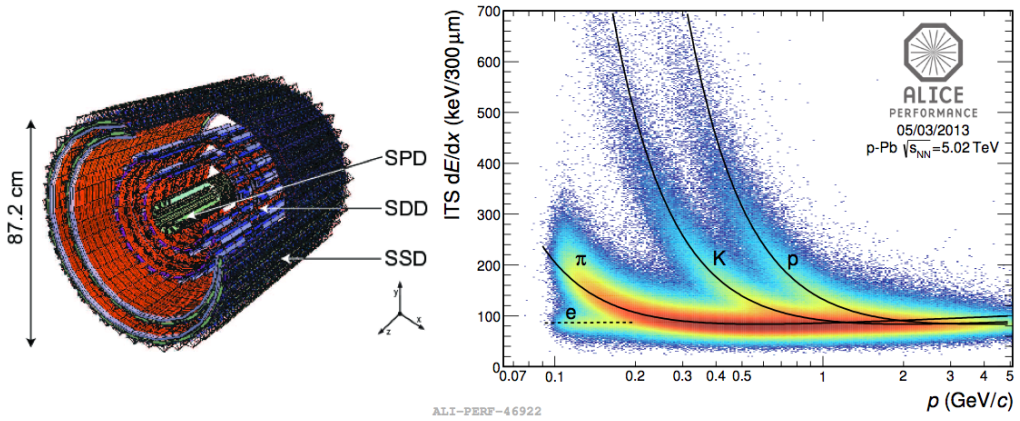

Figure 2.4: Left: The ALICE Inner Tracking System layers. Right: dE/dx distribution of charged particles as function of their momentum, both measured by the ITS alone, in p-Pb collisions at $\sqrt{s_{\rm NN}}$ =5.02 TeV. The lines are a parametrization of the detector response based on the Bethe-Bloch formula.

The SPD is based on hybrid silicon pixels, consisting of a two-dimensional matrix (sensor ladder) of reverse-biased silicon detector diodes bump-bonded to readout chips. In total, the SPD (60 staves) includes 240 ladders with 1200 chips for a total of 9.8 $\times 10^6$ read-out channels. Thanks to the high granularity the SPD has also been used for the trigger system, especially for the minimum bias event selection.
The Silicon Drift Detectors (SDD) constitute the two intermediate layers of the ITS. They have very good multitrack capability and provide two out of the four dE/dx samples needed for the ITS particle identification. They have a sensitive area of $70.17(r\phi)\times 75.26(z)$ mm^2 and a total area of 72.50×87.59 mm^2. The sensitive area is split into two drift regions by the central cathode strip to which a HV bias of ~ 2.4 kV is applied. Both outer layers use double sided SSD. The sensors are 300 μm thick and with an active area of $73(r)\times 40(z)$ mm^2. Each sensor has 768 strips on each side, almost parallel to the z beam axis direction, with a pitch of 95 μm. The stereo angle is 35 mrad which is a compromise between stereo view and reduction of ambiguities resulting from high particle densities.
The two layers of Silicon Strip Detectors (SSD) are crucial for the matching of tracks from the TPC to the ITS. They provide a two-dimensional measurement of the track position. In addition, the SDD provides dE/dx information, thus contributing to the particle identification for low-momentum particles. The system is optimized for low mass in order to minimize multiple scattering.

2.2.2 The Time Projection Chamber (TPC)

The Time-Projection Chamber (TPC) is the main tracking detector of the central barrel and is optimized to provide, together with the ITS, charged-particle momentum measurements with good two-track separation, particle identification, and vertex determination.
The phase space covered by the TPC in pseudo-rapidity is $|\eta| < 0.9$ for tracks with full radial track length (matches in ITS, TRD, and TOF detectors); for

reduced track length (at reduced momentum resolution), an acceptance up to about $|\eta| = 1.5$ is accessible. The full azimuth is covered.
The TPC is cylindrical in shape; the active volume has an inner radius of about 85 cm, an outer radius of about 250 cm, and an overall length along the beam direction of 500 cm. The detector is made of a large cylindrical field cage, filled with 90 m^3 of $Ne/CO_2/N_2$ (90%/10%/5%), in which the primary electrons are transported over a distance of up to 2.5 m on either side of the central electrode to the end plates. Multi-wire proportional chambers with cathode pad readout are mounted into 18 trapezoidal sectors at each end plate. A central cathodic plane divides the TPC in two drift regions.
After ionization by a charged particle, the electrons drift toward the endcap readout planes. The electron drift velocity of 2.7 cm/μs over 250 cm (each of the two TPC drift region separated by the central cathode) gives a maximum drift time of 88 μs, therefore setting a limit on the event rate sustainability of the TPC. At high interaction rate the pile-up effect becomes relevant. Another limiting factor is the long TPC dead time, that slows down the readout frequency. In Fig. 2.5 the TPC structure scheme and an example of the TPC particle identification is reported.
The TPC can measure track transverse momentum over a wide range, from about 0.1 GeV/c up to 100 GeV/c with good momentum resolution and efficiency (ϵ >90% for p_T >100 MeV/c, where the limiting factor are the interactions in the ITS material. By measuring the deflection in the magnetic field, the ITS and the TPC are able to determine the momentum of the charged particles with a resolution better than 1% at low p_T and better than 20% for p_T ~100 GeV/c. The momentum measurement and the dE/dx information allow to separate the various charged particle species in the low momentum region. Thanks to its good dE/dx resolution (5.7%, close to the design value of 5.5% [86]), the TPC can identify particles with p_T <1 GeV/c. In Fig. 2.5 (left) an example of the TPC detector performance is reported.

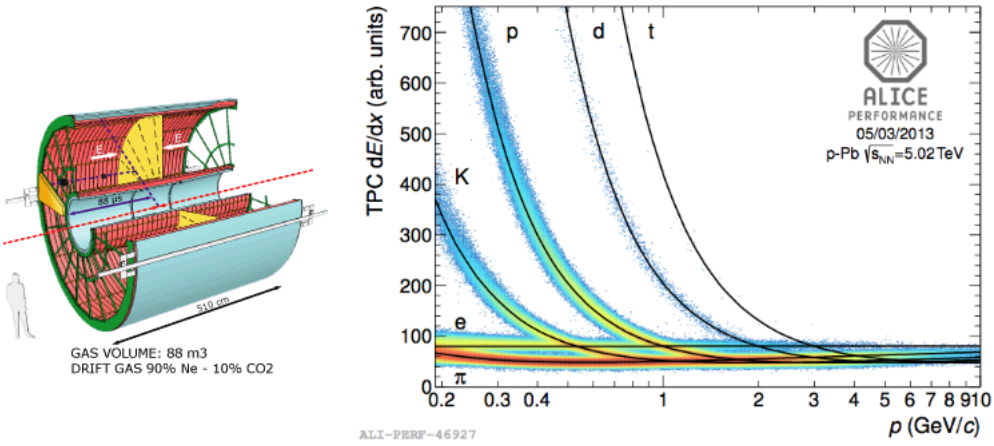

Figure 2.5: Left: The ALICE TPC internal structure. Right: dE/dx of charged particles vs their momentum measured by the TPC in p-Pb collisions at $\sqrt{s_{\rm NN}} = 5.02$ TeV. The lines are a parametrization of the detector response based on the Bethe-Bloch formula.

2.2.3 The Time-Of-Flight (TOF)

The Time-Of-Flight (TOF) detector is a large area MRPC array. It is dedicated to charged Particle IDentification (PID) in the intermediate momentum range, below about 2.5 GeV/c for pions and kaons, up to 4 GeV/c for protons, with a p/K and K/p p_T-dependent separation better than 3σ. The TOF covers the central pseudo-rapidity region ($|\eta| \leq 0.9$) and can provide also event-by-event identification of large samples of pions, kaons, and protons. In addition, at the inclusive level, identified kaons allow invariant mass studies, in particular the detection of open heavy-flavoured states, vector-meson resonances such as the ϕ meson and strange mesons like the K^{*0}.
The design of the Time-Of-Flight system is made to cope with a very high charged-particles density and counts more than 10^5 independent TOF channels.
A gaseus detector, the Multi-gap Resistive-Plate Chamber (MRPC), was chosen to cover the large sensitive area. A schematic view of one TOF double-stack MRPC can be seen in Fig.2.6.

The basic unit of the TOF system is a 10-gap double-stack MRPC strip.

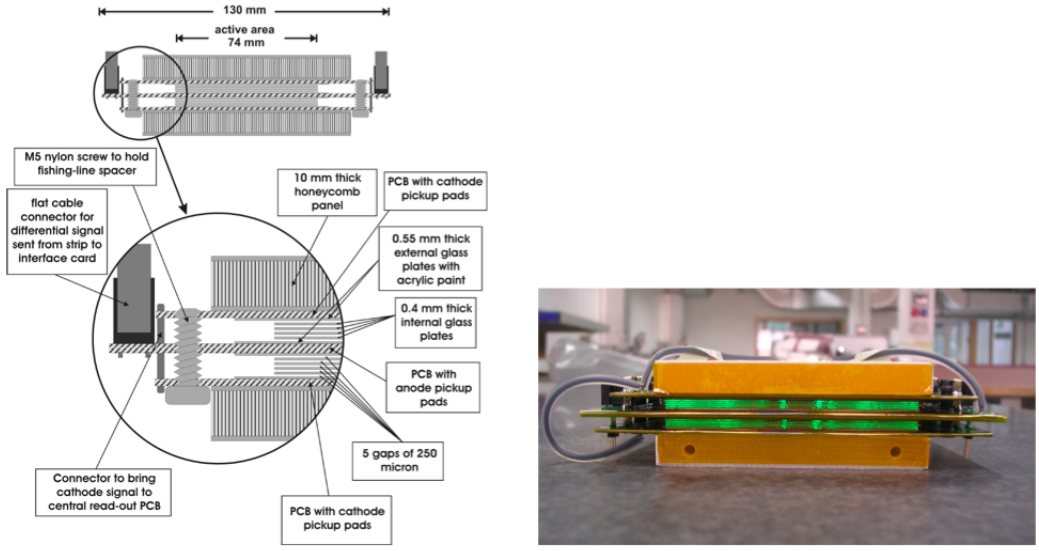

Figure 2.6: Schematic cross section (left) and photograph (right) of a 10-gap double-stack MRPC strip [81].

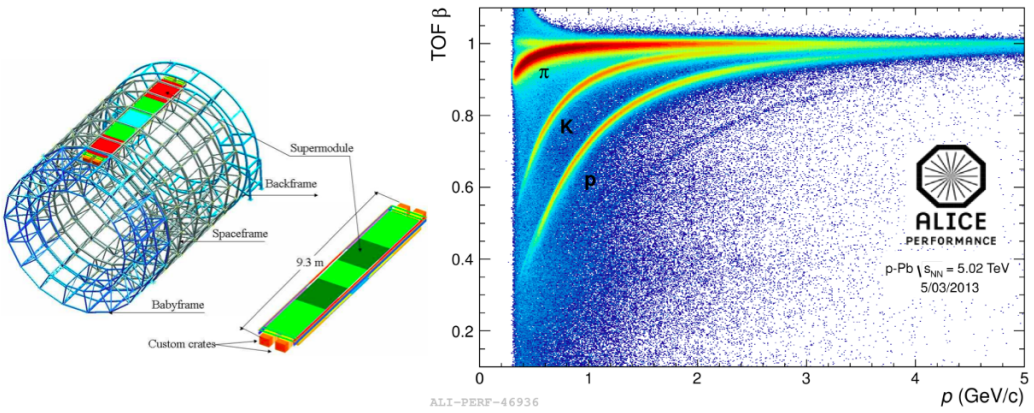

Figure 2.7: Left: The ALICE TOF modular structure. Rigth: TOF β-p performance in the p-Pb run at 5.02 TeV.

Each MRPC strip is 122 cm long and 13 cm wide, with an active area of 120×7.4 cm^2 subdivided into two rows of 48 pads of 3.5×2.5 cm^2 size. In order to minimize the transversal path of the incident particles through the chamber strips (that could increase the occupancy and the time jitter of the detected signals), an *ad hoc* tilted positioning of the strips was devised. Since

each MRPC is composed of 96 readout pads, the TOF detector consists of 152928 readout channels covering a total area of 138 m^2. The key aspect of these chambers is that the electric field is high and uniform over the full sensitive gaseous volume of the detector. The electrode planes operate at a nominal d.d.p. of 13.5 kV [81]. Any ionization produced by a traversing charged particle immediately starts a gas avalanche process which generates the observed signals on the pick-up electrodes. There is no drift time associated with the movement of the electrons to a region of high electric field and thus the only time jitter of these devices is caused by the fluctuations in the growth of the avalanche. The signal produced is the analogue sum of signals from many gaps and it is a peak well separated from zero. Data collected in the first year of operation show the MRPC performs with an intrinsic resolution better than about 40 ps, as from design, and an efficiency close to 100% can be reached [87].
The TOF is inscribed in a cylindrical shell with an internal radius of 370 cm and an external one of 399 cm. The detector has a modular structure corresponding to 18 sectors in ϕ and to 5 segments in z direction. Every module of the TOF detector consists of a group of MRPC strips (15 in the central, 19 in the intermediate and in the external modules) closed inside a box that defines and seals the gas volume and supports the external front-end electronics and services. The complete TOF system consists of 90 modules, laid out so that the joining areas of the modules are aligned with the dead areas of the other detectors projected from the interaction point, thus creating a configuration of minimal disturbance for the external detectors.
Figure 2.7 shows the TOF modular structure and the TOF performance expressed as a β versus momentum plot for a p-Pb run at 5.02 TeV. More details on the TOF performance are discussed in section 3.2.

2.2.4 The V0 and T0 detectors

The V0 detector is a small angle detector consisting of two arrays of scintillator counters, called V0A and V0C, which are installed on either side of

the ALICE interaction point. The V0A detector is located 340 cm from the vertex (interaction point – IP) on the side opposite to the muon spectrometer whereas V0C is fixed to the front face of the hadronic absorber, 90 cm from the vertex. They cover the pseudo-rapidity ranges $2.8 < \eta < 5.1$ (V0A) and $-3.7 < \eta < -1.7$ (V0C).
The V0 has provided minimum-bias triggers for the central barrel detectors in pp, Pb-Pb and p-Pb collisions. These triggers are given by particles originating from initial collisions and from secondary interactions in the vacuum chamber elements (beam-gas interaction). Since the dependence between the number of registered particles on the V0 arrays and the number of primary emitted particles is monotone, the V0 is also used as an indicator of the centrality of the collision via the multiplicity recorded in the event. More specific details on how the centrality is obtained in ALICE are reported in [88].
It has to be noted that while the definition of centrality in Pb-Pb collisions can be easily extracted from the collision geometry, in p-Pb collisions the relation between the two quantities is not linear and the definition of the centrality requires deeper studies on the dynamic of the collision. A more exhaustive explanation can be found in chapter 3.

The function of the T0 detector is to generate a start time (T0) for the TOF detector. This time corresponds to the real time of the collision (plus a fixed time delay) and it is independent of the interaction point position. The precision of this signal is about 50 ps (r.m.s.). Moreover, the T0 can measure the vertex position (with a precision ± 1.5 cm) for each interaction and can provide a Level 0 (L0) trigger when the vertex position is within preset values. This helps to discriminate beam-gas interactions. The T0 can also generate an early (prior to L0) "wake-up" signal to the TRD, provide redundancy to the V0 counters and generate minimum bias and multiplicity triggers.
The detector consists of two arrays (T0A and T0C) of Cherenkov counters, 12 counters per array. Each counter is based on a fine-mesh photomultiplier tube, optically coupled to a quartz radiator with 20 mm diameter and 20 mm

thickness. Like the V0, T0A is placed at 375 cm from the IP on the opposite side with respect to the muon spectrometer, while T0C is located just in from of the absorber, at 72.7 cm from the IP.

2.3 ALICE offline framework

The Grid is a distributed computing infrastructure of shared resources adopted by CERN to manage the enormous flow of data produced by the LHC and the computational work their elaboration requires. The Grid also allows the community of physicists all over to world to access the data in almost real time. The ALICE Collaboration has developed the AliEn (ALICE Environment) framework [89] to reconstruct and analyze the data in this distributed environment. AliEn provides a global file system, or catalogue, for data storage and an interface to execute the jobs on the Grid. Alongside the Alien interface there is the ALICE offline framework (AliRoot) [90], an object-oriented software framework, based on the ROOT system [91]. Entirely written in C++, except for a few internal modules in FORTRAN, the framework gives to the user the flexibility to perform Monte Carlo simulation, reconstruction, calibration and analysis with the same tool. Through the Grid, the user can split the analysis jobs in many identical sub jobs that run in parallel on different computer nodes. In addition to routine analysis, the user can implement his custom analysis code. The analysis presented in this thesis has been carried on with these tools and with a custom analysis code.
Below, few more details on simulation and reconstruction are given.

Simulation The simulation of physics events is of fundamental importance for any analysis and for evaluating the efficiency of the algorithms applied to reconstruct and analyze data as it has been done for the analysis presented in chapter 3.
In a realistic simulation the particles produced in a given collision are propagated inside the detector. As a consequence, effects like material absorption, acceptance, detector configuration and response should be taken into

account. Monte Carlo generators, like HIJING [92], PYTHIA [93] and DPMJET [94], are used for particle production in the simulated collision. The generated particles are propagated through the sensitive regions of the detector, where they decay, loose energy, interact with detector material, producing other particles or being absorbed. The ALICE detector layout, including geometry, position, structure and material is reproduced by using the ROOT libraries. The interaction of the particle with the material is simulated by the GEANT3 [96], GEANT4 [97] and Fluka [98] packages. Simulated hits in the detector are translated finally into the same format as the raw data, so that the same tracking algorithm as real data reconstruction is used.

Reconstruction In order to obtain a particle track in the detector, a reconstruction procedure is needed in order to gather and assemble the single hits in the detector sensible volume. The first step of the reconstruction is a local cluster finding procedure. The hit signals on a detector section are combined together into a single cluster to better estimate the position of traversing particle and reduce the effect of the random noise. ALICE exploits the Kalman Filter algorithm [99] for simultaneous track finding and track fitting. The ALICE track reconstruction is based on the following steps [101]:

- the clusters in the two ITS inner layers are used to give the primary vertex position [102, 103] needed by the Kalman filter to build the track "seeds" that are used as starting points;

- the track finding proceeds in the TPC from the outer to the inner part, from lower to higher track multiplicity. The clusters on the outermost pad rows and the primary vertex position from previous step are used as seed. A limited number of TPC cluster is associated to the track with the "center of gravity" method;

- track following is performed for each seed applying a constraint on the primary vertex, in order to maximize the efficiency for primary tracks.

Starting from the higher-momentum candidates, the TPC tracks are matched to the SSD layers and with ITS points down to the innermost SPD layer. The track is then back-propagation and refitted outward in ITS and TPC, up to the outer radius of the TPC;

- the track is extrapolated and matched in the TRD. Then follows the propagation to the outer layer to the PID detectors, TOF, HMPID, PHOS and EMCal;

- reconstructed tracks are refitted inwards through TRD, TPC and ITS and re-propagated to the primary vertex. The track parameters are evaluated in proximity of the vertex. The primary vertex position is finally recalculated using tracks to obtain the optimal resolution.

The output of the whole reconstruction procedure is the Event Summary Data (ESD) which contains all the information about the event both at track and event level. In order to allow a more efficient analysis a summary of the most relevant information is extracted from the ESDs in the format of Analysis Object Data (AOD). For each data sample, the files containing ESD and AOD are stored and distributed worldwide on the Grid, where the users can access them through AliEn.

Chapter 3

Measurement of the $K^{*0}(892)^0$ in p-Pb collisions

In heavy-ion collisions resonances are short-lived particles that decay in a interaction-rich expanding medium. The decay products, or "daughters", may re-scatter with the other particles of this medium or regenerate the "mother" particle through pseudo-elastic collisions. Since re-scattering and regeneration depend on the lifetime and temperature of the hadronic medium and on their individual cross section, resonant particles and their decay products can be proficiently used as probes for the properties of the medium at different stages and for pinpointing the time lapse between chemical (T_{ch}) and kinetic freeze-out (T_{kin}).

The K^{*0} resonance production presented here is measured at central rapidity ($0 < y_{CM} < 0.5$) in p-Pb collisions at 5.02 TeV with the ALICE experiment. The hadronic decay product, $K\pi$, is identified with both the Time Projection Chamber and Time-Of-Flight detectors through the nσ-cut method (see section 3.4.3). The invariant mass of the resonance is reconstructed and the yields are compared with the yield of the stable particle, the kaon.

3.1 Particle identification with the ALICE TPC

Particles identification with the TPC makes use of the simultaneous measurement of the momentum p of a particle and its specific ionization loss (dE/dx) in the gas of the TPC [104]. The measurement is done over a wide momentum range and only the relative values of the ionization need to be known to distinguish between different particle species. The information on the energy loss for a given track is extracted from the number of clusters (raging from a minimum of 50 cluster to a maximum of 160) which are assigned to the track during the tracking procedure.
The energy loss is described by the Bethe-Bloch function:

$$\langle \frac{dE}{dx} \rangle = \frac{4\pi N e^4}{mc^2} \frac{Z^2}{\beta^2} \left(\ln \frac{2mc^2\beta^2\gamma^2}{I} - \beta^2 - \frac{\delta(\beta)}{2} \right) \tag{3.1}$$

where mc^2 is the rest energy of the electron, Z the charge of the projectile, N the number density of electrons in the traversed matter, e the elementary charge, β the velocity of the projectile and I is the mean excitation energy of the atom. The most significant quantity for the particle identification is the resolution of the energy loss measurement. The resolution $\sigma_{dE/dx}$ depends on the number of samples, the pad size and the gas pressure while the energy loss distribution depends only on the cluster-size distribution and on the number of primary interactions in the gas. TPC can measure track transverse momentum from about 0.1 GeV/c up to 100 GeV/c with momentum resolution better than 1% at low p_T and better than 20% for p_T ~100 GeV/c. The resolution on the dE/dx is 5.7%, close to the design value of 5.5% [86].

3.2 Particle identification with the ALICE TOF

The Time-Of-Flight particle identification (PID) helps to extend the ALICE π/K and K/p discrimination power to higher p_T with respect to the TPC [52]. The following ingredients are of fundamental importance for the TOF performance:

- the TPC-TOF matching efficiency
- the optimal calibration of the TOF signal
- the knowledge of the single-event interaction time (t_0) with the best possible resolution

The matching efficiency is the probability that a track is associated to a hit on the TOF sensitive area; therefore, it represents the first requirement to attempt identification via time-of-flight. A good calibration of the TPC *per se* is important to have the best possible resolution on the momentum p and the track length, L. The time calibration and the t_0 (for further detail, see section 3.4.3) information are needed to achieve the best possible overall resolution on the time-of-flight measurements.
One of the possible PID strategies that exploit TOF is based on the discriminating variable $N_{\sigma,i}^{TOF}$, defined as:

$$N_{\sigma,i}^{TOF} = \frac{t - t_0 - t_{exp,i}}{\sigma_{PID,TOF}} \tag{3.2}$$

where i indicates the particle species ($i = \pi$, K, p, ...), t is the measured TOF hit time, t_0 is the interaction time, $t_{exp,i}$ is the expected time of flight computed during the central tracking procedure. The total resolution, $\sigma_{PID,TOF}$, is the sum of the following contributions:

$$\sigma_{PID,TOF} = \sqrt{\sigma_{TOF}^2 + \sigma_{timeZero}^2 + \sigma_{trk}^2} \quad . \tag{3.3}$$

The expected times depend on the mass hypothesis, but also on the measurement of the particle momentum and the track length during the tracking procedure. These globally contribute with σ_{trk}. The resolution of the interaction time, $\sigma_{timeZero}$, depends on how the t_0 is measured in ALICE, among three possible ways: as the average event time of the fill, with the T0 detector or with an algorithm involving tracks with hits on TOF. In Eq. 3.2 this contribution has been distinguished from σ_{TOF} because if the first two strategies are used, the resolution is independent of the TOF performance. In this analysis, the start time of the event has been estimated from a weighted

mean of the start time computed from the T0 and TOF algorithm ($T0best$). Finally, σ_{TOF} is the resolution on the time measurement, for which the TOF design has been optimized in order to get $\sigma_{TOF} < 100$ ps. Fig. 3.1 shows the total time resolution for pion tracks on TOF as a function of the number of tracks used to define the TOF event time. The TOF time resolution is σ_{TOF} = 80 ± 0.2 ps. The overall TOF resolution is found to be about 85 ps for pions with p_T = 1 GeV/c.

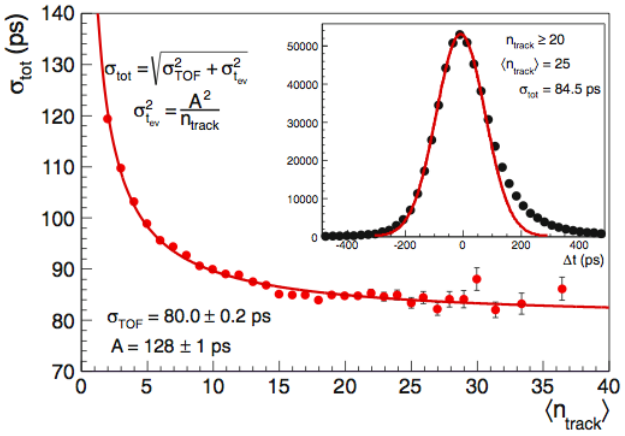

Figure 3.1: Total time resolution for pion tracks on TOF with $0.95 < p < 1.05$ GeV/c as a function of the number of tracks used to define the TOF event time. Data refer to p-Pb collisions. The inset shows the original distribution for a track multiplicity on TOF $n_{track} > 20$ which corresponds to an average of $\langle n_{track} \rangle = 25$ [87].

3.3 TOF matching efficiency

The ALICE tracking algorithm has been described in section 2.3. After the propagation through TPC and TRD, the tracks are extrapolated to the TOF sensitive layer. A geometrical matching window of 3 cm (for Pb-Pb collisions) or 10 cm (for pp and p-Pb collisions) is opened around the intercept of the extrapolated track with the TOF sensitive layer. The algorithm looks for TOF clusters within this matching window and if any is found, the closest

hit to the crossing point is associated to the track. The "matched" track is then propagated to the TOF layer.
The matching efficiency is estimated as

$$\epsilon_{match} = \frac{\text{Number of reconstructed tracks with an associated TOF hit}}{\text{Number of reconstructed tracks}}. \tag{3.4}$$

Fig. 3.2 shows the TOF matching efficiency for different particle species

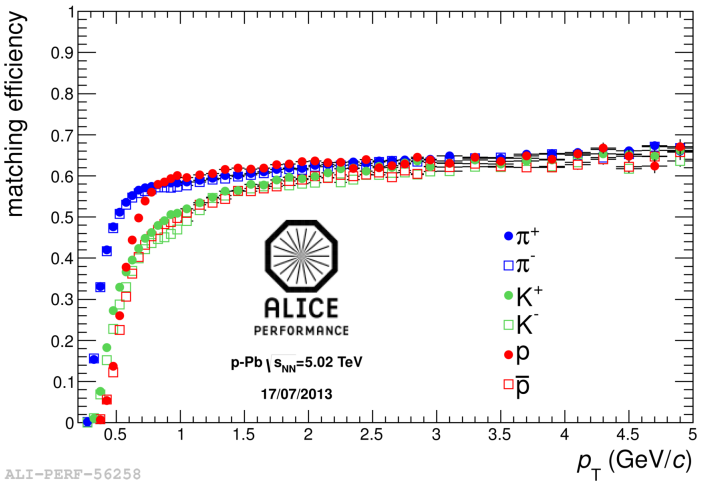

Figure 3.2: TOF matching efficiency for pions, kaons and protons in p-Pb collisions at $\sqrt{s_{\rm NN}} = 5.02$ TeV.

in p-Pb collisions at $\sqrt{s_{\rm NN}} = 5.02$ TeV. Fig. 3.3 shows the comparison between the TOF matching efficiency measured in p-Pb collisions and the one extracted from the corresponding simulation.
Clearly the interest is to have the TOF track matching efficiency as high as possible, while keeping the number of mismatched tracks as small as possible. The mismatched tracks are those matched with a wrong TOF hit. Tracks with $p_T < 0.3$ GeV/c do not reach the TOF due to the trajectory curvature in the magnetic field. For $p_T > 0.3$ GeV/c ϵ_{match} increases until it saturates for $p_T > 1$ GeV/c.
Finally, the matching efficiency has to be reproduced correctly in the Monte Carlo simulation, to reflect the detector response and be used as correction

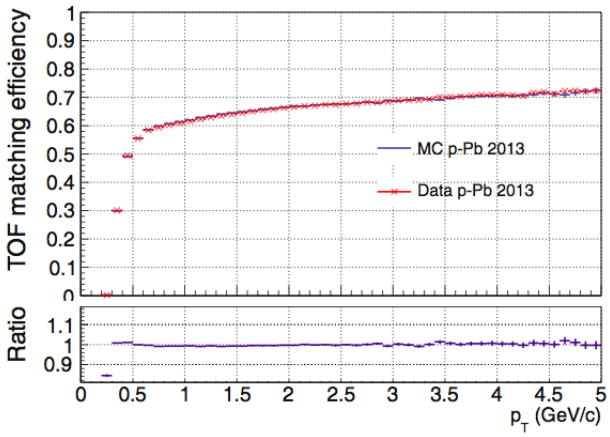

Figure 3.3: Comparison between the TOF matching efficiency measured in 2013 p-Pb data and the one extracted from the corresponding simulation (top). The bottom plot shows their ratio [87].

factor for any analysis on particle production. It has been verified that the Monte Carlo matching efficiency for positive and negative particles, reproduces the measured one within a few percent, as shown in the bottom plot of Fig. 3.3.

3.4 The K^{*0} resonance production analysis

The K^{*0} is a short-lived resonance with lifetime $\tau = 4$ fm/c, mass $m_{K^{*0}} = 0.896$ GeV/c^2 and width $\Gamma \sim \hbar/\tau = 0.0478$ GeV/c^2. In the analysis presented here, the resonance is reconstructed from the hadronic decay $K^{*0} \rightarrow K^{\pm} + \pi^{\mp}$ (branching ratio BR = 66.6%).

The analysis uses the data collected during the p-Pb run at $\sqrt{s_{\rm NN}} = 5.02$ TeV in January 2013 by the ALICE detector in the pseudorapidity range $|\eta| < 0.8$.

The invariant mass of the particle is reconstructed by combining identified kaons and pions into pairs identified as candidates for being the resonance decay products. From the fit of the invariant mass distribution, the raw yields are extracted and normalized to the number of events. The raw yields

normalization, the corrections for the efficiency, rapidity and for the resonance branching ratio are applied in order to obtain the K^{*0} cross section.

3.4.1 Event selection

The data sample consists of minimum bias events, selected exploiting the SPD and V0 detectors trigger. The event selection requires a primary vertex reconstructed in the SPD or with TPC tracks and whose z coordinate of the primary vertex (v_z) falls within ± 10 cm from the interaction point. The initial sample consists of about 125×10^6 events, while the number of accepted events that survive the event selection is $\sim 100 \times 10^6$.
The centrality estimator chosen for this analysis is the VZERO amplitude on the Pb direction (V0A). In Pb-Pb collisions, the centrality is defined as a fraction of the Pb-Pb hadronic cross section and it represents the geometrical superposition of the two colliding nuclei. When the two nuclei collide frontally, the collision is said "central", with high particle multiplicity and small impact parameter. On the other hand, in a peripheral collision, the impact parameter is large and the particle multiplicity lower. The more peripheral the collision, the less overlapped are the nuclei. Proton-lead collisions inherit this centrality definition [88]. In Fig.3.4 the centrality distribution for the accepted events is reported.
The centrality of the events is integrated over the whole p_T range for each of the measurements shown in this work. The subdivision in centrality classes has been only used for the cross check study of the event mixing background estimation, described in section 3.8.

3.4.2 Track selection

The candidate daughters are selected among the tracks coming from the primary vertex, called primary tracks, combining information from the ITS and TPC. In order to be well within the pseudo-rapidity region covered by the detectors involved in the particle identification (TPC and TOF) the tracks

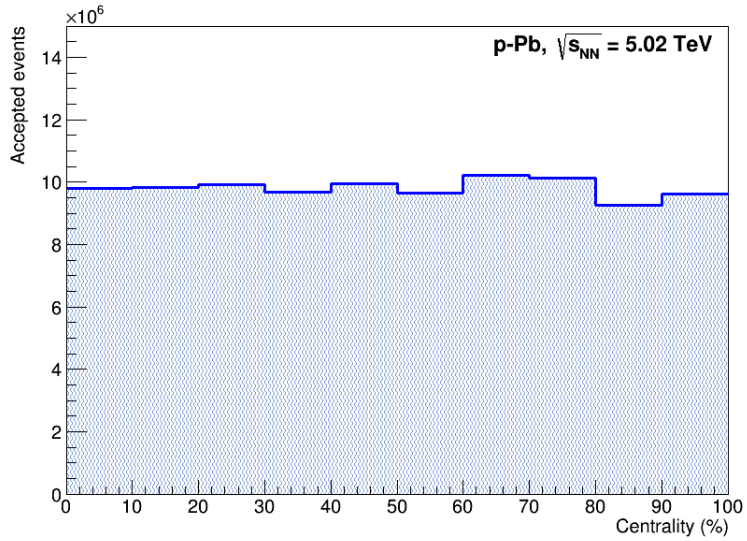

Figure 3.4: Centrality distribution of the accepted events.

are selected to have $|\eta| \leq 0.8$. Moreover, an additional request on the particle transverse momentum derives from the TOF matching: for p_T <0.3 GeV/c the track are rejected due to the magnetic field effects (see section 3.3). To be eligible, the tracks also have to pass a number of selection criteria. The selection criteria, called "standard quality cuts", employ parameters estimated during the reconstruction in the ITS and TPC to choose tracks of good quality. In order to select only the tracks pointing to the primary vertex, at least one cluster in the SPD is required, together with a limitation on the distance of closest approach (DCA). The DCA is the minimum distance between two tracks trajectories, that is ideally zero if the two tracks come from the same point. The resolution on the DCA is determined by the detector resolution on the track position measurement. For this analysis it is required that the component in the direction parallel to the beam is $\mathrm{DCA}_z < 2.0$ cm, while the component in the radial direction must satisfy the relation $\mathrm{DCA}_r(p_T) < 0.0105 + 0.0350$ GeV/c $\cdot p_T^{-1.1}$ cm, that takes into account the deflection of the trajectories in the magnetic field. The other requests are:

- a maximum value of chi-squared for the ITS cluster fitting (from Kalman

filter), $\chi^2 = 36$;

- a minimum number of cluster associated to the track in the TPC, $N_{cls} \geq 70$;
- a minimum of 0.8 for the ratio of the crossed rows[1] over the number of findable clusters[2];
- a maximum value of chi-squared for the TPC cluster fitting (from Kalman filter), $\chi^2 = 4.0$;
- a maximum value of chi-squared for the TPC constrained global tracks (from Kalman filter), $\chi^2 = 36.0$;
- a successful refit of the reconstruction algorithm, from the outer layer of the detector to the primary vertex, through TPC and ITS;
- rejection of daughters from "kink" decays (such as $K^{\pm} \rightarrow \mu^{\mp} + \nu$).

An additional request for the daughter pairs rapidity in the range $0 < y_{CM} < 0.5$ is necessary in order to select the region in which the detector acceptance is uniform.
The system p-Pb is asymmetric, thus, y_{cms} and y_{lab} do not coincide as in the Pb-Pb case. The shift of the CMS is of Δy = - 0.465 in the direction of provenience of the lead nucleus, towards the muon spectrometer. Since the positive rapidity is defined as the Pb beam direction, the rapidity transformation is

$$y_{lab} = y_{cms} + \Delta y = y_{cms} - 0.465. \tag{3.5}$$

Thus, the cut for the selection of the pairs at midrapidity $0.0 < y_{cms} < 0.5$ in the CMS becomes $-0.465 < y_{lab} < 0.035$ in the laboratory system.

[1]The crossed rows are the number of rows in the TPC that the traversing particle intercepts. This is a relevant quantity for the p_T resolution of a track since the lower the particle p_T the more it spirals while passing through the detector.

[2]A cluster in the TPC is defined as the charge induced on a pad-row of the detector by a traversing particle that, in a search window of 5 pads in wire direction and 5 bins in time direction, exceeds a certain threshold and fulfills all necessary quality criteria. The number of findable clusters is the number of geometrically possible clusters which can be assigned to a track.

3.4.3 Particle identification

In this work, Particle identification (PID) of the K^{*0} daughters is carried out with two different strategies in parallel: TOF PID and TPC PID. In both of them, the main objective is to identify correctly the pair and to remove as much background as possible.

The TOF PID analysis is based on the measurement of the time of flight of the particles passing through the detector, while the TPC relies on their specific energy loss. In both cases, the "nσ-cut" method is employed [52]. Let i indicate the detector used for PID (i = TPC, TOF) and j the particle species hypothesis. This method is based on the definition of a discriminating variable $n_{i,j}^{\sigma_{PID}}$ as

$$n_{i,j}^{\sigma_{PID}} = \frac{X_j - X_{i,j}^{exp}}{\sigma^{PID}{}_{i,j}} \tag{3.6}$$

where X_j is a measured observable in the detector i (energy loss if i = TPC, time of flight if i = TOF), $X_{i,j}^{exp}$ is the prediction of that observable's value in the mass hypothesis j and $\sigma_{i,j}^{PID}$ is the resolution on the measurement. Particle identification is then performed by applying an appropriate cut on the discriminating variable. For the TPC analysis, the candidate π and K are identified with a 2σ cut on the TPC signal. For the TOF analysis, a 2σ cut has been applied on the TOF signal. On top of that, an additional 5σ cut on the TPC signal is applied in order to reduce the contribution of the mismatched tracks: a track identified within 2σ as a pion (kaon) by the TOF is rejected if it is not identified as a pion (kaon) by the TPC within 5σ. The contribution from mismatched tracks was particularly relevant for particles with transverse momentum up to 1 GeV/c in Pb-Pb; even though the mismatch probability is lower in p-Pb collisions, this cut is still helpful in reducing the background.

In Fig.3.5 the response of the TPC for the kaon and pion is plotted in terms of the $n_{TPC}^{\sigma_{PID}}$ as a function of the momentum reconstructed at its inner radius, p_{TPC}. Likewise, in Fig.3.6 the TOF response for the kaon and the pion is

given by $n_{TOF}^{\sigma_{PID}}$ as function of p. In table 3.1 the PID cuts are reported.

Because of the natural kinematics cutoff of low momentum particles ($p_T <$

PID strategy	Cut	p_T range
TPC 2σ	$\lvert n\sigma_{\pi,K}^{TPC}\rvert < 2.0$	full range
	$\lvert n\sigma_{\pi,K}^{TPC}\rvert < 5.0$	full range
TOF 2σ	$\lvert n\sigma_{\pi,K}^{TOF}\rvert < 2.0$	full range

Table 3.1: PID cuts.

0.3 GeV/c) that do not reach the TOF, K^{*0} with $p_T < 0.5$ GeV/c cannot be reconstructed with TOF PID. This issue and the mismatch can be overcome or at least be reduced using a TPC-TOF combined analysis.

3.4.4 Signal extraction

The candidate resonance invariant mass (M_{inv}) distribution is obtained from the combination of primary identified kaons and pions from the same events into unlike-sign pairs, as a function of the resonance transverse momentum. The distributions for $K^+\pi^-$ and $K^-\pi^+$ are obtained separately and then summed bin by bin to obtain the total signal for K^{*0} and $\overline{K^{*0}}$ respectively. In order to extract the K^{*0} signal it is necessary to remove as much as possible the contribution of the uncorrelated pairs to the background contribution. In this analysis the Like-Sign (LS) pair technique has been used to estimate and subtract the background: $K^+\pi^+$ and $K^-\pi^-$ pairs from the same event have been built separately and then combined into a geometric mean, according to the formula:

$$LS = 2\sqrt{y_{++}y_{--}}, \quad \delta LS = \sqrt{\frac{y_{++}^2(\delta y_{--})^2 + y_{--}^2(\delta y_{++})^2}{y_{++}y_{--}}} \tag{3.7}$$

where $y_{\pm\pm}$ and $\delta y_{\pm\pm}$ are the entries in each M_{inv} bin for the $K^+\pi^+$ and $K^-\pi^-$ distributions and their statistical errors, respectively. Since the unlike-sign and like-sign pairs are estimated from the same set of events, no normalization is needed before the background subtraction.

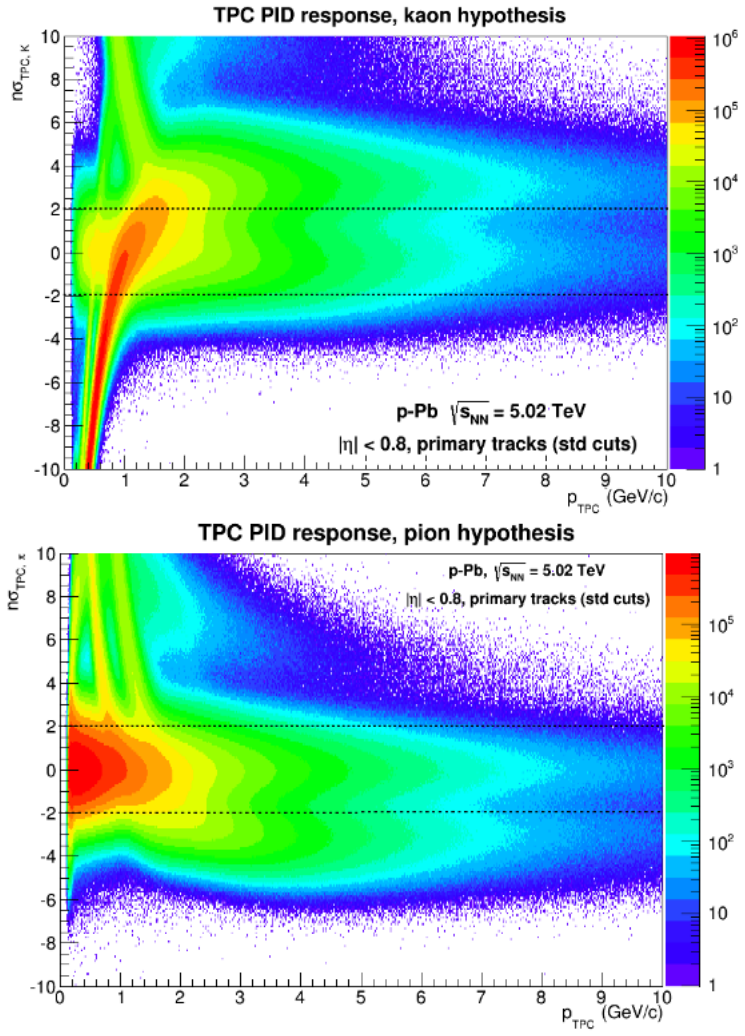

Figure 3.5: TPC response for kaon (top) and pion (bottom) hypothesis in terms of $n_{TPC}^{\sigma_{PID}}$ as function of the particle momentum at the inner radius of the TPC. The black dashed lines mark a 2σ selection.

Another technique that can be used for the subtraction of the combinatorial background is the event mixing (EM) technique. The background invariant mass distribution is built by combining uncorrelated unlike-sign charged identified kaons and pions from different events. When applying this method, it is important to combine pairs from events with similar topology and multiplicity, to reproduce satisfactorily the kinematic properties of the

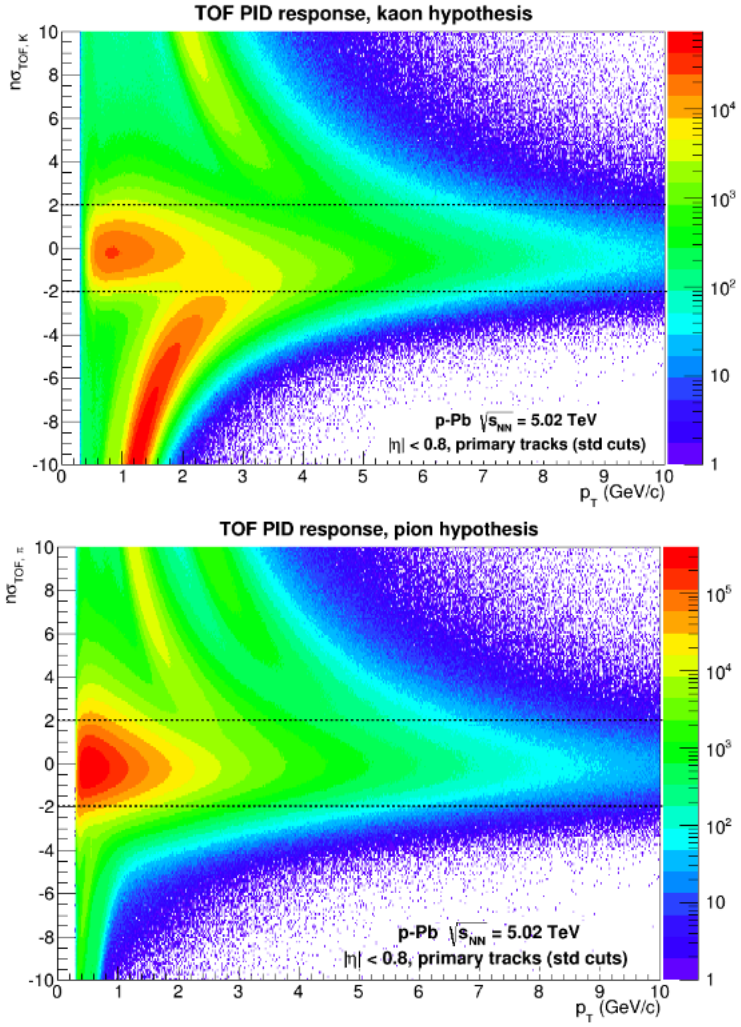

Figure 3.6: TOF response for kaon (top) and pion (bottom) hypothesis in terms of $n_{TOF}^{\sigma_{PID}}$ as function of the particle momentum at the vertex. The black dashed lines mark a 2σ selection.

combinatorial background. The total event mixing invariant mass distribution has to be normalized to the unlike-sign distribution before subtraction, because the statistics of the EM distribution is higher, depending on the number of mixed events used to evaluate the background. In this study, the event mixing technique is only used to check the results of the LS analysis. In Fig. 3.7 an example of unlike-sign, like-sign and normalized event mixing

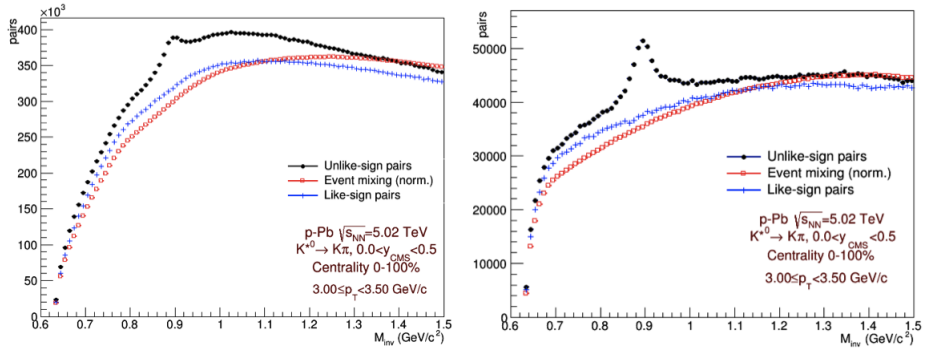

Figure 3.7: Distributions of unlike-sign pairs (black), like-sign background (blue) and normalised event mixing background (red) for the TPC (left) and TOF (right) analysis in the p_T bin 3.0 - 3.5 GeV/c. The event-mixing background is normalised in the 1.3-1.5 GeV/c^2 invariant mass range, while the like-sign background is not normalised.

distribution are shown for the TPC (left) and the TOF (right) in the p_T range 3.0 - 3.5 GeV/c.

3.4.5 Invariant mass fit

The invariant mass distribution after the like-sign background subtraction is fitted using the Roofit package [105]. The function used for fitting the resonance peak is [106]:

$$S(M_{K\pi}) = F(M_{K\pi}) \times P(M_{K\pi}) \tag{3.8}$$

where $F(M_{K\pi})$ is the non-relativistic Breit-Wigner

$$F(M_{K\pi}) = \frac{\Gamma/2}{(M_{K\pi} - M_0)^2 + \frac{\Gamma^2}{4}} \tag{3.9}$$

with M_0 and Γ being the vacuum K^{*0} mass and width respectively.
$P(M_{K\pi})$ is the Boltzmann factor phase space that takes into account the K^{*0}

produced through kaon and pion scattering ($K + \pi \rightarrow K^{*0} \rightarrow K + \pi$):

$$P(M_{K\pi}) = \frac{M_{K\pi}}{\sqrt{M_{K\pi}^2 + p_T^2}} \times \exp\left(-\frac{\sqrt{M_{K\pi}^2 + p_T^2}}{T_{f_0}}\right) \tag{3.10}$$

where T_{f_0} is the temperature at which the resonance is emitted, fixed at about 250 MeV like in the K^{*0} analysis in pp.
For the background fit, a second degree polynomial has been used in almost the totality of the p_T bins. From Fig. 3.7 it can be seen that the TPC and TOF backgrounds have different shapes before subtraction. After the subtraction, the residual background of the TPC analysis maintains a curved shape while the TOF residual background is flatter. Due to this difference and after a series of trials with different function for the background (see chapter 4 for details), the second degree polynomial is deemed the one that gives the most satisfactory description of the background shape in both analyses.

The experimental points are thus fitted with a sum of these terms and

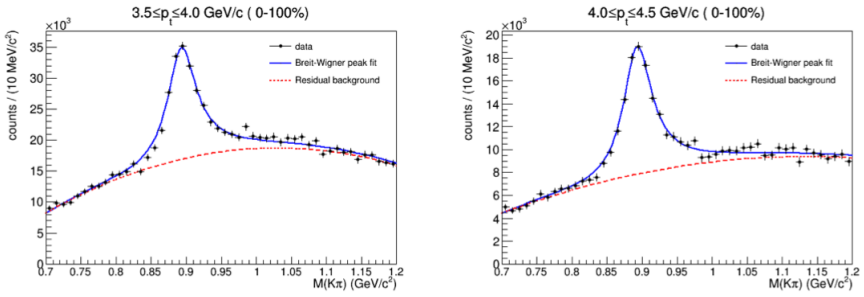

Figure 3.8: Examples of the fit on the LS background-subtracted invariant mass distribution (black points) for the TPC 2σ analysis. The resonance peak is fitted with a non-relativistic Breit-Wigner for the signal (solid line) and a second degree polynomial (dashed line) to shape the residual background. The Breit-Wigner width is fixed to the PDG value, and the width of each bin is 10 MeV/c^2.

the final fitting function is given by $F(M_{K\pi}) \times P(M_{K\pi}) + B(M_{K\pi})$. A few examples of fitted like-sign background subtracted signals for the TPC and TOF analyses are shown in Fig. 3.8 and 3.9 respectively. During the fitting procedures, the width of the resonance is fixed at the PDG value, $\Gamma_{K^{*0}} =$

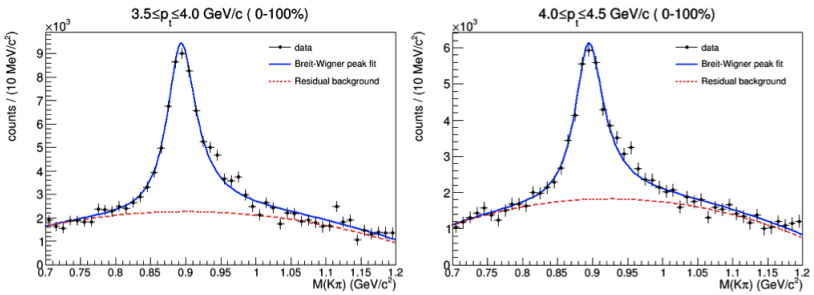

Figure 3.9: Examples of the fit on the LS background-subtracted invariant mass distribution (black points) for the TOF 2σ analysis. The resonance peak is fitted with a non-relativistic Breit-Wigner for the signal (solid line) and a second degree polynomial (dashed line) to shape the residual background. The Breit-Wigner width is fixed to the PDG value, and the width of each bin is 10 MeV/c^2.

0.0478 GeV/c^2 [63], while its mass is left free to vary. The mass constraint has been studied for systematic uncertainties but no significant effects have been found.

The invariant mass fit for all the p_T bins for both analyses can be found in appendix A.

The analysis was repeated using the EM technique as a cross check on the background estimation. The event mixing technique combines uncorrelated unlike-sign charged identified kaons and pions from different events. the pairs are chosen among events with similar topology and multiplicity, to reproduce satisfactorily the kinematics properties of the combinatorial background. Ten events are considered at a time for the mixing. Like for the unlike-sign distribution, the contribution from $K^+\pi^-$ and $K^-\pi^+$ are obtained separately and then summed. The resulting distribution is normalized to the unlike-sign distribution in the range $1.3 \leq M_{inv} \leq 1.5$ GeV/c^2. A non-relativistic Breit-Wigner has been used for fitting the signal and a second degree polynomial for the EM background fit.

The fit and the raw yields from the analysis with the event mixing background are shown in respectively in Fig. 3.10 and Fig. 3.11.

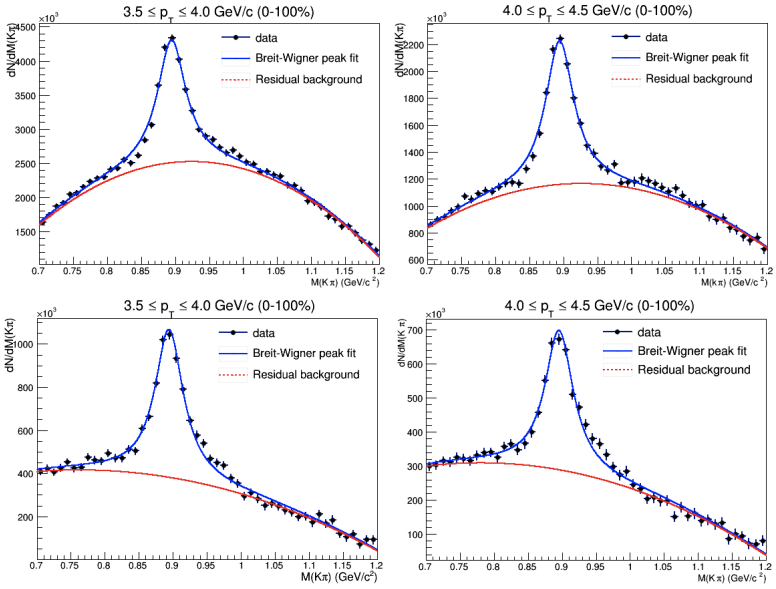

Figure 3.10: Examples of the fit on the EM background-subtracted invariant mass distribution (black points) for the TPC 2σ analysis (upper row) and TOF 2σ analysis (bottom row). The resonance peak is fitted with a non-relativistic Breit-Wigner for the signal (solid line) and a second degree polynomial (dashed line) to shape the residual background. The Breit-Wigner width is fixed to the PDG value, and the width of each bin is 10 MeV/c^2.

3.5 Efficiency correction

The efficiency corrections have been estimated from simulated p-Pb events on which the same selection criteria as the data have been applied. The Monte Carlo event and track simulation is obtained with DPMJET [94] and a full Geant [95] simulation and reconstruction and anchored[3] to the data sets used in this analysis, weighted to the number of events per run (typically, a MC run contains 25% of the statistic of the corresponding run in the data).
In the analysis with the TPC the total efficiency correction factor is obtained from two contributions:

$$\epsilon^{TPC}_{K^{*0},tot} = (Acc \times \epsilon_{rec})(p_T) \times \epsilon^{TPC}_{PID} \tag{3.11}$$

[3]With "anchoring" is indicated a procedure used to correctly take into account the data taking conditions (dead channels, data taking setup, etc.) in the simulated events.

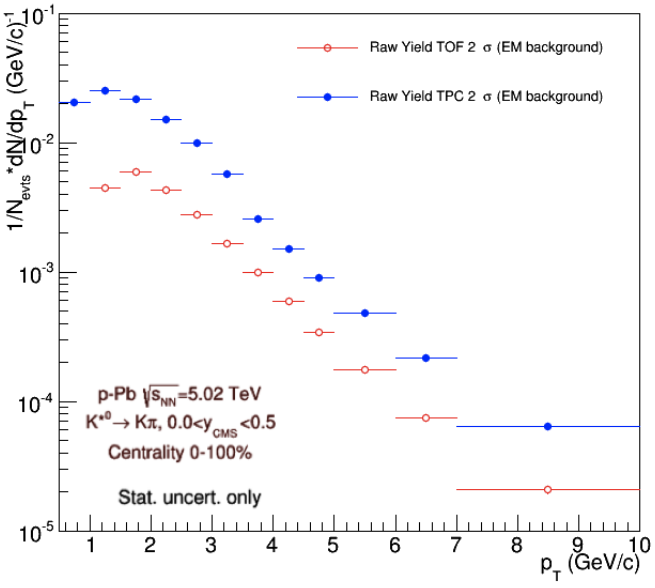

Figure 3.11: Raw yields from the analysis with the event mixing background from TPC (blue) and TOF (red).

where $(Acc \times \epsilon_{rec})(p_T)$ is the p_T-dependent correction due to the detector acceptance (Acc) and reconstruction efficiency (ϵ_{rec}), including the contribution of the tracking and candidate selection cuts. It is defined as the ratio between the number of reconstructed (with quality cuts) and generated K^{*0} which decay into charged $K\pi$ pairs in the interval $0.0 < y_{CM} < 0.5$. ϵ_{PID}^{TPC} is the PID efficiency of the 2σ-cut on the TPC signal. The TPC response is gaussian thus its PID efficiency is given by an *a priori* factor which is the product of two single-track efficiency terms, if one considers the identification of each candidate daughter as independent. The gaussian factor for a 2σ-cut is 0.9545 for a single track, therefore $\epsilon_{PID}^{TPC} = f^2 = (0.9545)^2 = 0.911$. The total efficiency correction for the TPC analysis, shown in Fig. 3.12, is obtained as the $(Acc \times \epsilon_{rec})(p_T)$ term obtained from MC (black solid line), scaled by the p_T-independent gaussian factor for a 2σ-cut (blue solid line).

The total efficiency for the TOF analysis is the product of three contribu-

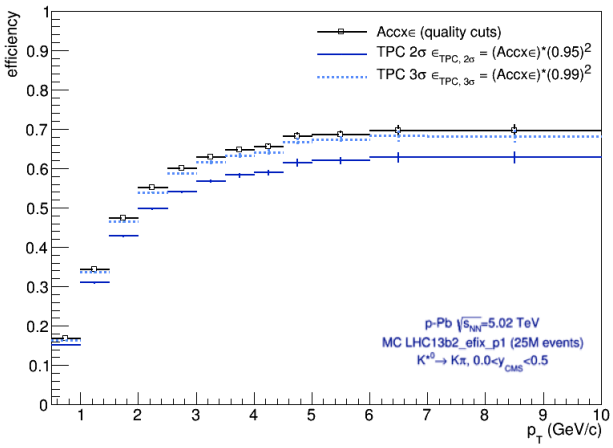

Figure 3.12: Efficiency correction for the TPC analysis. The efficiency per acceptance term ($Acc \times \epsilon_{rec}$) after the quality cuts selection is shown in black, while the total efficiency that includes also the gaussian TPC PID efficiency for a 2σ cut is shown in blue. The light-blue dashed line represents the efficiency including the correction for a 3σ-cut, for comparison.

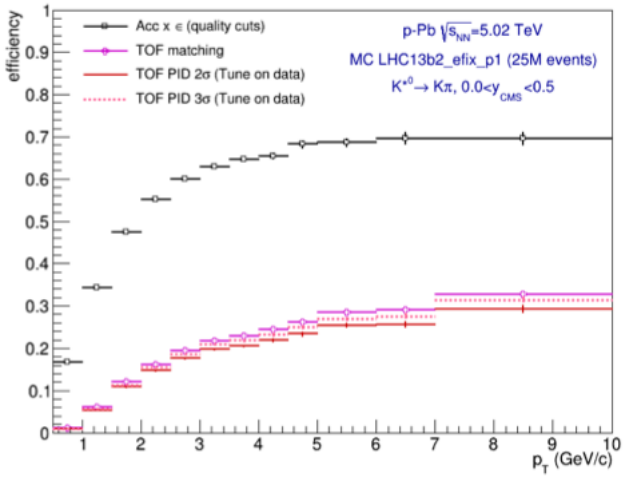

Figure 3.13: Efficiency correction for the TOF analysis from MC response. The efficiency per acceptance term ($Acc \times \epsilon_{rec}$) after the quality cuts selection is reported in black, the K^{*0} TOF matching efficiency in magenta and the total efficiency in red, including a 2σ cut on TOF PID. The pink dashed line represents the total efficiency when a 3σ-cut on TOF PID is applied, for comparison.

tion:

$$\epsilon^{TOF}_{K^{*0},tot} = (Acc \times \epsilon_{rec})(p_T) \times \epsilon^{match}_{K^{*0}} \times \epsilon^{TOF}_{PID} = \epsilon'^{match}_{K^{*0}} \times \epsilon^{TOF}_{PID} \tag{3.12}$$

where $(Acc \times \epsilon_{rec})(p_T)$ is the p_T-dependent correction due to the detector acceptance (Acc), reconstruction efficiency (ϵ_{rec}) and selection cuts, that is common with the TPC analysis. The TOF matching efficiency, $\epsilon^{match}_{K^{*0}}$, is the product of the single-track matching efficiency of each daughter, convoluted with the two-tracks acceptance. The ϵ^{TOF}_{PID} factor, found to be constant, accounts for the TOF PID of the daughters performed with the nσ-cut strategy.

The TOF PID response is not perfectly gaussian and it is not possible to obtain the PID efficiency a priori like in the TPC case. The TOF PID efficiency has to be estimated from the MC considering that the PID response is affected by residual non-gaussian tail in the TOF signal.

The TOF matching contribution on the K^{*0} efficiency was also estimated from a Monte Carlo sample. The K^{*0} matching efficiency ($\epsilon'^{match}_{K^{*0}}$) is defined as

$$\epsilon'^{match}_{K^{*0}} = \frac{R_{TOF}(0 < y_{CM} < 0.5)}{G(0 < y_{CM} < 0.5)} \tag{3.13}$$

where the numerator $R_{TOF}(0 < y_{CM} < 0.5)$ is the number of generated K^{*0} and $\overline{K^{*0}}$ whose decay products have been reconstructed in the TOF in the $0 < y_{CM} < 0.5$ range. The denominator, G, is the number of generated K^{*0} and $\overline{K^{*0}}$ which decay into charged Kπ pairs in the $0 < y_{CM} < 0.5$ range.

The TOF total PID efficiency, $\epsilon'^{TOF}_{K^{*0},tot}$, has, at numerator, the number of resonances that have been reconstructed, matched and identified by TOF. These are identified as K^{*0} or $\overline{K^{*0}}$ by using the Monte Carlo information of their PDG code. The denominator is the same as for the TOF matching efficiency (G).

As for the TPC analysis, the reconstructed tracks are selected through the same cuts used for the data.

Figure 3.13 shows the total efficiency for the TOF analysis.

The raw yields obtained from the fit of the invariant mass distribution in the p_T bins are normalized for the total number of events. After applying the above mentioned efficiency correction, the yields are divided by the branching ratio of the considered decay channel ($K^{*0} \to K\pi$, 66.6%).
The corrected yields are obtained as

$$\frac{d^2N_{K^{*0}}}{dydp_T} = \frac{1}{2}\frac{1}{N_{ev}}\frac{1}{\Delta y \Delta p_T}\frac{N_{K^{*0}(p_T)}}{\epsilon(p_T)\cdot B.R.} \tag{3.14}$$

where N_{ev} is the number of total events, $\epsilon(p_T)$ is the total efficiency correction, different for the TOF and TPC, and $B.R.$ the branching ratio. The factor 1/2 takes into account that the measurement of the yields is performed for both particles and antiparticles. The factor $\Delta y = 0.5$ corrects for the rapidity since the analysis is carried out only in half of the rapidity range.
In Fig. 3.14 the corrected yields for the TPC (left) and TOF (right) analyses are shown, with statistical errors only.

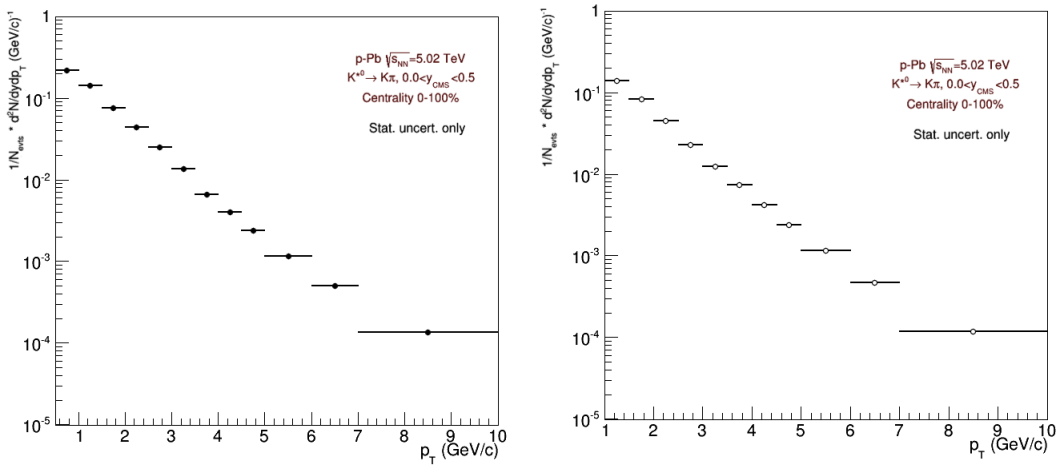

Figure 3.14: Corrected (K^{*0} + $\overline{K^{*0}}$)/2 spectra obtained with the TPC analysis (left) and TOF analysis (right).

Chapter 4

Systematic uncertainties

The K^{*0} yields have been checked for systematic effects originated from each of the analysis steps: track selection, particle identification, background estimation, fitting procedure.
In order to estimate the systematic error associated with each contribution, the analysis has been repeated by varying one setting at the time. For each of the steps, at least one alternative selection/procedure with respect to the main analysis has been considered.
Following the method described in [107], all the systematic uncertainties have been computed as the Root Mean Square (RMS) of the measurements set in order to obtain a more reliable estimation. The RMS is defined as

$$\sigma_x = \sqrt{\frac{1}{N}\sum_{i=1}^{N}(x_i - \overline{x})^2}, \tag{4.1}$$

where x_i is the measurement, N is the number of measurements in the sample and $\overline{x}$ is their mean value.
In addition, it has been verified that the measurements x_i, used for the systematic checks, are not statistically compatible with the default measurement. The main analysis will be from now indicated as "default measurement", summarized below:

- TPC (TOF) PID with a 2σ-cut (2σ-cut);

- like-sign distribution used for the background estimation;
- a non-relativistic Breit-Wigner has been used for the resonance peak fit, a second degree polynomial for the residual background fit;
- the resonance width is fixed at the PDG value;
- the resonance mass is left free to vary within the fit range.

Indicating the measurements and their statistical uncertainties as ($y_i \pm \sigma_i$), the value closest to the weighted mean of the sample has been chosen as the "central value", together with its statistical uncertainties ($y_c \pm \sigma_c$). The statistical compatibility check verifies whether the differences $(\Delta y)_i$ = y_c - y_i are due to statistics rather than to a systematic effect. The variable

Source	**Syst. uncert. TPC analysis** (%) of central value	**Syst. uncert. TOF analysis** (%) of central value
Yield extraction		
Residual bg. fit function (0-100%))	3÷5	3÷4
Constraint on BW mass	n.s.	n.s.
Constraint on BW width and fit range	8	10
Background estimation		
Event-mixing background (0-100%)	n.s.	n.s.
LS background normalisation	n.s.	n.s.
Tracking and track selection		
Global tracking	8	8
Material budget	6	6
TOF matching	-	4
PID selection	5	7
Tune of the TOF PID response	-	4

Table 4.1: Contribution to the systematic uncertainty on the yield from various sources, expressed in percentile of the measured yield (central value). "n.s." indicates no significant contribution to the total systematic uncertainty.

$\Delta_i = \sqrt{\sigma_i^2 - \sigma_c^2}$ has been defined as the difference in quadrature of the statistical errors associated to each of the measurements. The ratio $n_i = (\Delta y)_i/\Delta_i$ indicates how much of the difference is due to statistics. For $n_i \leq 1.0$ there is no systematic effect, the measurements and the "central value" are compatible within the statistical uncertainties [107]. The measurements considered in the default analysis differ from the "central values" because they have been selected on order to have optimized settings.

In Table 4.1 all the systematic uncertainties are summarized while a more extensive description will be given in the following section.

4.1 Tracking and material budget systematic uncertainties

In the recently published analysis on p-Pb collisions [108], the systematic uncertainty related to the global tracking efficiency and the track selection is estimated to be 4% for both the pion and the kaon separately. Since for the reconstruction of the K^{*0} resonance two tracks are used, this factor has to be doubled. Then, a 8% systematic uncertainty is assumed for the K^{*0} in both the TPC and TOF analyses.

Another possible source of systematic uncertainty is, for the TOF analysis

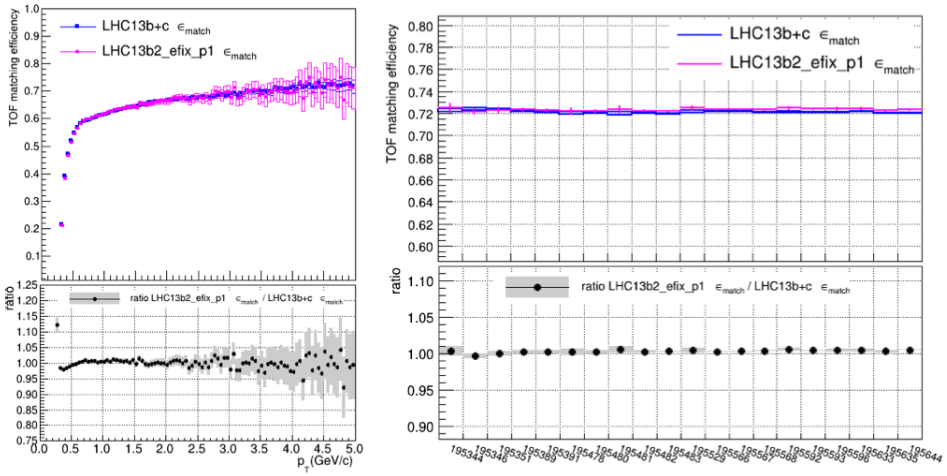

Figure 4.1: Left: single-track TOF matching efficiency as a function of p_T in MC and data and their ratio for a sample run (about 12×10^6 events). Right: comparison of the average single-track TOF matching efficiency for $p_T > 1$ GeV/c for MC and data, for each of the good runs in the considered dataset.

only, the TOF matching efficiency, see section 3.3. The discrepancy between the TOF matching efficiency in data and in the MC accounts for a 2% systematic uncertainty for a single track, doubling to 4% for this analysis.

The material supporting the detectors and their misalignment constitute the "dead zones" in which the detector is not sensible to the particles passage. Systematic uncertainties given by the inert (as opposed to sensible) material present along the particle path have also to be considered. This is the material budget contribution, common for the TOF and TPC analyses, that is estimated to be 3% for 0.2 GeV/c pions/kaons (single track) and negligible above 3 GeV/c for both species. An additional systematics effect, again for the TOF analysis only, is introduced by the uncertainty on the material crossed by the particles in the TRD detector and by imperfections in the simulation of the hadronic interactions in the above mentioned material. This additional contribution has been estimated to be a total of 6%.

4.2 PID systematic uncertainty

The systematic uncertainty associated with PID is different for the TPC and the TOF analyses. The analysis is repeated by widening the PID cut to 2.5σ-cut in both cases. The requests on the track quality and the primary selection cuts are kept the same, as well as the background extraction, fit function, fit parameters and range. The corrected yields for the TPC and TOF analyses are shown in Fig. 4.2 and 4.3 (statistical error only). The ratio between the 2.5σ-cut and the 2σ-cut analysis are shown in Fig. 4.4 and Fig. 4.5 for the TPC and TOF respectively.

For the TPC analysis the ratio is very close to unity and with small deviations as a function of p_T. On the other hand, the ratio for the TOF analysis shows a systematic trend in the region from low to intermediate p_T. The systematic uncertainty is attributed bin by bin and is 5% in average for the TPC and 7% for the TOF.

For the TOF case only, an additional systematic uncertainty related to the non-gaussianity of the TOF PID response has also been considered. The TOF signal has been parametrised in the Monte Carlo as a gaussian plus an asymmetric exponential tail (Fig. 4.6) in order to reproduce the data. The tail parameter τ defines the percentage of the full response width at which

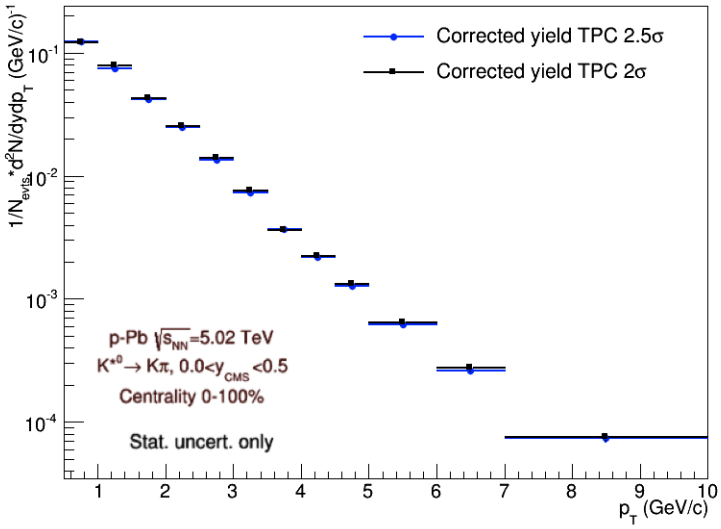

Figure 4.2: Corrected yields for the 2σ-cut (black line) and the 2.5σ-cut (blue line) analysis for the TPC analysis.

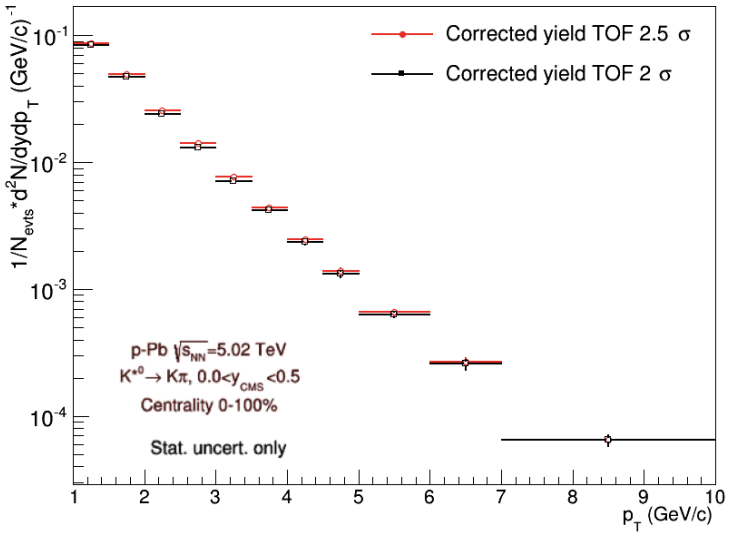

Figure 4.3: Corrected yields for the 2σ-cut (black line) and the 2.5σ-cut (red line) analysis for the TOF analysis.

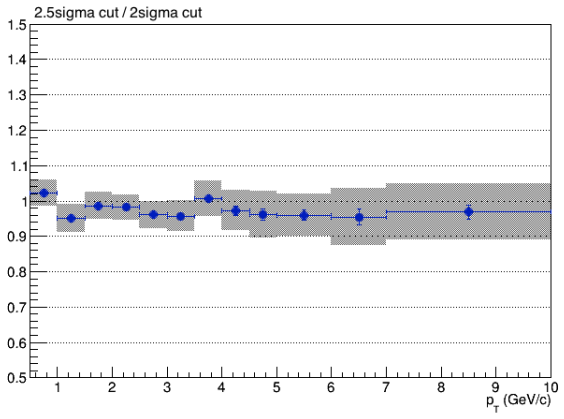

Figure 4.4: Ratio of corrected yields for the 2σ-cut and the 2.5σ-cut analysis for the TPC analysis. The blue bars are computed from the yields errors subtracted in quadrature while the shaded boxes are the yields errors summed in quadrature.

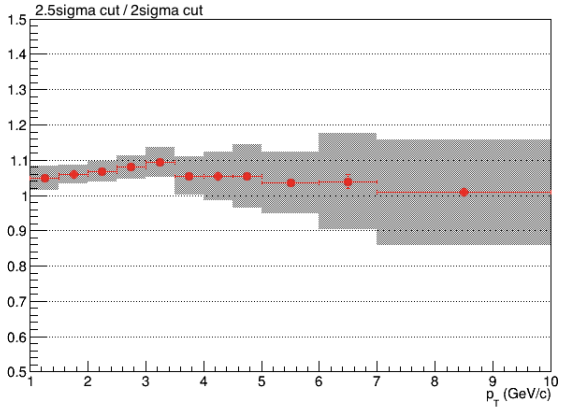

Figure 4.5: Ratio of corrected yields for the 2σ-cut and the 2.5σ-cut analysis for the TOF analysis. The blue bars are computed from the yields errors subtracted in quadrature while the shaded boxes are the yields errors summed in quadrature.

the exponential behaviour starts. In order to evaluate the systematic effect on the TOF PID efficiency due to this choice, the tail parameter has been varied between 0.8σ and 1.0σ from the point at which the tail joins the gaussian distribution. The integral of the resulting distribution in a Nσ range corresponds to the efficiency of the Nσ-cut TOF PID (for a single-track).

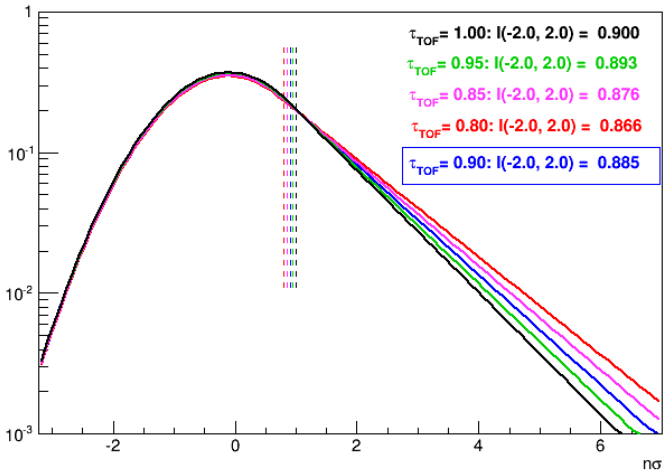

Figure 4.6: Function used to parametrise the TOF PID response in MC. The response is described a as a gaussian with an exponential tail, starting at τ_{TOF} (dashed lines), in units of multiples of the TOF resolution. Different colors correspond to different values of τ_{TOF}.

The PID efficiency varies by 2% for a single track and, considering two independent tracks, this propagates as a 4% systematic effect to the TOF PID yields measurement.

4.3 Systematic uncertainty related to the background estimation

The like-sign background used in this analysis is not normalized to the unlike-sign pair distribution. The spectrum obtained from a normalized like-sign background is compatible within the statistical errors with the one with no normalization. Thus, no systematic uncertainty is associated with the background normalization.
The signal after the like-sign and the event mixing background subtraction have been analyzed in order to check the procedure but no systematic uncertainties has been derived from the comparison. The comparison shows that

the two strategies for background subtraction lead to compatible results.

4.4 Systematic uncertainties from yields extraction

The systematic uncertainties on the extracted yields can be estimated varying the invariant mass fit settings. The fitting range, the fitting function and the constraints on the resonance parameters have been varied to identify the systematic effects.

4.4.1 Fit function systematic

Particular attention was given to the study of the background estimation, especially because of the peculiarity of the TPC residual background distribution as a function of p_T. At low-intermediate p_T (from 0.5 to 3.5 GeV/c), the TPC background is high and shows different slopes within the invariant mass range considered. Each p_T bin has been studied individually in order to pinpoint the best combination of settings for a optimal yield extraction. At high p_T, the TPC residual background very much resembles the TOF residual background that is low and has a flatter shape (see appendix A) over all the p_T intervals considered.

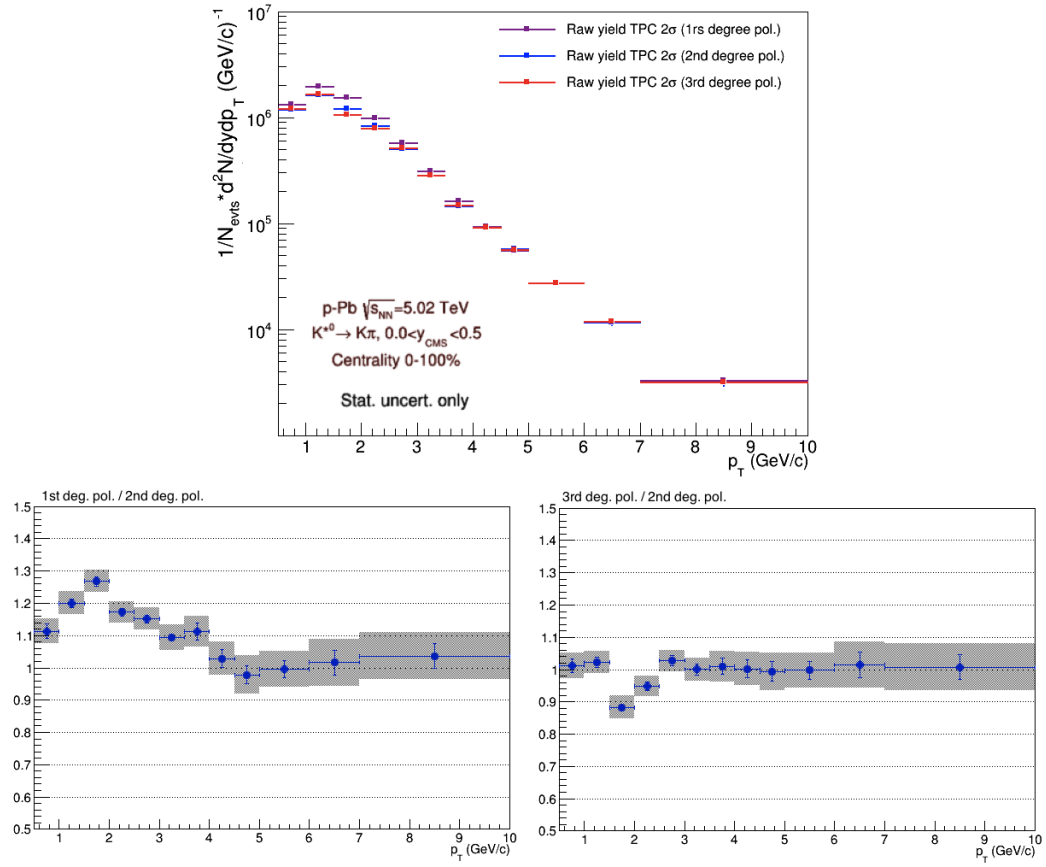

Figure 4.7: Top: raw yields from the TPC analysis. The fit of the resonance invariant mass distribution (LS-background) is performed using a first (violet line), second (blue), third (red) degree polynomial function for the fit of the residual background. Bottom: ratio of the raw yields with the first to second degree polynomial function for the residual background (left); ratio of the raw yields with the third to second degree polynomial function for the residual background (right). The bars represent the statistical errors subtracted in quadrature. The shaded grey boxes represent the statistical errors summed in quadrature.

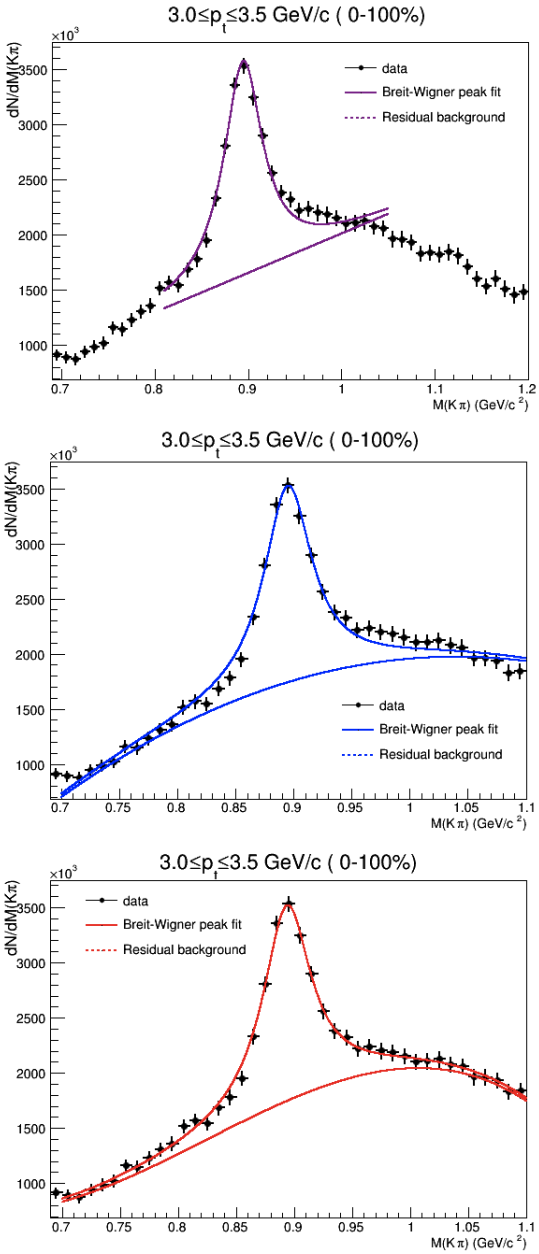

Figure 4.8: Examples of the fit on the LS background-subtracted invariant mass distribution for the TPC 2σ analysis with the three function used for the residual background fit. The resonance peak is fitted with a non-relativistic Breit-Wigner for the signal. To shape the residual background, a first (top, violet line), a second (centre, blue line) and third (bottom, red line) degree polynomial have been studied for the systematic uncertainties. The fits present different range for the chosen p_T because they are the optimized ones.

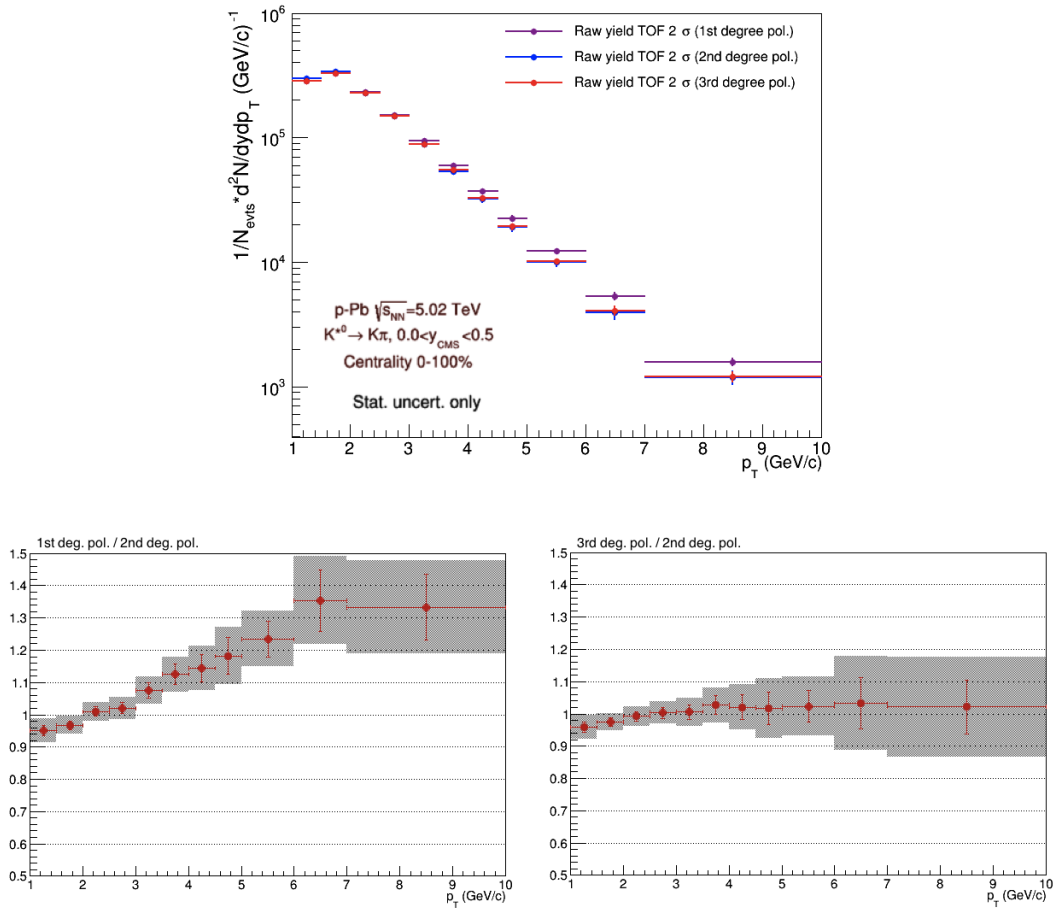

Figure 4.9: Top: raw yields from the TOF analysis. The fit of the resonance invariant mass distribution (LS-background) is performed using a first (violet line), second (blue), third (red) degree polynomial function for the fit of the residual background. Bottom: ratio of the raw yields with the first to second degree polynomial function for the residual background (left); ratio of the raw yields with the third to second degree polynomial function for the residual background (right). The bars represent the statistical errors subtracted in quadrature. The shaded grey boxes represent the statistical errors summed in quadrature.

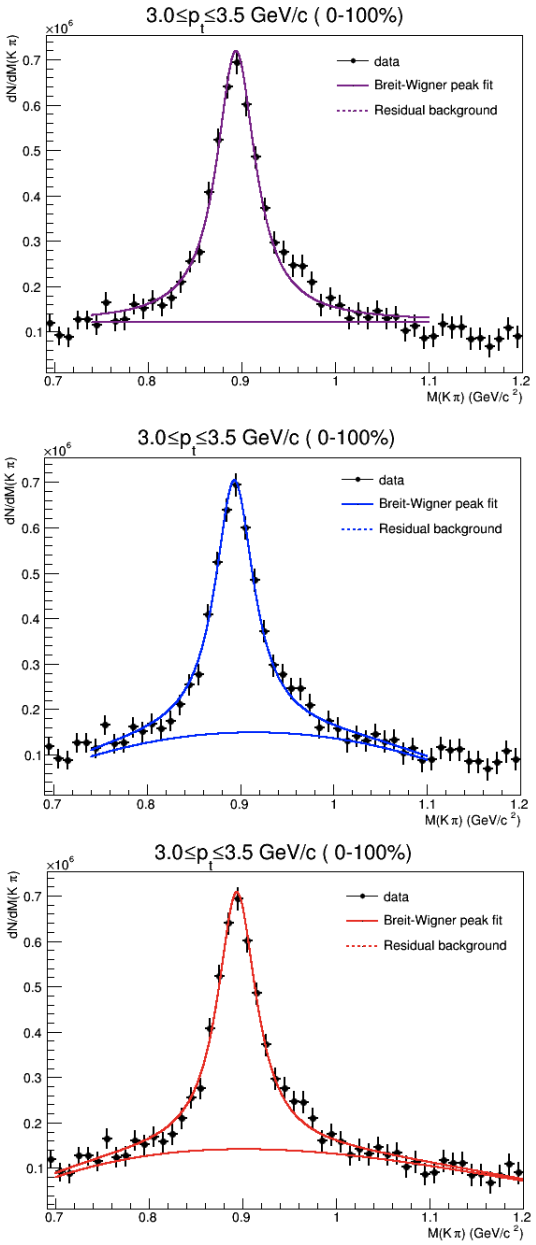

Figure 4.10: Examples of the fit on the LS background-subtracted invariant mass distribution for the TOF 2σ analysis with the three function used for the residual background fit. The resonance peak is fitted with a non-relativistic Breit-Wigner for the signal. To shape the residual background, a first (top, violet line), a second (centre, blue line) and third (bottom, red line) degree polynomial have been studied for the systematic uncertainties. The fits present different range for the chosen p_T because they are the optimized ones.

After the like-sign background subtraction, the residual background has been fitted with a second degree polynomial which best describes the behaviour of the data points. To check for the presence of systematics effects, the fitting procedure has been repeated using a linear and third degree polynomial functions. The fit ranges have been kept the same as the main analysis (optimized ones). When this was not possible, the smaller range variation has been used. A univocal choice could not be made for both TPC and TOF analysis due to the differences in their background shapes. This study has showed that the first degree polynomial is better suited to describe the flatter TOF background (but the second degree still remains the best solution) while it cannot reproduce the curved TPC background. The third degree polynomial is a valid solution for the TPC background analysis and still well describes the TOF background.
The raw yields for the three fit functions and their ratio are shown in Fig. 4.7 for the TPC and Fig. 4.9 for the TOF.
In Fig. 4.7, the raw yield from the residual background fit with the linear function shows a clear deviation al low p_T. This deviation is even more evident in the ratio with the second degree polynomial function. As it can be seen from Fig. 4.8, this is due to the unsuitability of the linear function for the TPC residual background, that has therefore been excluded from the systematic uncertainties estimation. The ratio of the raw yields with the third to second degree polynomial function for the residual background also shows a deviation in the p_T range $1.5 \leq p_T \leq 3.0$ GeV/c. As it can be seen from the fits in appendix A, this effects is to be imputed to the irregular shape of the TPC residual background for these p_T bins.
A similar effect can be seen in the TOF raw yield from the residual background fit with the linear function at high p_T and in the ratio of the raw yields from the linear fit function over the second degree polynomial function. Thus, also for the TOF case, the first degree polynomial function has been excluded from the systematic uncertainties estimation.
The systematic uncertainty contribution from the choice of fit the function, shown in Fig 4.11, varies between 3(3)% and 5(4)% as a function of p_T for the TPC (TOF).

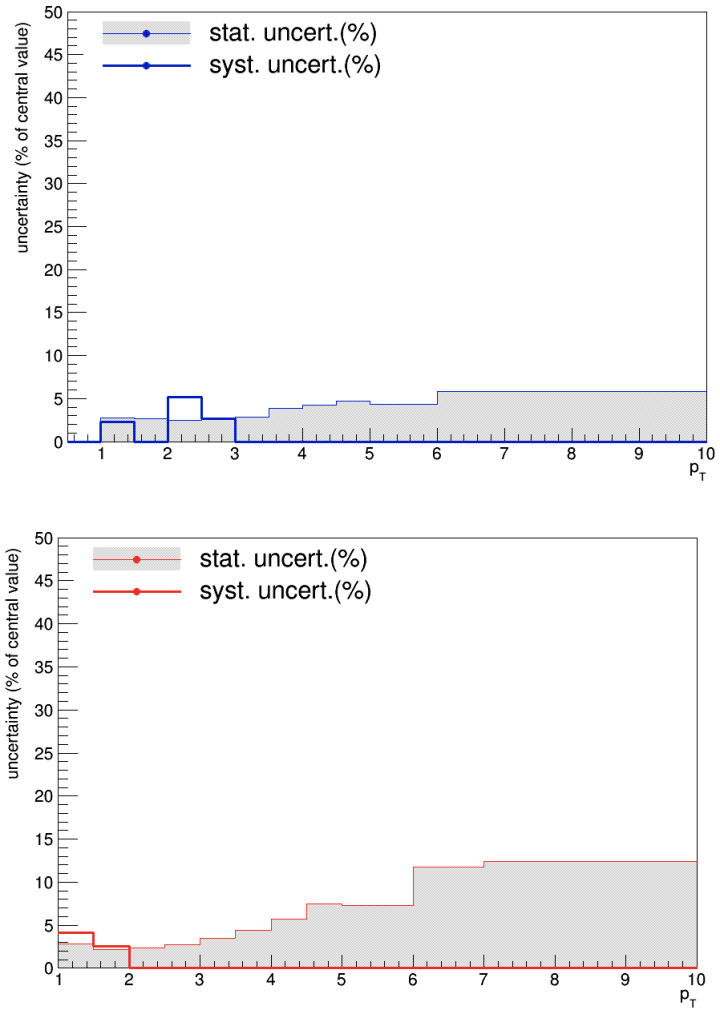

Figure 4.11: Comparison between statistical (shaded area) and systematic (bold line) uncertainty from the background fit function choice for the TPC (left, in blue) and TOF (right, in red).

4.4.2 Constraints on the resonance parameters

The Breit-Wigner fit parameters, the resonance mass and width, have been studied to look for systematic effects related to their constraint values. A

check was performed for both analyses by comparing the raw yields obtained from the fit in which the resonance mass is left free within the fit range (like in the main analysis) or constrained between 0.5 and 1.5 times the PDG value. The resulting yields were statistically compatible, showing that the yield measurement is not sensitive to reasonable variations of the mass parameter.

4.4.3 Fit range and resonance width

The systematic contribution from the fit range and resonance width have been considered together since they are dependent from each other: the variation of the fit range and/or of the width constraint introduces an uncertainty of the same nature, related to the fluctuation of the yields in the considered range.

The fit range has been optimized for each p_T bin by choosing a compromise between the lowest possible χ^2 and the "goodness" of the visual result of the fit. For the systematic studies, the default ranges have been extended or narrowed by 20 MeV/c^2. Three alternative ranges have been considered. At the same time, for each of the these three alternative ranges, the width has been fixed, like in the default analysis, or constrained between 0.5 and 1.5 times the PDG value. The choice of the fit range has been observed to be strongly p_T-dependent in the low to intermediate p_T region while it is less sensitive to changes at high p_T. This effect can be seen in Fig. 4.12, where the comparison between statistical and systematical errors is shown. In particular, in the interval from 1.5 to 5.0 GeV/c, the systematic error is significantly higher that the statistical one.
The systematic contribution associated with the fit range and width variation has been estimated (as the RMS) to be 8% for the TPC analysis and 10% for the TOF analysis.

Each of the systematic uncertainty contribution identified within the analysis have been summed in quadrature in order to obtain the total systematic

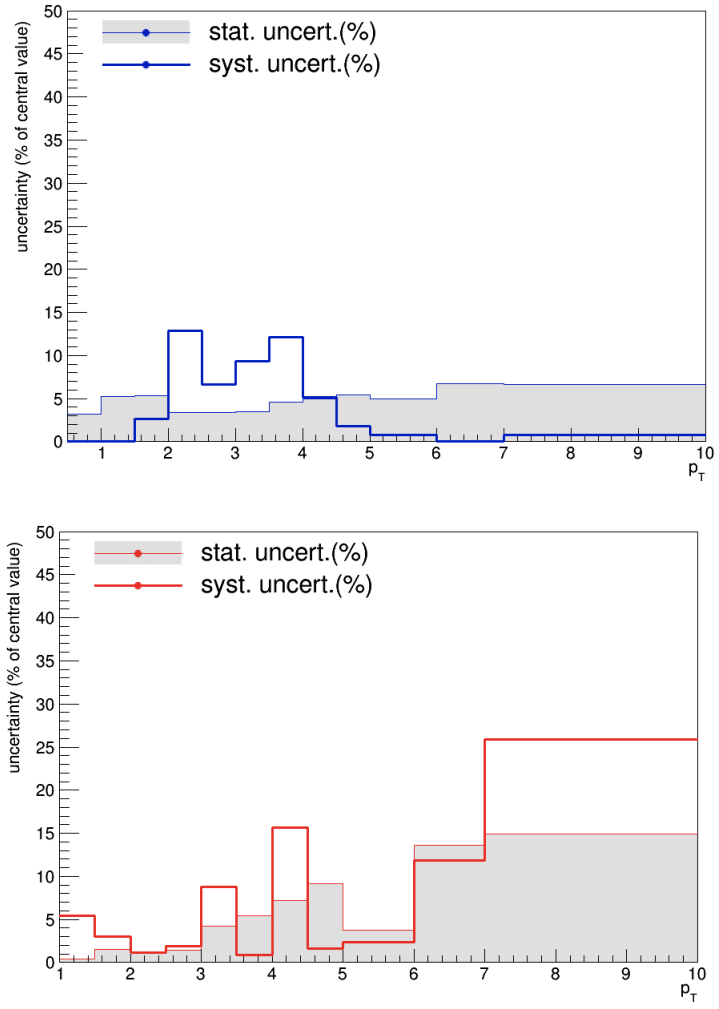

Figure 4.12: Comparison between statistical (shaded area) and systematic (bold line) error from the fit range choice for the TPC (left, in blue) and TOF (right, in red).

contribution related to the measurement. In Fig. 4.13 and Fig. 4.14, the total systematic uncertainty is shown together with the individual systematic uncertainty contributions. In Fig. 4.15 only the systematic uncertainties not in common to the TPC and TOF analyses are shown (global tracking and material budget contributions are excluded).

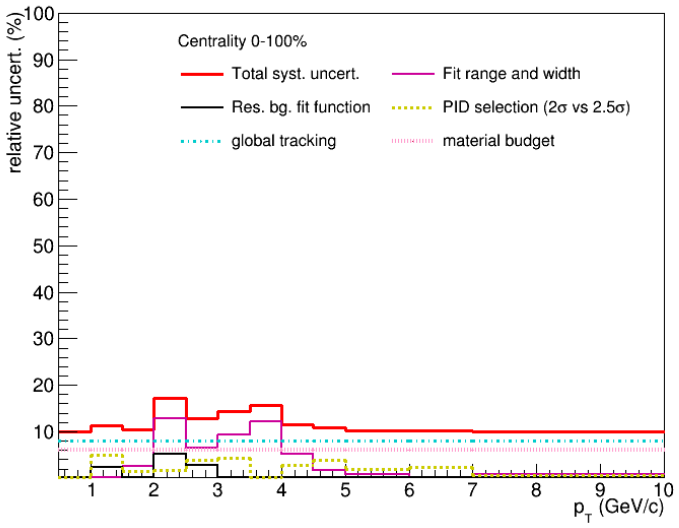

Figure 4.13: Total systematic uncertainty (red line) for the TPC analysis is shown together with the individual systematic uncertainty contribution.

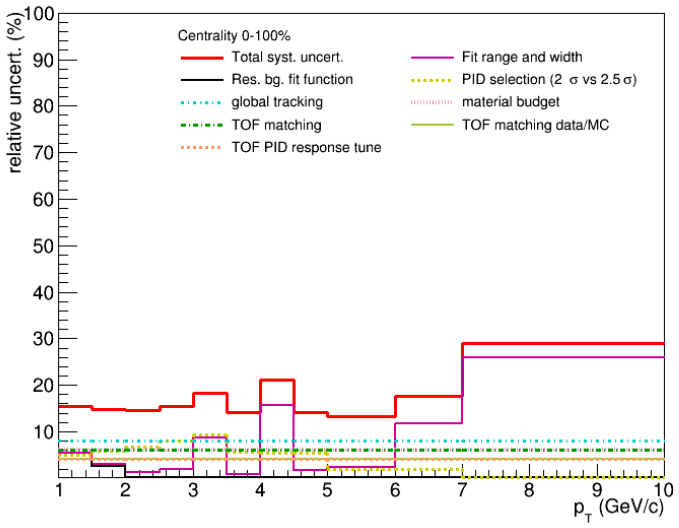

Figure 4.14: Total systematic uncertainty (red line) for the TOF analysis is shown together with the individual systematic uncertainty contribution.

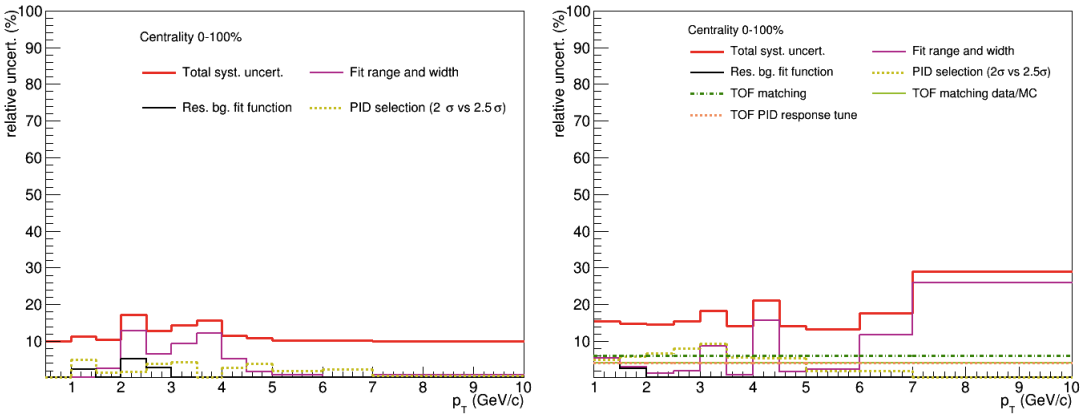

Figure 4.15: Total systematic uncertainty (red line) for the TPC (left) and TOF (right) analysis. Only the non common systematic uncertainty contribution are shown.

Chapter 5

K^{*0} yields and particle ratio

5.1 K^{*0} yields

Following the procedure described in section 3.5, the raw yields have been normalized and corrected for efficiency and branching ratio. The resulting measured spectra for K^{*0} is shown in Figure 5.1 for the TPC and TOF analyses. The statistical error are represented by the error bars while the systematic uncertainties (described in chapter 4) are represented by the boxes. The total systematic uncertainty for the TPC analysis is on average 12% while it is about 17% for the TOF analysis.

In order to extract the integrated yields, the distributions of Figure 5.1 have been fitted with a Lèvy-Tsallis function [109]. The Lèvy-Tsallis function is a power law, also used to fit the p_T spectra in pp and Pb-Pb collisions analyses, and given by:

$$\frac{1}{2\pi p_T}\frac{d^2N}{dydp_T} = \frac{dN}{dy}\frac{((n-1)(n-2))}{2\pi nT\cdot(nT+m(n-2))}(1+\frac{\sqrt{p_t^2+m^2}-m}{nT})^{-n} \quad (5.1)$$

where n, T and dN/dy are free parameters and m is fixed to the PDG K^{*0} mass value.

The K^{*0} yield fitted with the Lèvy-Tsallis function are shown in Fig. 5.2 for the TPC and TOF analyses.

Using the integrated yields value, the ratio of K^{*0}/K has been computed,

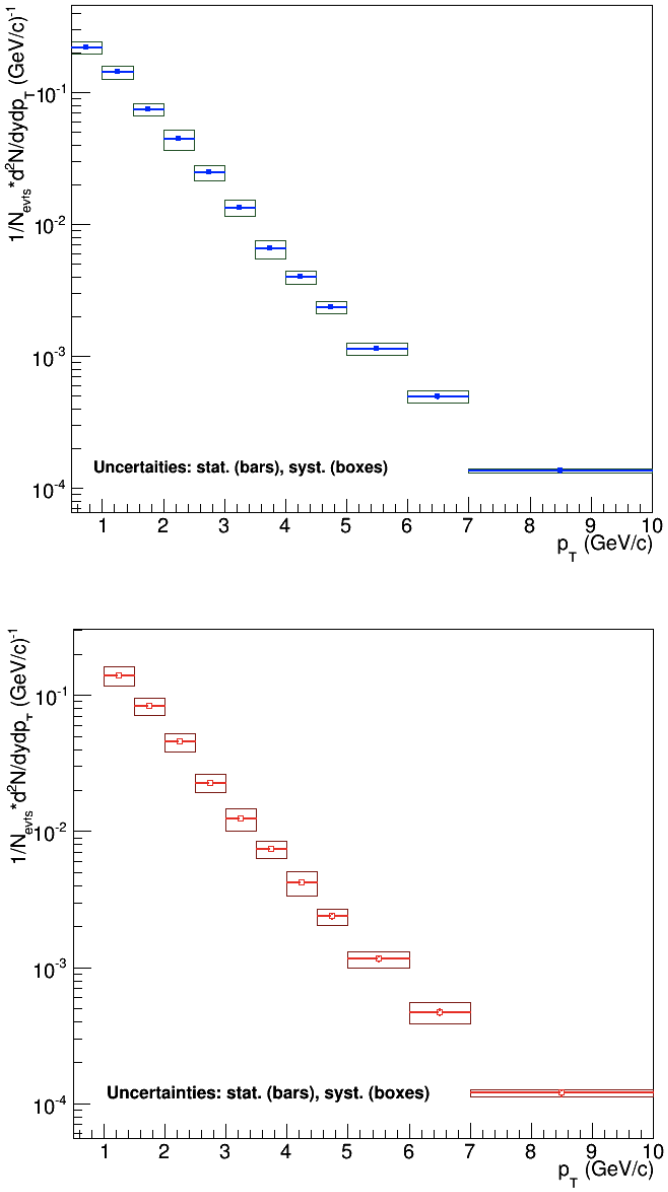

Figure 5.1: K^{*0} yield normalized by the total number of events and corrected for efficiency and branching ratio for the TPC (blue) and TOF (red) analyses. The statistical errors are represented by bars while the systematic uncertainties are represented by boxes.

as it will be discussed in the next section.

5.2 K^{*0}/K ratio

The K^{*0}/K ratio is studied in order to quantify the re-scattering the resonance undergoes during its life in the strongly interacting medium that forms after the proton and lead collisions.
From the integrated yield, obtained as illustrated in section 5.1, the ratio has been computed. The K yield have been taken from the identified particle spectra dedicated analysis [108]. In Table 5.1, the yield of both K^{*0} and K are reported. For K^{*0}, the integrated yields for the TOF and TPC analyses are shown separately.

The K^{*0}/K ratio as a function of the collision energy is shown in Fig. 5.3

	Detector	Centrality	$\frac{dN}{dy}$ $(GeV/c)^{-1}$
K^{*0}	TPC	0-100%	0.3315 ± 0.0300
	TOF	0-100%	0.3096 ± 0.0526
K		0-100%	1.1292 ± 0.0351

Table 5.1: K^{*0} integrated yields for the TPC and TOF analyses and K integrated yields as computed in [108]. The errors shown here are the overall errors, given by the statistical and systematic uncertainties summed in quadrature.

together with the results from pp and A-A collisions measured by ALICE [110] and STAR [111]. Both the TPC e TOF analyses results are displayed. It can be observed that the measurements of the ratio for p-Pb collisions lay in-between the results from pp and PbPb collisions analyses. This means that there may be rescattering effects in p-Pb collisions, even if these are less significant than in Pb-Pb collisions.

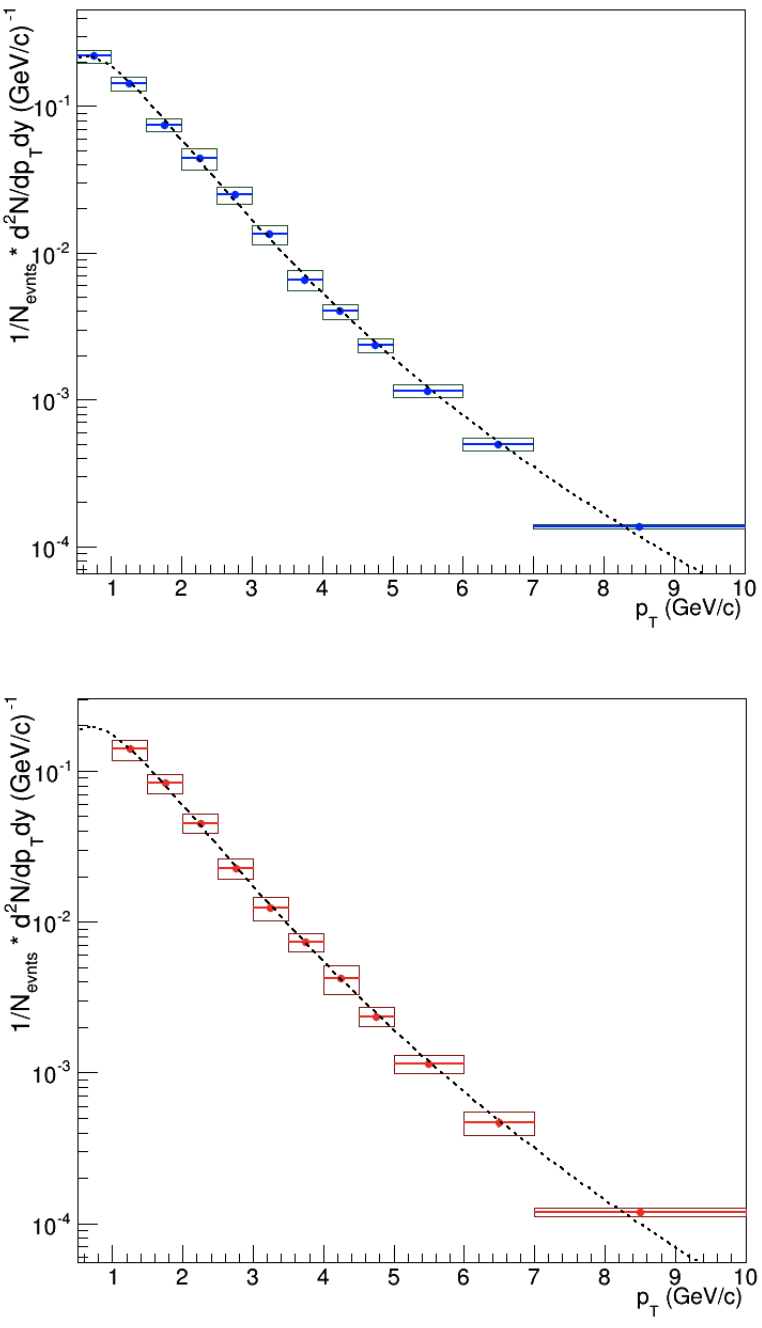

Figure 5.2: Corrected p_T spectra for K^{*0} from the TPC (blue) and TOF (red) analyses. The dashed line is the fit with the Lèvy-Tsallis function, Eq. 5.1. Error bars include statistical (bars) and systematic (boxes) uncertainties.

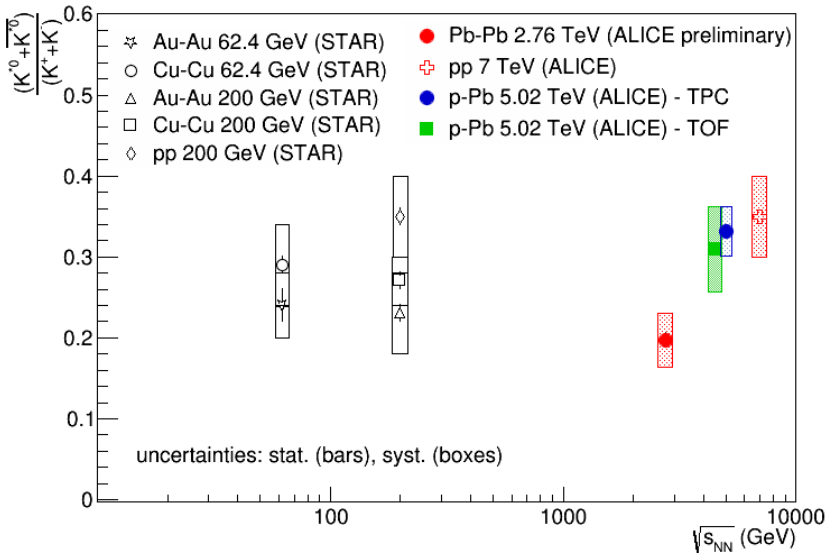

Figure 5.3: K^{*0}/K ratio as a function of the collision energy. The value of the ratio for p-Pb collisions is indicated with the blue marker for the TPC analysis and with the green marker for the TOF analysis (shifted left for visibility). The results from pp, Cu-Cu, Au-Au measured by STAR [111] and pp and Pb-Pb (preliminary) measurements by ALICE are also shown.

Conclusions

Within the research on Quark Gluon Plasma, resonances are used to probe the medium properties in the partonic and hadronic phase. In particular, the study of the system in the time lapse between chemical and kinetic freeze-out is of interest.
This thesis focuses on the production of the K^{*0} resonance in p-Pb collisions at 5.02 TeV measured with the ALICE detector. Two independent, parallel analysis were carried on using the Time Projection Chamber (TPC) and the Time of Flight (TOF) detectors for particle identification.
The resonance was reconstructed through the hadronic decay in charged particles (kaons and pions) and the invariant mass distribution, from which the signal was extracted, was obtained selecting matching unlike-sign pairs among the reconstructed tracks. The background was estimated with the like-sign technique and subtracted from the unlike-sign distribution. At this point, a few differences between the TPC and TOF analyses have been noted. The residual background for the TPC analysis is higher than for the TOF analysis at low p_T and its shape varies more irregularly over all the p_T range. In spite of the different shapes, a second degree polynomial function was found to give the best description of the residual background distribution for both TPC and TOF analyses.
The raw yields extracted from the fit of the invariant mass distribution are of central importance for the analysis shown in this work. From the raw yields after normalization and corrected for efficiency and branching ratio, the K^{*0} p_T spectra is obtained. The systematic uncertainties on the yields from the TPC and TOF analyses have been estimated by varying the selection criteria, comparing different method for background subtraction and changing

the fit settings. The systematic uncertainties are evaluated as a function of the transverse momentum of the K^{*0} and are, on average, 12% (TPC) and 17% (TOF).
The results show that TPC and TOF have different performances but are both valid and efficient tools for particle identification. The best performance could be achieved with a TPC-TOF combined analysis.
The spectra have been fitted with a Lèvy-Tsallis function in order to extract the integrated yields. The integrated yields thus obtained have been used to compute the K^{*0}/K ratio. Hints of the presence of possible rescattering effects in p-Pb collisions have been observed in this ratio as a function of the collisions energy, $\sqrt{s_{NN}}$. The ratio values obtained, both in the TPC and TOF analyses, lay in-between the results from pp and Pb-Pb collisions, also measured by ALICE.

Appendix A

Invariant mass fit

In the following, the fit on the like-sign background-subtracted invariant mass distribution for all the p_T bins will be show for both the TOF and TPC analysis.
The like-sign background-subtracted invariant mass distribution for the TOF has been studied for $p_T \geq 1$ GeV/c in order to avoid the region of lower TOF PID efficiency.

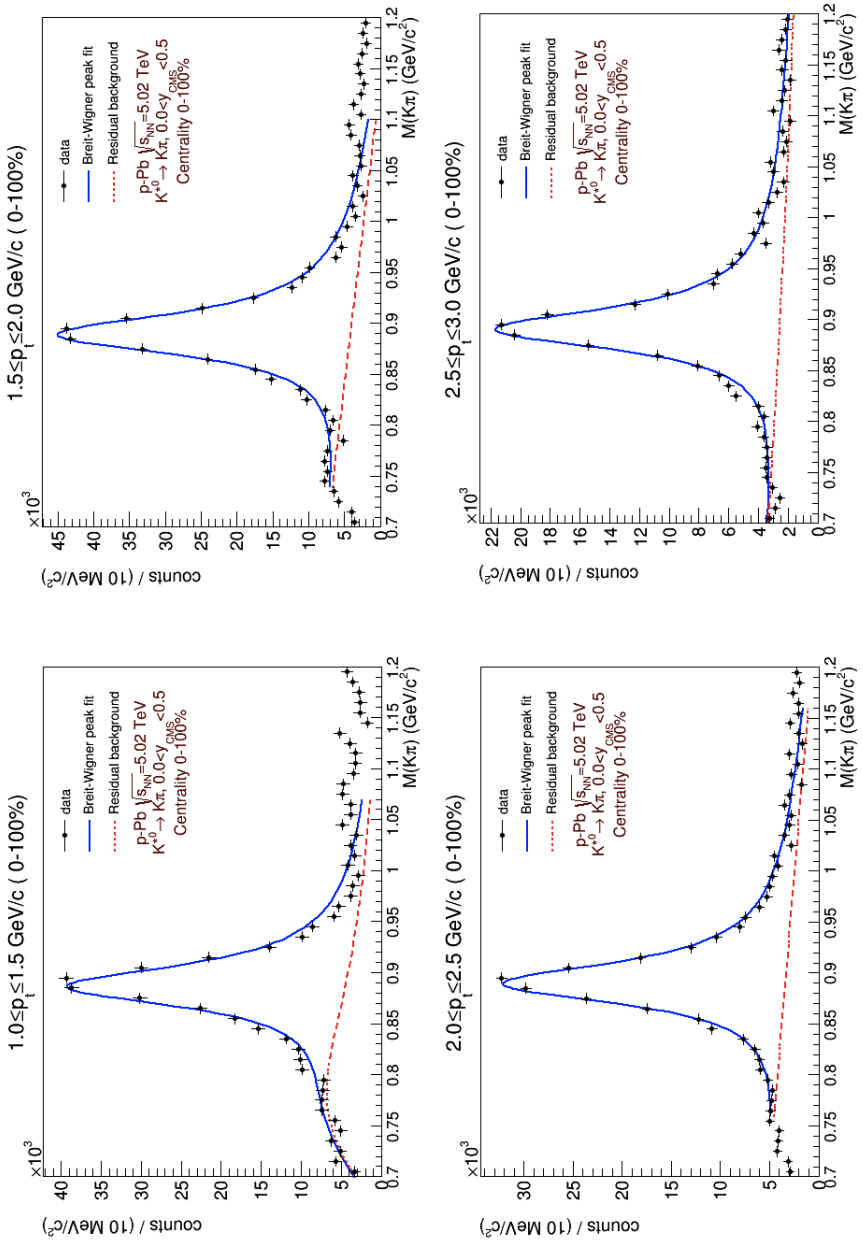

Figure A.1: Fit on the like-sign background-subtracted invariant mass distribution (black points) for the TOF 2σ analysis. The resonance peak is fitted with a relativistic Breit-Wigner for the signal (solid line), while an exponential convoluted with a step function for the first bin, a first degree polynomial for the second and third p_T bin and a second degree polynomial were used (dashed line) to shape the residual background. The Breit-Wigner width is fixed to the PDG value, and the width of each bin is 10 MeV/c^2.

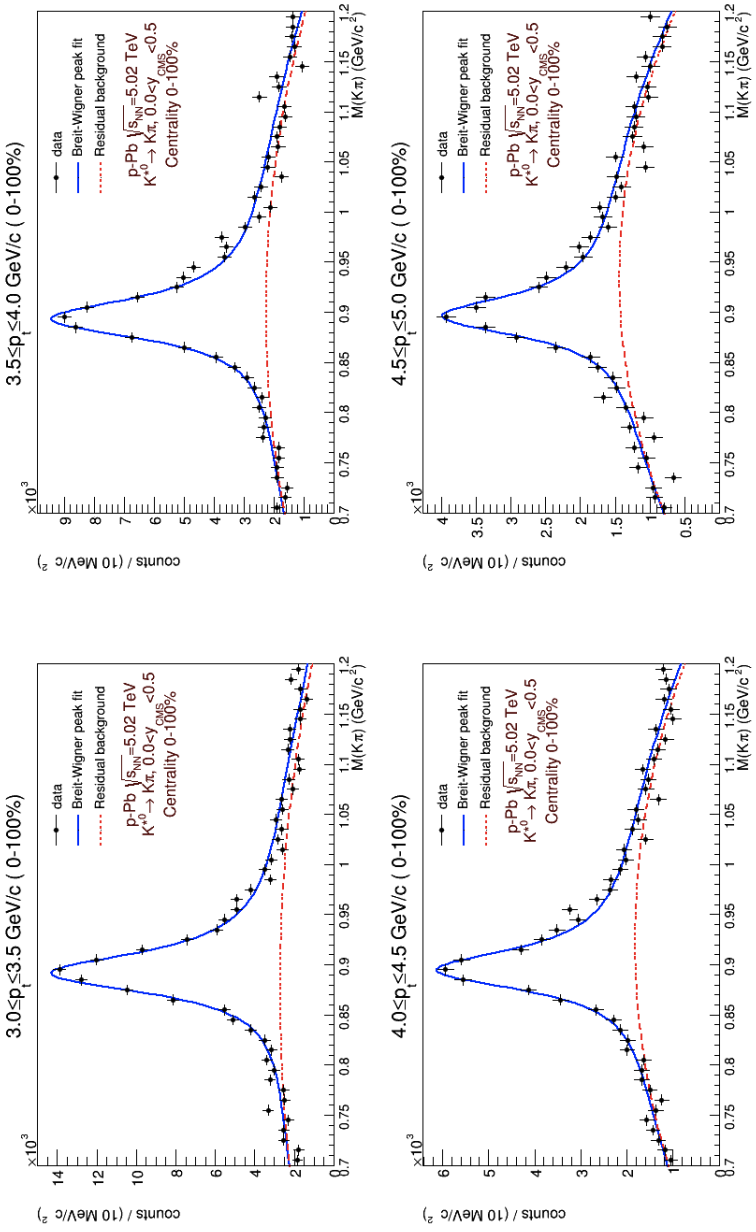

Figure A.2: Fit on the like-sign background-subtracted invariant mass distribution (black points) for the TOF 2σ analysis. The resonance peak is fitted with a relativistic Breit-Wigner for the signal (solid line) and a second degree polynomial (dashed line) to shape the residual background. The Breit-Wigner width is fixed to the PDG value, and the width of each bin is 10 MeV/c^2.

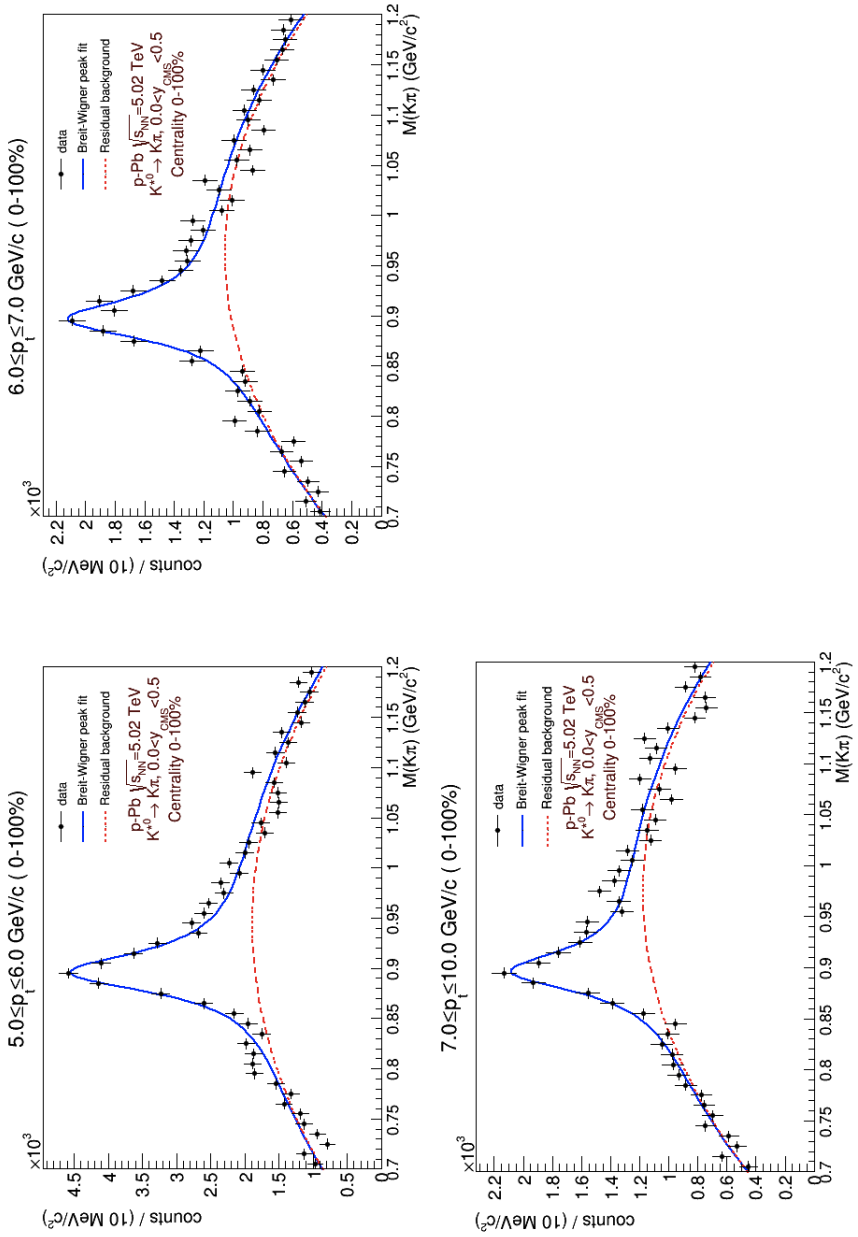

Figure A.3: Fit on the like-sign background-subtracted invariant mass distribution (black points) for the TOF 2σ analysis. The resonance peak is fitted with a relativistic Breit-Wigner for the signal (solid line) and a second degree polynomial (dashed line) to shape the residual background. The Breit-Wigner width is fixed to the PDG value, and the width of each bin is 10 MeV/c^2.

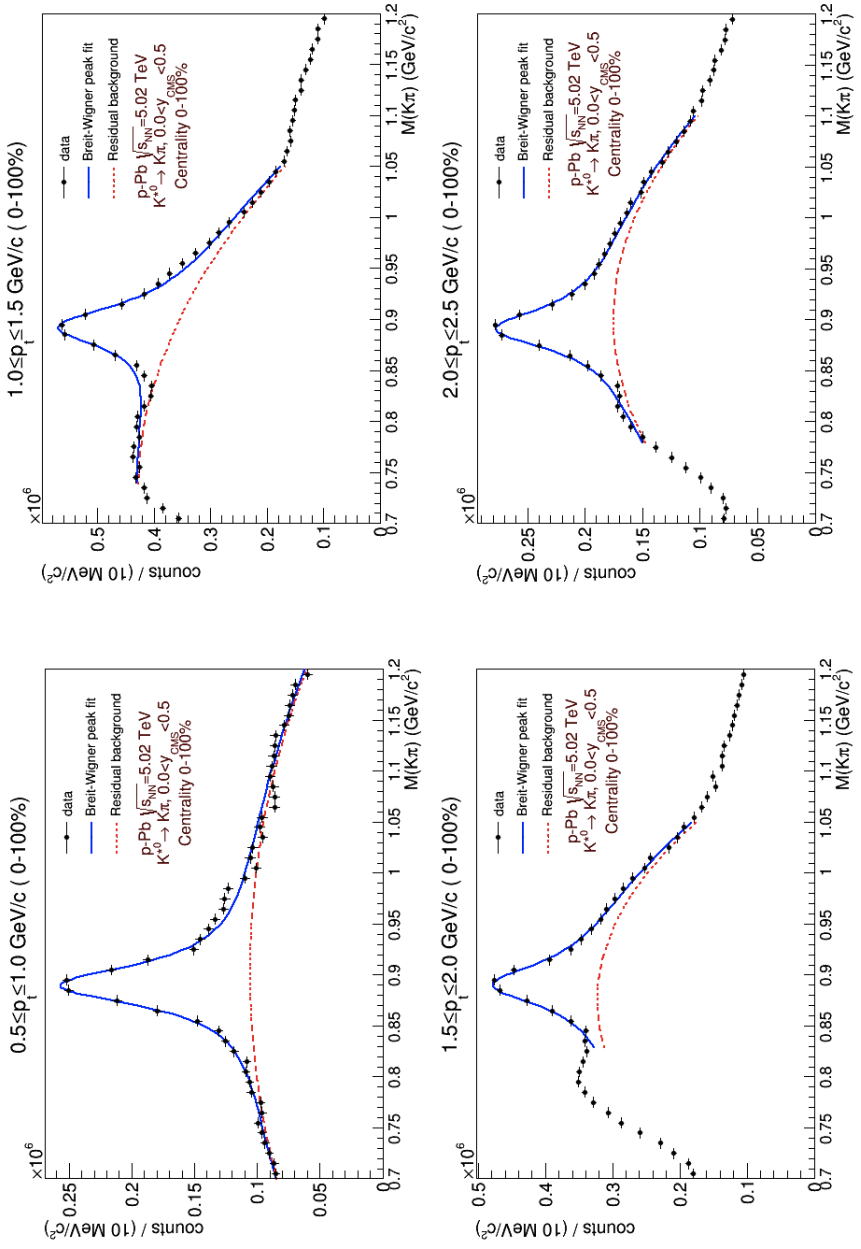

Figure A.4: Fit on the like-sign background-subtracted invariant mass distribution (black points) for the TPC 2σ analysis. The resonance peak is fitted with a relativistic Breit-Wigner for the signal (solid line) and a second degree polynomial (dashed line) to shape the residual background. The Breit-Wigner width is fixed to the PDG value, and the width of each bin is 10 MeV/c^2.

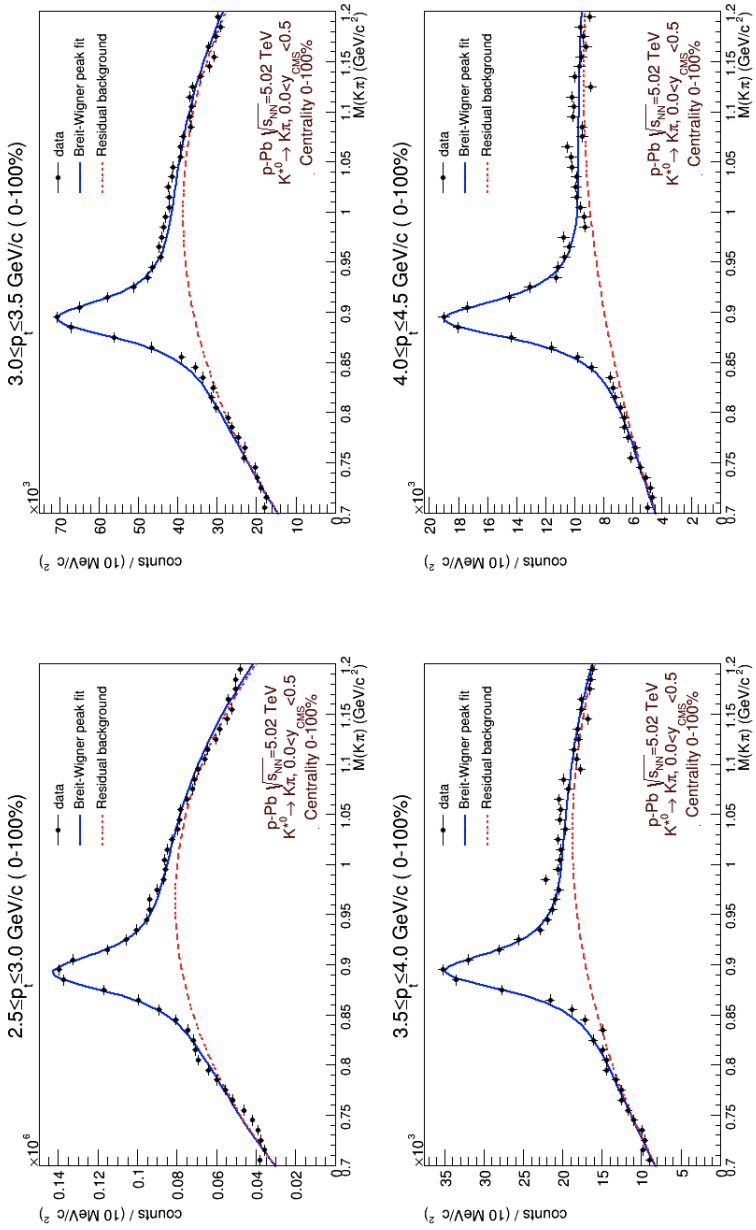

Figure A.5: Fit on the like-sign background-subtracted invariant mass distribution (black points) for the TPC 2σ analysis. The resonance peak is fitted with a relativistic Breit-Wigner for the signal (solid line) and a second degree polynomial (dashed line) to shape the residual background. The Breit-Wigner width is fixed to the PDG value, and the width of each bin is 10 MeV/c^2.

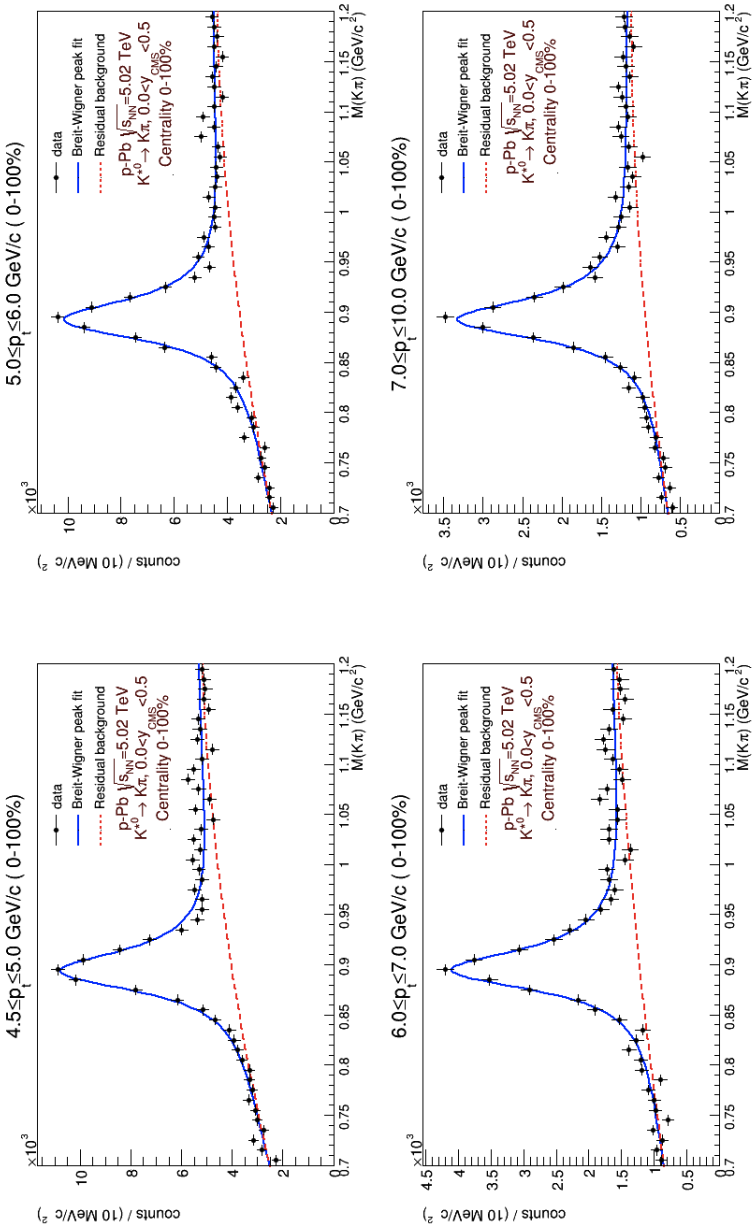

Figure A.6: Fit on the like-sign background-subtracted invariant mass distribution (black points) for the TPC 2σ analysis. The resonance peak is fitted with a relativistic Breit-Wigner for the signal (solid line) and a second degree polynomial (dashed line) to shape the residual background. The Breit-Wigner width is fixed to the PDG value, and the width of each bin is 10 MeV/c^2.

Bibliography

[1] A. Bettini, *Introduction to elementary particle physics*, Cambridge University Press.

[2] P. Skands, *Introduction to QCD* [arXiv:hep-ph/1207.2389].

[3] R. Craig Group, *Measurement of the Inclusive Jet Cross Section Using the Midpoint Algorithm in Run II at CDF* (Dissertation presented to the graduate School of the University of Florida in partial fulfillment of the requirements for the degree of doctor of philosophy).

[4] U. Heinz, *Concepts of heavy-ion physics* [arXiv:hep-ph/0407360v1].

[5] H. Satz, *The Thermodynamics of Quarks and Gluons* [arXiv:hep-ph/0803.1611v1].

[6] K. Safarìk, *Heavy-ion physics* (Prepared for 1999 European School of Conference: C99-08-22, p.267-288).

[7] Meisinger P. N., Miller T. R., Ogilvie M. C., *Phenomenological Models of the Quark-Gluon Plasma Equation of State* [arXiv:hep-lat/0110173].

[8] R. Baier, Yu.L. Dokshitzer, A.H. Mueller, S. Peignè, D. Schiff *Radiative energy loss of high energy quarks and gluons in a finite volume quark-gluon plasma* [arXiv:hep-ph/9607355].

[9] Tounsi A., Redlich K., *Strangeness Enhancement and Canonical Suppression* [arXiv:hep-ph/0111159].

[10] Becattini F., Manninen J., *Strangeness production from SPS to LHC* J. Phys. G: Nucl. Part. Phys. 35, 104013 (2008).

[11] P. Koch, B. Müller and J. Rafelski, Phys. Rep. 142, 167 (1986).

[12] Bass S. *et al.*, Phys. Rev. C **60**, 021902 (1999).

[13] ALICE Collaboration, *Multi-strange baryon production at mid-rapidity in Pb-Pb collisions at* $\sqrt{s_{\rm NN}}$ *= 2.76 TeV* [arXiv:nucl-ex/1307.5543].

[14] Adare A. *et al.* (PHENIX Collaboration), 2010 Phys.Rev.Lett. **104** 132301 (Preprint 0804.4168).

[15] Wilde M. (ALICE Collaboration), 2012 (Preprint 1210.5958).

[16] Lohner D. (ALICE Collaboration), *Measurement of Direct-Photon Elliptic Flow in Pb-Pb Collisions at* $\sqrt{s_{\rm NN}}$ *= 2.76 TeV* [arXiv:hep-ex/1212.3995v2].

[17] Y. Aoki, S. Borsanyi, S. Durr, Z. Fodor, S. Katz *et al.*, JHEP **0906** 088 (2009).

[18] M. Cheng **et al.**, Phys.Rev. **D74** 054507 (2006).

[19] A. Andronic, *The charm of hot matter - charmonium and open charm measurements in Pb-Pb collisions with ALICE at the LHC* [arXiv:nucl-ex/1304.6332v1].

[20] T. Matsui and H. Satz, Phys. Rev. Lett. B **178** (1986) 416.

[21] Z. Conesa del Valle *etal.*, Nucl. Phys. B **214** (2011) 3.

[22] A. Capella, L. Bravina, E.G. Ferreiro, A.B. Kaidalov and E. Zabrodin, Eur. Phys. J. C **58** (2008) 437.

[23] R. Vogt, Phys. Rev. C **81** (2010) 044903; R. Vogt, Phys. Rev. C **61** (2000) 035203.

[24] Arnaldi R. *et al.* (NA60 Collaboration), 2012 Phys. Lett. B **706** 263-267 (Preprint 1004.5523).

[25] Alessandro B. *et al.* (NA50 Collaboration), 2005 Eur. Phys. J. C **39** 335-345 (Preprint hep-ex/0412036).

[26] Adare A. *et al.* (PHENIX Collaboration), 2007 Phys. Rev. Lett. **98** 232301 (Preprint nucl-ex/0611020).

[27] Digal S., Petreczky P. and Satz H. 2001 Phys. Rev. D **64** 094015 (Preprint hep-ph/0106017).

[28] Karsch F., Kharzeev D. and Satz H. 2006 Phys. Lett. B **637** 75-80 (Preprint hep-ph/0512239).

[29] Abelev B. *et al.* (ALICE Collaboration), 2012 Phys. Rev. Lett. **109** 072301 (Preprint 1202.1383).

[30] M.L. Miller, K. Reygers, S.J. Sanders and P. Steinberg, *Glauber Modeling in High Energy Nuclear Collisions* [arXiv:nucl-ex/0701025v1].

[31] d'Enterria D., *Jet quenching* [arXiv:nucl-ex/0902.2011v2].

[32] Adams J. *et al.*, *Evidence from d+Au measurements for final-state suppression of high p_T hadrons in Au+Au collisions at RHIC* [arXiv:nucl-ex/0306024v3].

[33] P. Wang, V. E. Lyubovitskij, Th. Gutsche, and A. Faessler *Chiral symmetry restoration in strange hadronic matter* [arXiv:nucl-th/0311074v2]

[34] D.D. Chinellato (ALICE Collaboration) *Strange and Multi-Strange Particle Production in ALICE* [arXiv:hep-ex/1211.7298v1].

[35] J.Y. Ollitrault, Phys. Rev. D **46**, 229 (1992).

[36] K. Aamodt *et al.* (ALICE Collaboration), Phys. Rev. Lett. **107** 032301 (2011).

[37] (ALICE Collaboration) *Anisotropic flow of charged hadrons, pions and (anti-)protons measured at high transverse momentum in Pb-Pb collisions at $\sqrt{s_{\rm NN}}$ = 2.76 TeV* [arXiv:nucl-ex/1205.5761v2].

[38] G. Kestin and U.W. Heinz, Eur. Phys. J. C **61**, 545 (2009).

[39] H. Niemi, K. J. Eskola, and P.V. Ruuskanen, Phys. Rev. C **79**, 024903 (2009).

[40] Yuri Kharlov (ALICE collaboration), *Recent results from ALICE* [arXiv:nucl-ex/1203.2420v1].

[41] W. A. Horowitz and M. Gyulassy, J. Phys. G **38**, 124114 (2011).

[42] ALICE Collaboration [arXiv:hep-ex/1208.1974].

[43] L. Milano (ALICE Collaboration), Nuclear Physics A, Volumes 904–905, Pages 531c-534c.

[44] A. Andronic, P. Braun-Munzinger and J. Stachel, Phys. Lett. B 678:516 (2009).

[45] A. Andronic *et al.*, Nucl. Phys. A **772** (2006), 167.

[46] J. Cleymans, K. Redlich, Phys. Rev. Lett. **81**, 5284-5286 (1998).

[47] S. Singha, Quark Matter 2012 proceedings.

[48] J. Steinheimer, J. Aichelin and M. Bleicher, [arXiv:nucl-th/1203.5302v1] (2012).

[49] F. Becattini, M. Bleicher, T. Kollegger, M. Mitrovski, T. Schusterand, R. Stock, [arXiv:nucl-th/1203.5302v1] (2012).

[50] STAR Collaboration, Phys. Rev. C79, 034909 (2009).
PHENIX Collaboration, Phys. Rev. C69, 034909 (2004).
BRAHMS Collaboration, Phys. Rev. C72, 014908 (2005).

[51] J. Cleymans *et al.*, Phys. Rev. C **74**, 034903 (2006).

[52] F. Bellini, *Measurement of K(892)^{*0} resonance production in PbÐPb collisions with the ALICE experiment at the LHC* (Doctoral thesis).

[53] C. Markert *et al.*, Proceedings of PASI 2002 [arXiv:hep-ph/0206260].

[54] A. Andronic *et al.*, Phys. Lett. B **673**, (2009) 142-145.

[55] P. Braun-Munzinger and J. Stachel, *Hadron Production in Ultra-relativistic Nuclear Collisions and the QCD Phase Diagram: an Update* from *Nuclei To Stars: Festschrift in Honor of Gerald E Brown*, ed. S. Lee (World Scientific, Singapore, 2011) [arXiv:1101.3167v1].

[56] A. Andronic *et al.*, J. Phys. G: Nucl. Part. Phys. **38** (2011) 124081.

[57] G. Torrieri and J. Rafelski, Phys. Lett. B **509**, (2001) 239-245.

[58] R. Rapp *et al.*, [arXiv:0901.3289v1].

[59] A. G. Knospe *Hadronic Resonances in Heavy-Ion Collisions at ALICE* [arXiv:nucl-ex/1301.1581v1].

[60] B.I. Abelev *et al*, *Hadronic resonance production in d+Au collisions at* $\sqrt{s_{\rm NN}}$ *= 200 GeV at RHIC* [arXiv:nucl-ex/0801.0450]

[61] Aguilar-Benitez M. *et al.* (LEBC-EHS Collaboration), Z. Phys. C **50**, 405 (1991).

[62] Albrecht H. *et al.*, Z. Phys. C **61**, 1 (1994).

[63] J. Beringer *et al.*, *The Review of Particle Physics (Particle Data Group)*, Phys. Rev. D **86**, 010001 (2012).

[64] ALICE Collaboration, *Production of* $K^{*0}(892)^0$ *and* $\phi(1020)$ *in p-p collisions at* $\sqrt{s_{\rm NN}}$ *= 7 TeV* [arXiv:hep-ex/1208.5717v2].

[65] ALICE Collaboration, [arXiv:nucl-ex/1210.3615v2].

[66] A. Dumitru, D. E. Kharzeev, E. M. Levin and Y. Nara, Phys.Rev. C **85** (2012) 044920, [arXiv:hep-ph/1111.3031].

[67] G. Barnafoldi, J. Barrette, M. Gyulassy, P. Levai and V. Topor Pop, Phys.Rev. C**85** (2012) 024903, [arXiv:nucl-th/1111.3646].

[68] P. Tribedy and R. Venugopalan, Phys.Lett. B **710** (2012) 125Ð133, [arXiv:hep-ph/1112.2445].

[69] R. Xu, W.-T. Deng, and X.-N. Wang, [arXiv:nucl-th/1204.1998].

[70] J. L. Albacete, A. Dumitru, H. Fujii and Y. Nara, [arXiv:hep-ph/1209.2001].

[71] S. Roesler, R. Engel, and J. Ranft, [arXiv:hep-ph/0012252].

[72] B. Back *et al.* (PHOBOS Collaboration), Phys.Rev.Lett. **93** (2004) 082301, [arXiv:nucl-ex/0311009].

[73] B. Alver *et al.* (PHOBOS Collaboration), Phys.Rev. C **83** (2011) 024913, [arXiv:nucl-ex/1011.1940].

[74] ALICE Collaboration, [arXiv:nucl-ex/1210.4520v1].

[75] (PHENIX Collaboration) K. Adcox *et al.*, Phys. Rev. Lett. **88** 022301 (2002), [arXiv:nucl-ex/0109003].

[76] (STAR Collaboration), C. Adler *et al.*, Phys. Rev. Lett. **89**, 202301 (2002), [arXiv:nucl-ex/0206011].

[77] (ALICE Collaboration) K. Aamodt *et al.*, Phys. Lett. B **696**, 30 (2011), [arXiv:1012.1004]

[78] (CMS Collaboration) S. Chatrchyan *et al.*, Eur. Phys. J. C **72**, 1945 (2012), [arXiv:1202.2554].

[79] (ALICE Collaboration) B. Abelev *et al.*, [arXiv:1208.2711].

[80] Lyndon Evans, JINST 3 S08001 (2008).

[81] ALICE Collaboration, JINST 3 S08002 (2008).

[82] ATLAS Collaboration, JINST 3 S08003 (2008).

[83] CMS Collaboration, JINST 3 S08004 (2008).

[84] LHCb Collaboration, JINST 3 S08005 (2008).

[85] B. Abelev (ALICE Collaboration), Phys. Rev. Lett. **105** (2010) 252301 [arXiv:1011.3916].

[86] J. Wiechula (ALICE TPC Collaboration), Nuclear Physics A 830 (2009) 531c-534c.

[87] A. Akindinov *et al.*, Eur. Phys. J. Plus (2013) **128** 44.

[88] K. Aamodt *et al.* (ALICE Collaboration), Phys. Rev. Lett. **106**, 032301 (2011).

[89] P. Saiz *et. al* (ALICE Collaboration), Nucl. Instr. and Meth. A **502** (2-3), 437-440 (2003).

[90] http://aliweb.cern.ch/Offline/.

[91] R. Brun and F. Rademakers, Nucl. Instr. Meth. A **389** (12), 81-86 (1997).

[92] X. N. Wang and M. Gyulassy, Phys.Rev. D **44**, 3501-3516 (1991).

[93] T. Sjostrand, S. Mrenna and P. Skands, J. High Energy Phys. **05**, 026 (2006).

[94] S. Roesler, R. Engel, J. Ranft, [arXiv:hep-ph/0012252].

[95] http://wwwasd.web.cern.ch/wwwasd/geant/index.html.

[96] http://wwwasd.web.cern.ch/wwwasd/geant/index.html (1993).

[97] S. Agostinelli *et al.*, Nucl. Instr. and Meth A **506** (3), 250-303 (2003).

[98] A.Fassetal, http://www.slac.stanford.edu/econf/C0303241/proc/papers/OMT004.PDF.

[99] P. Billoir, Comp. Phys. Comm. **57** (1-3), 390-394 (1989).

[100] Greg Welch and Gary Bishop, *An Introduction to the Kalman Filter* TR 95-041, Department of Computer Science University of North Carolina at Chapel Hill.

[101] B. Batyunya and K. Safarik, ALICE-INT-97-24 (1997).

[102] E. Bruna, A.Dainese, M. Masera and F. Prino, ALICE-INT-2009-018 (2009).

[103] D. Caffarri, Ph.D. thesis, Scuola di Dottorato di Ricerca in Fisica dell'Università di Padova, (2011).

[104] J. Alme *et al.*, Nuclear Instruments and Methods in Physics Research A 622 (2010) 316-367.

[105] http://roofit.sourceforge.net.

[106] J. Adams *et al.*, *K^{*0}(892) resonance production in Au+Au and p+p Collisions at $\sqrt{s_{\rm NN}}$ = 200 GeV at RHIC* [arXiv:nucl-ex/0412019v2].

[107] R. Barlow, [arXiv:hep-ex/0207026].

[108] (ALICE Collaboration) [arXiv:nucl-ex/1307.6796].

[109] (STAR Collaboration), Phys. Rev. C75 064901 (2007).

[110] (ALICE Collaboration) Eur. Phys. J. C (2012) 72:2183.

[111] Phys. Rev. C 71, 064902 (2005)
Phys. Rev. C 84, 034909 (2011).